國立台灣大學 電機工程學研究所

博士論文

指導教授：李百祺教授

使用線性陣列之超音波乳房斷層掃描技術

Ultrasonic Computed Tomography of the Breast Using Linear Arrays

研究生：黃聖文　撰

中華民國九十三年七月

中文摘要

使用傳統超音波灰階影像來偵測乳房中的腫瘤時，其效果常因對比解析度不足而受限。使用其他的組織特性如聲速和衰減係數來成像，可以提供額外的診療資訊。在本論文中，我們提出了一個基於有限角度穿透式斷層掃描(limited-angle transmission tomography)來重建乳房中聲速分佈和衰減係數(attenuation coefficient)分佈的技術。我們所用的成像設備和乳腺 X 光攝影檢查術(x-ray mammography)的設備類似。在這個設備中，一個所有通道都可獨立發射、接收的線性陣列探頭被置於乳房的上方，而一個置於乳房下方的金屬板則被用來反射脈衝信號以取得成像所需的飛行時間(time-of-flight)資料和衰減資料。使用這個設備可以同時取得成傳統超音波灰階影像、聲速分佈和衰減係數分佈所需的資料。然而有限的投影角度使得系統無法收集到重建聲速分佈和衰減係數分佈所需的完整資料，也使得重建出來的結果不準確。為了改善準確度，我們發展出一個基於凸面規劃(convex programming formulation)的重建演算法。在聲速分佈的重建方面，這個演算法成功地利用同一成像物體的傳統灰階影像資訊來提升聲速估計的準確度。而在衰減係數分佈的重建方面，為了改善衰減係數的估計準確度，除了使用基於凸面規劃的重建演算法，我們還提出了一個基於角頻法(angular spectrum method)的技術，利用聲速分佈的資訊來補償折射對衰減資料的不利影響。模擬和實驗結果證實了使用我們所提出的方式，利用線性陣列探頭來進行有限角度穿透式斷層掃描是可行的。聲速分佈和衰減係數分佈可以用來輔助傳統超音波灰階影像，提升偵測乳房中腫瘤的準確度。

Abstract

The performance of B-mode ultrasound in the clinical detection of breast cancer is often limited by poor contrast resolution. Contrast mechanisms based on alternative tissue characteristics, such as direct estimation of sound velocities and attenuation coefficients in different tissues, may offer additional diagnostic information. An approach based on limited-angle transmission tomography for reconstruction of the sound velocity distribution and attenuation coefficient distribution in the breast is proposed in this thesis. The imaging setup is similar to that of x-ray mammography. With this setup, the time-of-flight data and the attenuation data are acquired by a linear array positioned at the top of the compressed breast that both transmits and receives, and a metal plate is placed at the bottom as a reflector. Such a setup can be easily integrated with a B-mode system so that the acoustic data for all of the B-mode image, the sound velocity distribution, and the attenuation coefficient distribution can be simultaneously acquired. However, the acquired data are incomplete, and this results in inaccurate sound velocity estimation and attenuation coefficient estimation. In order to improve the estimation accuracy, a new reconstruction algorithm based on a convex programming formulation was developed. This improvement is mainly attributable to the proposed algorithm successfully incorporating information from the B-mode image of the same object. Furthermore, a technique based on the angular spectrum method was developed to compensate the effects of refraction on the attenuation data using the information on sound velocity distribution. Simulation results and experimental results demonstrate that the proposed approach to limited-angle transmission tomography using linear arrays is feasible. Both the sound velocity image and the attenuation coefficient image can be used to complement conventional B-mode image to enhance the detection of breast cancer.

List of Symbols

$a_{ij}(t)$	echo from metal plate
c	sound velocity
d_{p}	propagation distance
$d(u,C)$	distance between u and C
$e_{ij}(t)$	channel data
f	temporal frequency
$g(t)$	pulse signal
k	spatial frequency
p_{A}	pitch of the array
s	slowness
t	time
t_{ij}	time of flight
w	wave
A	amplitude
C	set
D_{A}	distance between array and metal plate
I	index set
N_{A}	total number of channels in linear array
P_C	projector onto C
W	wave
$\widetilde{W}$	angular spectrum
α	attenuation coefficient
$\boldsymbol{\alpha}$	attenuation coefficient distribution
β	absorption
θ	angle
ρ	density
$\Delta\mathbf{a}$	attenuation data
$\Delta\mathbf{s}$	slowness distribution
Δt_{ij}	geometrically compensated time of flight
Φ	cost function

Table of Contents

List of Figures

List of Tables

Chapter 1 Introduction

1.1 Sound velocity, attenuation coefficient, and breast cancer detection

The detection of breast cancer using B-mode ultrasound is of clinical importance [1]–[4]. Although x-ray mammography is also a popular modality for breast cancer detection, ultrasound is more effective in cases such as the differential diagnosis of pathologies in the radiologically dense breast [1]. Furthermore, B-mode ultrasound is an effective adjunct to mammography in reducing the number of negative biopsy results [4]. In order to improve the effectiveness of B-mode ultrasound in breast cancer detection, several issues need to be addressed. First, severe distortions caused by sound velocity inhomogeneities (including phase aberrations and wavefront amplitude distortions [5]–[9]) may be present. Such distortions degrade the contrast resolution and therefore reduce cancer detectability. Furthermore, even if a region of interest (ROI) is detectable above the background it may still be difficult to distinguish a tumor from a region of fat. This leads to a second issue, related to the fundamental contrast mechanism. In B-mode ultrasound, the image contrast is primarily determined by tissue scattering properties and acoustic impedance. In other words, if two regions in the image have similar scattering properties and acoustic impedance, they may not be distinguishable. In breast B-mode ultrasound, a fat region and a tumor may have similar characteristics on the resulting image. For example, the B-mode image of a solid homogeneous hypoechoic tumor with irregular borders may look like a fat region [1]. Alternative imaging methods can be used to form a breast image based on different acoustic parameters. One example is the elasticity imaging based on elastic modulus [10], [11]; since elastic modulus varies over a wide range in different tissues, it is possible to provide a much higher contrast among different tissues of interest.

In this study, two physical parameters are of interest. The first one is the sound velocity. One of the reasons is that the velocity of sound in cancerous tissue is higher than that in fat [12]. Although the sound velocity distribution alone may not be adequate for obtaining full diagnostic information, tumors can be detected more accurately and effectively by combining the sound velocity distribution information

with the corresponding B-mode image. The second reason for using sound velocity is that if the sound velocity distribution can be found, it may be possible to devise an adaptive imaging scheme and to correct for the image distortion in conventional B-mode imaging due to sound velocity inhomogeneities [13]–[18]. Another physical parameter of interest is the attenuation coefficient because the attenuation coefficient varies from tissue to tissue. For example, the attenuation of cancerous tissue is higher than that of cyst. Therefore, the attenuation coefficient distribution in the breast can also help the detection of breast cancer [19]–[21].

1.2 Limited angle transmission tomography

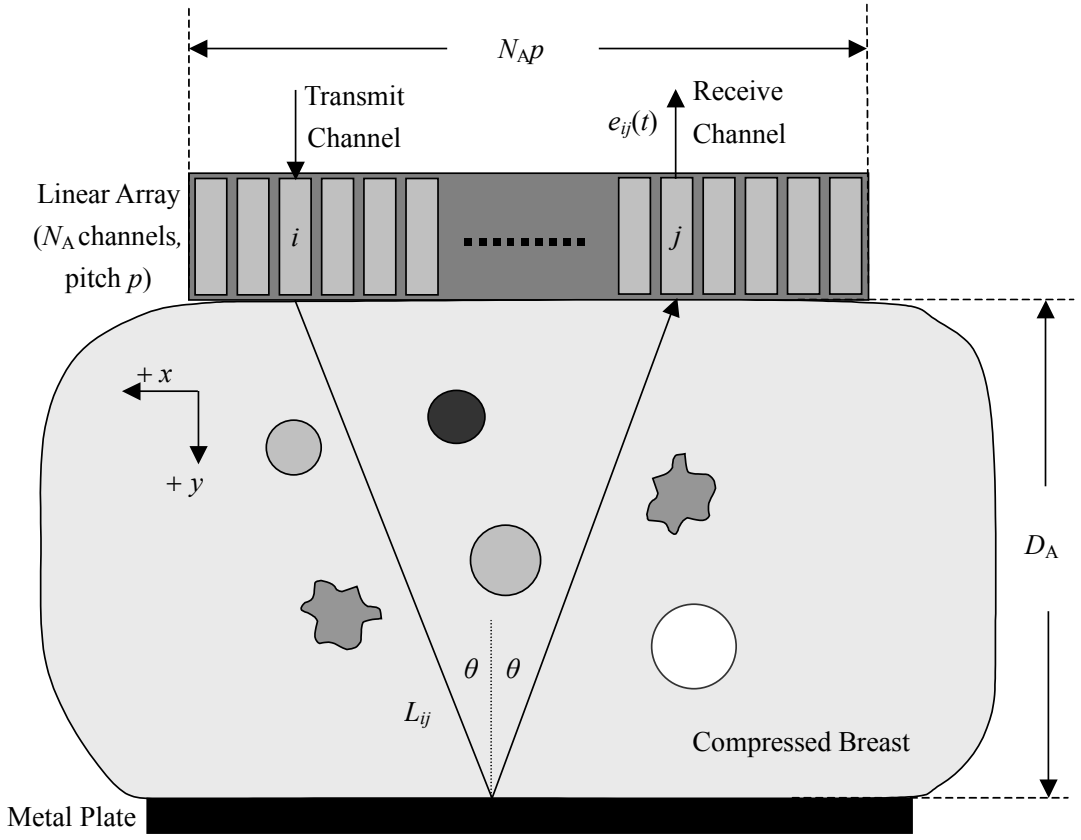

Fig. 1.1. Tomographic imaging setup allowing the acquisition of B-mode images, sound velocity distributions, and attenuation coefficient distributions. Each of the channels in the array can transmit independently. A metal plate at the bottom of the compressed breast reflects the acoustic signal.

The sound velocity distribution and the attenuation coefficient distribution can be measured using ultrasonic computed tomography [22]. However, the apparatus used for computed tomography is very different from that used for B-mode imaging. It is the main purpose of this thesis to develop an imaging strategy for reconstructing the

sound velocity distribution and the attenuation coefficient distribution using pulse-echo data from a linear array, such as that used in B-mode imaging. Hence, the limited-angle transmission tomography setup shown in Fig. 1.1 was adopted [23], [24]. Fig. 1.1 shows that a linear array is placed at the top of the image object and a metal plate at the bottom reflects the acoustic wave. In addition to performing B-mode imaging, the imaging setup is also capable of transmitting a wideband pulse from a single channel in order to acquire a complete channel data set and corresponding time-of-flight data set and attenuation data set, which contain information on the sound velocity distribution and the attenuation coefficient distribution of the image object, respectively. Thus, all of the B-mode images, sound velocity distributions, and attenuation coefficient distributions can be acquired using a single setup. Note that the setup is similar to the setup proposed by Krueger *et al.* [25], [26]. Nonetheless, a new reconstruction algorithm is proposed in this thesis that provides a significant improvement in estimation accuracy. As described in Section 2.3, the B-mode image is used for segmentation such that constraints can be properly defined and imposed during reconstruction, and the improvement in estimation accuracy is mainly attributable to the proposed technique successfully incorporating information from the B-mode image of the same object. Note that the use of B-mode images for segmentation has also been proposed in near-infrared breast imaging [27], [28].

1.3 Thesis organization

This thesis is organized as follows. Chapter 2 presents the basic equations for the imaging setup shown in Fig. 1.1 and introduces the algorithms for reconstructing sound velocity distributions. In Chapter 3, simulations were performed to test the efficacy of the proposed technique. The effects of wave propagation such as refraction and diffraction were included in the simulated data, and these data were used to evaluate the algorithms introduced in Chapter 2. In Chapter 4, a custom-made phantom containing a variety of image objects with differing physical properties was used to experimentally investigate the performance of the approach proposed in Chapter 2 and evaluated by simulations in Chapter 3 for reconstructing sound velocity distributions. The imaging setup shown in Fig. 1.1 can also be used to reconstruct attenuation coefficient distributions. Chapter 5 presents the basic equations and the algorithms for reconstructing attenuation coefficient distributions, which were experimentally evaluated using the data used in Chapter 4. Chapter 6 discusses the efficacy of applying the sound velocity distribution to correcting for the waveform

distortions caused by sound velocity inhomogeneities and the efficacy of applying coded excitation to signal-to-noise ratio (SNR) enhancement when collecting the time-of-flight data. This thesis concludes in Chapter 7. Future works are also described. Appendix A presents a new coded excitation scheme that efficiently synthesizes codes for arbitrary waveforms using a bipolar square wave pulser. The technique can be applied to enhance the SNR, which is essential for time-of-flight estimation.

Chapter 2 Reconstruction of the sound velocity distribution

2.1 Basic equations for the imaging setup

Consider the imaging setup shown in Fig. 1.1. Assume that the image objects contain targets uniform along the z-axis, and t denotes the time. Note that the setup is similar to that of x-ray mammography [29] and the one proposed by Krueger *et al.* for ultrasound [25], [26]. Fig. 1.1 shows that the linear array has N_{A} channels and that a metal plate is used for reflecting the acoustic wave. The array axis and the beam axis are defined as the x-axis and the y-axis, respectively. In addition to performing B-mode imaging, the imaging setup shown in Fig. 1.1 is also capable of transmitting a wideband pulse from a single channel in order to acquire a complete channel data set $\{e_{ij}(t)\}, 1 \le i, j \le N_{\mathrm{A}}$, where $e_{ij}(t)$ is the echo signal received by channel j when only channel i transmits. With $e_{ij}(t)$, the time-of-flight t_{ij} corresponding to the same transmit/receive combination for the echo reflected from the bottom metal plate can be obtained.

Let $c(x, y)$ denote the sound velocity at the center frequency of the transmitted pulse. When only soft tissues are considered and only time-of-flight is of interest, effects of refraction associated with sound velocity inhomogeneities can be ignored [22]. In this case,

$$t_{ij} = \int_{L_{ij}} s(x, y)\, dl \,, \tag{2.1}$$

where L_{ij} is the path of the line integral as shown in Fig. 1.1, and $s(x, y) = c^{-1}(x, y)$ is defined as the slowness. Assume the average slowness in the image object is $s_0 = c_0^{-1}$, and define

$$t_{ij,0} = \int_{L_{ij}} s_0 dl \tag{2.2}$$

as the geometrical delay, then the time-of-flight with geometrical delay compensated becomes

$$\Delta t_{ij} = t_{ij} - t_{ij,0} = \int_{L_{ij}} [s(x,y) - s_0] dl = \int_{L_{ij}} \Delta s(x,y) dl \,. \tag{2.3}$$

$\Delta s(x,y)$ can be discretized with spatial sampling intervals Δx_{s} and Δy_{s} in the x and y directions, respectively. In this case, (2.3) becomes

$$\Delta t_{ij} = \sum_{n=1}^{N} \sum_{m=1}^{M} \Delta s(m,n) l_{ij}(m,n) = \mathbf{l}_{ij}^{\mathrm{T}} \Delta \mathbf{s} \,, \tag{2.4}$$

where $\mathbf{l}_{ij}$ and $\Delta\mathbf{s}$ are $MN \times 1$ column vectors, $\left(\mathbf{l}_{ij}\right)_{(m-1)N+n} \equiv l_{ij}(m,n)$ is the contribution of grid point (m,n), $1 \le m \le M$, $1 \le n \le N$ [i.e., the length of the line segment which is the intersection of the path L_{ij} and the rectangle centered at the grid point (m,n) with a size of $\Delta x_{\mathrm{s}} \times \Delta y_{\mathrm{s}}$], and $\left(\Delta\mathbf{s}\right)_{(m-1)N+n} \equiv \Delta s(m,n)$.

There are a total of N_{A}^2 equations in (2.4). Due to the assumption of the straight-line propagation path, $\mathbf{l}_{ij} = \mathbf{l}_{ji}$, and Δt_{ij} can be set to $\left(\Delta t_{ij} + \Delta t_{ji}\right)/2$ for $1 \le i \le N_{\mathrm{A}}$, $1 \le j \le i$. Thus, the number of equations reduces to $N_{\mathrm{A}}(N_{\mathrm{A}}+1)/2$ and they can be put into the following matrix form:

$$\mathbf{L}\Delta\mathbf{s} = \Delta\mathbf{t} \,, \tag{2.5}$$

where $\Delta\mathbf{t}$ is an $\left[N_{\mathrm{A}}(N_{\mathrm{A}}+1)/2\right] \times 1$ column vector and $\mathbf{L}$ is an $\left[N_{\mathrm{A}}(N_{\mathrm{A}}+1)/2\right] \times MN$ matrix. In (2.5), $\Delta\mathbf{t}$ is obtained from the channel data, and $\mathbf{L}$ is calculated based on the geometry. The focus of this thesis is to develop a scheme for accurately solving slowness distribution $\Delta\mathbf{s}$.

2.2 A brief introduction to the convex programming formulation

In this thesis, $C = \{\mathbf{x} \in \mathbf{X} : \text{property } P(\mathbf{x})\}$ means that C is a subset of $\mathbf{X}$ containing all $\mathbf{x}$ in $\mathbf{X}$ which have the property P [30]. A complete inner product space is called a Hilbert space. On the finite-dimensional Euclidean space $\mathbf{R}^{MN}$, if for all $\mathbf{x} = [x_1 \quad x_2 \quad \cdots \quad x_{MN}]^{\mathrm{T}}$ in $\mathbf{R}^{MN}$ and all $\mathbf{y} = [y_1 \quad y_2 \quad \cdots \quad y_{MN}]^{\mathrm{T}}$ in $\mathbf{R}^{MN}$, their inner product is defined as the Euclidean inner product

$$\langle \mathbf{x}, \mathbf{y} \rangle = \sum_{l=1}^{MN} x_l y_l = \mathbf{y}^{\mathrm{T}} \mathbf{x}, \tag{2.6}$$

then $\mathbf{R}^{MN}$ is a Hilbert space [31]. Each slowness distribution $\Delta\mathbf{s}$ is an element in $\mathbf{R}^{MN}$.

Let C be a closed convex set in a Hilbert space $\mathbf{H}$. Then for each u in $\mathbf{H}$, there exists a unique u^* in C that is closest to u. That is,

$$\left\| u - u^* \right\| = \min_{v \in C} \| u - v \|, \tag{2.7}$$

where $\|\cdot\|$ is the norm induced by the inner product. This unique nearest neighbor u^* in C of u is called the projection of u onto C, and the operator assigning $u^* = P_C u$ to each u is called the projector onto C and is denoted by P_C. For example, if the closed convex set C represents a set of distributions satisfying a given condition and u is any initial guess, then a distribution in C that is closest to distribution u can be found. Assume that for a real problem one tries to find a solution u in $\mathbf{H}$ satisfying a given constraint, and the associated constraint set

$$C = \{u \in \mathbf{H} : u \text{ satisfies the given constraint}\} \tag{2.8}$$

is nonempty, closed, and convex, then a solution $u \in C$ is $u^* = P_C u_0$, where u_0 is any given initial condition. If there are k constraints in a problem and each

$$C_i = \{u \in \mathbf{H} : u \text{ satisfies the } i\text{th constraint}\}, i = 1,2,\cdots,l, \tag{2.9}$$

is closed and convex, then all the solutions form a set $C_0 = \bigcap_{i=1}^{l} C_i$ which is also closed and convex. Thus, $P_{C_0} u_0$ is a solution provided that C_0 is nonempty.

In the presence of inconsistent constraints, which may arise from inaccurate measurements such as estimation errors in the pulse arrival time, C_0 is empty and there is no solution. One way to solve this problem is to divide all of the constraints into two classes: one class contains the hard constraints that the solution must satisfy, and the other class contains the soft constraints for which the total amount of violation must be minimized. Let $I^{\mathrm{c}} = I^{\mathrm{h}} \bigcup I^{\mathrm{s}}$ be the finite constraint index set, where I^{h} denotes the possibly empty hard-constraint index set, I^{s} denotes the nonempty soft-constraint index set, and $I^{\mathrm{h}} \bigcap I^{\mathrm{s}}$ is empty. Define

$$\Phi^{\mathrm{s}}(u) = \frac{1}{2}\sum_{i \in I^{\mathrm{s}}} w_i d^2(u, C_i), \tag{2.10}$$

where $w_i \in (0,1]$ for all $i \in I^{\mathrm{s}}$, $\sum_{i \in I^{\mathrm{s}}} w_i = 1$, and $d(u, C_i) = \inf\{\|u - v\| : v \in C_i\}$ is the distance between u and C_i, where inf stands for the greatest lower bound. Suppose that **H** is finite dimensional, C_i is bounded for some $i \in I^{\mathrm{c}}$, $C^{\mathrm{h}} = \bigcap_{i \in I^{\mathrm{h}}} C_i$ is nonempty, and take $u_0 \in C^{\mathrm{h}}$, $\lambda_n \in [0,1]$ for all $n \geq 0$ such that $\sum_{n \geq 0} \lambda_n (1 - \lambda_n) = \infty$, and $\gamma \in (0,2]$. Let

$$u_{n+1} = (1 - \lambda_n) u_n + \lambda_n P_{C^{\mathrm{h}}}\left[(1 - \gamma) u_n + \gamma \sum_{i \in I^{\mathrm{s}}} w_i P_{C_i}(u_n)\right], n \geq 0. \tag{2.11}$$

Then the sequence $\{u_n\}$ converges to a point u with $\Phi^{\mathrm{s}}(u) = \min_{v \in C^{\mathrm{h}}} \Phi^{\mathrm{s}}(v)$ [32]. That is, (2.11) can be used to find a solution that satisfies all the hard constraints and minimizes the objective function Φ^{s}, which is the total amount of violation of the soft constraints. Note that such a problem is in a convex programming formulation since Φ^{s} is a convex function on a convex set C^{h}.

2.3 Reconstruction algorithms

Several approaches can be used to solve (2.5), of which the convex programming formulation for inconsistent problems introduced in Section 2.2 was chosen because it can incorporate the B-mode image information.

To achieve good reconstruction accuracy, prior knowledge of $\Delta\mathbf{s}$ must be used. For example, the sound velocity in soft tissue and $\Delta\mathbf{s}$ are both bounded. Thus, the sound velocity is assumed to be in $[c_{\text{lower}}, c_{\text{upper}}]$ (where $c_{\text{lower}} = 1450$ m/s and $c_{\text{upper}} = 1580$ m/s throughout the thesis), and this is a hard constraint (i.e., a constraint that cannot be violated). Define

$$C_{\text{velocity}} = \left\{\mathbf{x} \in \mathbf{R}^{MN} : x_l \in [c_{\text{upper}}^{-1} - s_0, c_{\text{lower}}^{-1} - s_0], 1 \le l \le MN\right\}, \tag{2.12}$$

where s_0 is the assumed background slowness; then C_{velocity} is referred as a property set since it is relevant to the prior knowledge. Note that C_{velocity}, which contains the slowness distribution that satisfies the velocity constraints, is nonempty, bounded, closed, and convex.

If $\mathbf{L}$ in (2.5) is expressed as $\mathbf{L} = \begin{bmatrix}\mathbf{l}_1 & \mathbf{l}_2 & \cdots & \mathbf{l}_{N_{\text{A}}(N_{\text{A}}+1)/2}\end{bmatrix}^{\text{T}}$ and $\Delta\mathbf{t}$ as $\Delta\mathbf{t} = \begin{bmatrix}\Delta t_1 & \Delta t_2 & \cdots & \Delta t_{N_{\text{A}}(N_{\text{A}}+1)/2}\end{bmatrix}^{\text{T}}$, in order to satisfy (2.5), the slowness distribution $\Delta\mathbf{s}$ must belong to

$$C_{\Delta t_i} = \left\{\mathbf{x} \in \mathbf{R}^{MN} : \langle \mathbf{x}, \mathbf{l}_i \rangle = \Delta t_i\right\}, i = 1, 2, \cdots, N_{\text{A}}(N_{\text{A}}+1)/2, \tag{2.13}$$

where each $C_{\Delta t_i}$ is a closed and convex set in $\mathbf{R}^{MN}$ (i.e., $\Delta\mathbf{s}$ must belong to $\bigcap C_{\Delta t_i}$, the intersection of the $C_{\Delta t_i}$ sets). Each $C_{\Delta t_i}$ set in (2.13) is referred as a data set since it is directly related to the known Δt_i. $\bigcap C_{\Delta t_i}$ may be empty, and even if it is nonempty, the points in the set may not lead to reasonable sound velocities. Therefore, the $C_{\Delta t_i}$ that contains all the slowness distributions that satisfy Δt_i is a soft-constraint set. The slowness distribution $\Delta\mathbf{s}$ does not have to match all time-of-flight data. In other words, violation is allowed. Nonetheless, the distribution must minimize the total errors.

A slowness distribution $\mathbf{x} \in C_{\text{velocity}}$ minimizing the cost function (i.e., the total amount of violation of the time-of-flight data)

$$\Phi_{\text{TOF}}^{\text{S}}(\mathbf{x}) = \frac{1}{2} \sum_{i=1}^{N_{\text{A}}(N_{\text{A}}+1)/2} w_i d^2(\mathbf{x}, C_{\Delta t_i}), \tag{2.14}$$

where $w_i \in (0,1]$ for all $i \in \{1,2,\cdots, N_{\text{A}}(N_{\text{A}}+1)/2\}$, $\sum_{i=1}^{N_{\text{A}}(N_{\text{A}}+1)/2} w_i = 1$, and $d(\mathbf{x}, C_{\Delta t_i})$ is the distance between $\mathbf{x}$ and $C_{\Delta t_i}$, can be found by taking $\mathbf{x}$ as the limit of the sequence $\{\mathbf{x}_n\}$ (i.e., $\lim_{n\to\infty} \mathbf{x}_n$). $\mathbf{x}_0 \in C_{\text{velocity}}$ is an initial slowness distribution, and

$$\mathbf{x}_{n+1} = (1-\lambda_n)\mathbf{x}_n + \lambda_n P_{C_{\text{velocity}}}\left[(1-\gamma)\mathbf{x}_n + \gamma \sum_{i=1}^{N_{\text{A}}(N_{\text{A}}+1)/2} w_i P_{C_{\Delta t_i}}(\mathbf{x}_n)\right], n \geq 0, \tag{2.15}$$

where $\lambda_n \in [0,1]$ for all $n \geq 0$, $\sum_{n\geq 0} \lambda_n(1-\lambda_n) = \infty$, $\gamma \in (0,2]$, and $P_{C_{\text{velocity}}}$ is the projector onto C_{velocity}. This algorithm is called Algorithm I. The parameters λ_n and γ determine the rate of convergence, and the weights w_i reflect the relative importance of the time-of-flight data. In each case in this thesis, all weights w_i were set to be the same (i.e., each time-of-flight is equally important), $\lambda_n = 0.5$ for all $n \geq 0$ [satisfying $\sum_{n\geq 0} \lambda_n(1-\lambda_n) = \infty$], and $\gamma = 1$.

As is shown in Section 3.3, using only C_{velocity} as the hard-constraint set is not sufficient to obtain an accurate sound velocity distribution; thus other constraints are needed. A second method utilizing the B-mode image information is proposed. Consider a B-mode image in which an object contains an ROI surrounded by the background. Suppose that this ROI can be identified and segmented, then different constraints can be imposed in the ROI and the background. In other words, the following property set can be generated and used as another hard-constraint set:

$$C_{\text{image}} = \begin{cases} \left\{ \begin{array}{c} \mathbf{x} \in \mathbf{R}^{MN} : x_{b_1} = x_{b_2} = \cdots = x_{b_{N_\text{b}}}, x_{r_1} = x_{r_2} = \cdots = x_{r_{N_\text{r}}}, \\ x_{br_i} \in \left[x_{b_1}, x_{r_1} \right], 1 \le i \le N_\text{br} \end{array} \right\} \text{if } x_{b_1} \le x_{r_1} \\ \left\{ \begin{array}{c} \mathbf{x} \in \mathbf{R}^{MN} : x_{b_1} = x_{b_2} = \cdots = x_{b_{N_\text{b}}}, x_{r_1} = x_{r_2} = \cdots = x_{r_{N_\text{r}}}, \\ x_{br_i} \in \left[x_{r_1}, x_{b_1} \right], 1 \le i \le N_\text{br} \end{array} \right\} \text{otherwise} \end{cases}, \quad (2.16)$$

where $I_\text{b} \equiv \{b_1, b_2, \cdots, b_{N_\text{b}}\}$ is the background index set, $I_\text{r} \equiv \{r_1, r_2, \cdots, r_{N_\text{r}}\}$ is the ROI index set, and $I_\text{br} \equiv \{br_1, br_2, \cdots, br_{N_\text{br}}\}$ is the boundary index set. (2.16) means that all the slowness values in the background must be the same, and all the slowness values in the ROI must also be the same. In addition, each slowness value at the boundary must be between that of the background and that of the ROI. Note that no specific slowness value has been set in any region at this point. Also note that C_image, which contains all the slowness distributions that satisfy the constraint derived from the B-mode image, is also closed and convex. The C_image can be similarly generated when the object contains more ROIs. A slowness distribution $\mathbf{x} \in C_\text{velocity} \bigcap C_\text{image}$ minimizing $\Phi^\text{s}_\text{TOF}(\mathbf{x})$ can be found by taking $\mathbf{x}$ as the limit of the sequence $\{\mathbf{x}_n\}$ (i.e., $\lim_{n\to\infty} \mathbf{x}_n$). $\mathbf{x}_0 \in C_\text{velocity} \bigcap C_\text{image}$ is an initial slowness distribution, and

$$\mathbf{x}_{n+1} = (1-\lambda_n)\mathbf{x}_n + \lambda_n P_{C_\text{velocity} \cap C_\text{image}} \left[(1-\gamma)\mathbf{x}_n + \gamma \sum_{i=1}^{N_\text{A}(N_\text{A}+1)/2} w_i P_{C_{\Delta t_i}}(\mathbf{x}_n) \right], n \ge 0 . \quad (2.17)$$

This algorithm is called Algorithm II, which differs from Algorithm I only in the projector outside the brackets (i.e., the slowness distribution must be in the hard-constraint set C_image in addition to being in C_velocity in Algorithm II). The critical issue of the proposed method is the incorporation of C_image, which is shown in Section 3.4 to be crucial to the quality of the reconstructed sound velocity distribution.

A sound velocity distribution $\mathbf{c} = [c_1 \quad c_2 \quad \cdots \quad c_{MN}]^\text{T}$ and a slowness

distribution $\Delta\mathbf{s} = \begin{bmatrix} \Delta s_1 & \Delta s_2 & \cdots & \Delta s_{MN} \end{bmatrix}^{\mathrm{T}}$ are related as follows:

$$c_l = \left(s_0 + \Delta s_l\right)^{-1}, l = 1,2,\cdots,MN\,. \tag{2.18}$$

Chapter 3 Numerical results—sound velocity

In this chapter, simulations were performed to test the efficacy of the proposed technique. All the raw data generated in this chapter were noise free. However, the effects of wave propagation such as refraction and diffraction were included in the simulated data. The B-mode images were simulated using a *k*-space method [33], and the time-of-flight data were generated using the series solution to the scattering of a plane wave incident on a fluid cylinder [34]. These data were used to test Algorithm I and Algorithm II introduced in Section 2.3.

3.1 B-mode image generation

All B-mode images in this chapter were generated with a *k*-space method proposed by Tabei *et al.* [33]. This method solves the coupled first-order linear acoustic propagation equations for a fluid medium and allows inclusion of relaxation absorption and perfectly matched layers. It enables accurate calculation of scattering in soft tissues, and therefore simulated speckle images can be formed. Furthermore, diffraction, refraction, and scattering in an inhomogeneous medium are all accounted for. A brief description of the *k*-space method is included below.

The coupled first-order linear acoustic propagation equations for a two-dimensional fluid medium with perfectly matched layers and relaxation absorption [35] are

$$\rho(\mathbf{r})\left(\frac{\partial u_x(\mathbf{r},t)}{\partial t}+\alpha_x(\mathbf{r})u_x(\mathbf{r},t)\right)=-\frac{\partial p(\mathbf{r},t)}{\partial x}, \tag{3.1}$$

$$\rho(\mathbf{r})\left(\frac{\partial u_y(\mathbf{r},t)}{\partial t}+\alpha_y(\mathbf{r})u_y(\mathbf{r},t)\right)=-\frac{\partial p(\mathbf{r},t)}{\partial y}, \tag{3.2}$$

$$\kappa(\mathbf{r},t)\otimes\left(\frac{\partial p_x(\mathbf{r},t)}{\partial t}+\alpha_x(\mathbf{r})p_x(\mathbf{r},t)\right)=-\frac{\partial u_x(\mathbf{r},t)}{\partial x}, \tag{3.3}$$

$$\kappa(\mathbf{r},t)\otimes\left(\frac{\partial p_y(\mathbf{r},t)}{\partial t}+\alpha_y(\mathbf{r})p_y(\mathbf{r},t)\right)=-\frac{\partial u_y(\mathbf{r},t)}{\partial y}, \tag{3.4}$$

where $\mathbf{r}=(x,y)$ is the Cartesian coordinate, (u_x,u_y) is the acoustic particle velocity fluctuation, $p(\mathbf{r},t)=p_x(\mathbf{r},t)+p_y(\mathbf{r},t)$ is the acoustic pressure fluctuation, $\rho(\mathbf{r})$ is the density of the medium, $\alpha_x(\mathbf{r})$ and $\alpha_y(\mathbf{r})$ are dispersionless absorption parameters employed only within the perfectly matched layers, the $\otimes$ operator denotes temporal convolution, and $\kappa(\mathbf{r},t)$ is the generalized compressibility defined as

$$\kappa(\mathbf{r},t)=\kappa_\infty(\mathbf{r})\delta(t)+\sum_{q=1}^{N_r}\frac{\kappa_q(\mathbf{r})}{\tau_q(\mathbf{r})}\exp\left[-t/\tau_q(\mathbf{r})\right]H(t), \tag{3.5}$$

where $\kappa_\infty(\mathbf{r})=1/\left[\rho(\mathbf{r})c_\infty^2(\mathbf{r})\right]$, $c_\infty(\mathbf{r})=\lim_{f\to\infty}c(\mathbf{r},f)$ is the sound velocity of the medium when the temporal frequency f approaches infinity, $\tau_q(\mathbf{r})$ is the relaxation time for the q th relaxation process, $\kappa_q(\mathbf{r})$ is the relaxation modulus for the q th order relaxation process, $\delta(t)$ is the Dirac delta function, and $H(t)$ is the Heaviside step function. By introducing state variables

$$S_q^{(\cdot)}(\mathbf{r},t)\equiv\left(\frac{\exp\left[-t/\tau_q(\mathbf{r})\right]}{\tau_q(\mathbf{r})}H(t)\right)\otimes p_{(\cdot)}(\mathbf{r},t), \tag{3.6}$$

where $(\cdot)$ denotes x or y, (3.1)–(3.4) can be solved by a temporal iteration scheme. The discrete field equations are

$$u_x(\mathbf{r}_1,t^+)=e^{-\alpha_x(\mathbf{r}_1)\Delta t/2}\left[e^{-\alpha_x(\mathbf{r}_1)\Delta t/2}u_x(\mathbf{r}_1,t^-)-\frac{\Delta t}{\rho(\mathbf{r}_1)}\frac{\partial p(\mathbf{r},t)}{\partial^{(c_0\Delta t)^+}x}\right], \tag{3.7}$$

$$u_y(\mathbf{r}_2,t^+)=e^{-\alpha_y(\mathbf{r}_2)\Delta t/2}\left[e^{-\alpha_y(\mathbf{r}_2)\Delta t/2}u_y(\mathbf{r}_2,t^-)-\frac{\Delta t}{\rho(\mathbf{r}_2)}\frac{\partial p(\mathbf{r},t)}{\partial^{(c_0\Delta t)^+}y}\right], \tag{3.8}$$

$$p_x(\mathbf{r},t+\Delta t)=e^{-\mu_x(\mathbf{r})\Delta t/2}\left[e^{-\mu_x(\mathbf{r})\Delta t/2}p_x(\mathbf{r},t)-\frac{\Delta t}{\kappa_\infty(\mathbf{r})}\times\left(\frac{\partial u_x(\mathbf{r}_1,t^+)}{\partial^{(c_0\Delta t)^-}x}-\sum_{q=1}^{N_r}v_q^x(\mathbf{r})S_q^x(\mathbf{r},t^+)\right)\right], \tag{3.9}$$

$$p_y(\mathbf{r},t+\Delta t)=e^{-\mu_y(\mathbf{r})\Delta t/2}\left[e^{-\mu_y(\mathbf{r})\Delta t/2}p_y(\mathbf{r},t)-\frac{\Delta t}{\kappa_\infty(\mathbf{r})}\times\left(\frac{\partial u_y(\mathbf{r}_2,t^+)}{\partial^{(c_0\Delta t)^-}y}-\sum_{q=1}^{N_r}v_q^y(\mathbf{r})S_q^y(\mathbf{r},t^+)\right)\right], \tag{3.10}$$

$$S_q^x(\mathbf{r},t^+)=e^{-\Delta t/[2\tau_q(\mathbf{r})]}\left[e^{-\Delta t/[2\tau_q(\mathbf{r})]}S_q^x(\mathbf{r},t^-)-\Delta t\frac{p_x(\mathbf{r},t)}{\tau_q(\mathbf{r})}\right], \tag{3.11}$$

$$S_q^y(\mathbf{r},t^+)=e^{-\Delta t/[2\tau_q(\mathbf{r})]}\left[e^{-\Delta t/[2\tau_q(\mathbf{r})]}S_q^y(\mathbf{r},t^-)-\Delta t\frac{p_y(\mathbf{r},t)}{\tau_q(\mathbf{r})}\right], \tag{3.12}$$

where Δt is the temporal increment at each iteration, $t^+=t+\Delta t/2$, $t^-=t-\Delta t/2$, $\mathbf{r}_1=(x+\Delta x/2,y)$, $\mathbf{r}_2=(x,y+\Delta y/2)$, Δx and Δy are the spatial sampling intervals in the x and y directions, respectively,

$$\mu_{(\cdot)}(\mathbf{r})\equiv\frac{1}{\kappa_\infty(\mathbf{r})}\sum_{q=1}^{N_r}\frac{\kappa_q(\mathbf{r})}{\tau_q(\mathbf{r})}+\alpha_{(\cdot)}(\mathbf{r}), \tag{3.13}$$

$$v_q^{(\cdot)}(\mathbf{r})\equiv\frac{\kappa_q(\mathbf{r})}{\tau_q(\mathbf{r})}-\kappa_q(\mathbf{r})\alpha_{(\cdot)}(\mathbf{r}), \tag{3.14}$$

and

$$\frac{\partial p(\mathbf{r},t)}{\partial^{(c_0\Delta t)^+}x}\equiv\mathbf{F}^{-1}\left\{jk_x\exp(jk_x\Delta x/2)\sin c(c_0\Delta tk/2\pi)\mathbf{F}\left[p(\mathbf{r},t)\right]\right\}, \tag{3.15}$$

$$\frac{\partial p(\mathbf{r},t)}{\partial^{(c_0\Delta t)^+}y}\equiv\mathbf{F}^{-1}\left\{jk_y\exp(jk_y\Delta y/2)\sin c(c_0\Delta tk/2\pi)\mathbf{F}\left[p(\mathbf{r},t)\right]\right\}, \tag{3.16}$$

$$\frac{\partial u_x(\mathbf{r}_1,t^+)}{\partial^{(c_0\Delta t)^-}x}\equiv\mathbf{F}^{-1}\left\{jk_x\exp(-jk_x\Delta x/2)\sin c(c_0\Delta tk/2\pi)\mathbf{F}\left[u_x(\mathbf{r}_1,t^+)\right]\right\}, \tag{3.17}$$

$$\frac{\partial u_y(\mathbf{r}_1,t^+)}{\partial^{(c_0\Delta t)^-} y} \equiv \mathbf{F}^{-1}\left\{jk_y \exp(-jk_y\Delta y/2)\sin c(c_0\Delta t k/2\pi)\mathbf{F}\left[u_y(\mathbf{r}_1,t^+)\right]\right\}, \qquad (3.18)$$

where $\mathbf{F}$ and $\mathbf{F}^{-1}$ represent the spatial Fourier transform and inverse Fourier transform, respectively, $\mathbf{k}=(k_x,k_y)$ is the wave vector, $k=\sqrt{k_x^2+k_y^2}$, and c_0 is the c_∞ value of the background.

All simulation data were generated under MATLAB (Mathworks, Natick, MA). The FFTW routine was also adopted [36] for the fast Fourier transform in order to make the *k*-space method more computationally efficient. The hardware platform was a personal computer with a 2.4 GHz Pentium 4 CPU and a total RAM of 1.5 gigabytes. Obtaining a complete channel data set $\{e_{ij}(t)\}, 1\le i,j\le N_A$, requires N_A firings, which in general is very time consuming. In order to reduce the computation time, only eight firings are used per image, with all channels receiving to generate a B-mode image using a synthetic aperture approach. It took about one day to generate the required data for each case.

3.2 Generation of the time-of-flight data

The simulation time can be reduced by generating the time-of-flight data without simulating the channel data. In this case, the time-consuming *k*-space method is replaced by the series solution to the scattering of a plane wave incident on a fluid cylinder [34]. The details of this method are provided below.

With reference to Fig. 3.1(a), consider the following problem: An acoustic wave $w(x,y;t)$ propagates along the $+y$ direction in a linear fluid medium that has background physical parameters $(\rho_0, c_0(f))$—where ρ is the density, c is the sound velocity, and f is the temporal frequency—and contains a cylinder with physical parameters $(\rho_1, c_1(f))$, radius a, and centered at (x_1, y_1). Assuming that attenuation can be ignored and that $w(x,0;t)$ is known, find $w(x,y_2;t)$.

Because the medium is linear, the above problem is equivalent to the following: find $W(x,y_2;f)$ assuming that $W(x,0;f)$ is known, where $W(x,0;f)$ and $W(x,y_2;f)$ are the temporal Fourier transforms of $w(x,0;t)$ and $w(x,y_2;t)$, respectively. It has been shown that if $W(x,y;f)$ represents an incident plane wave,

then there exists an exact series solution for $W(x, y_2; f)$ [34].

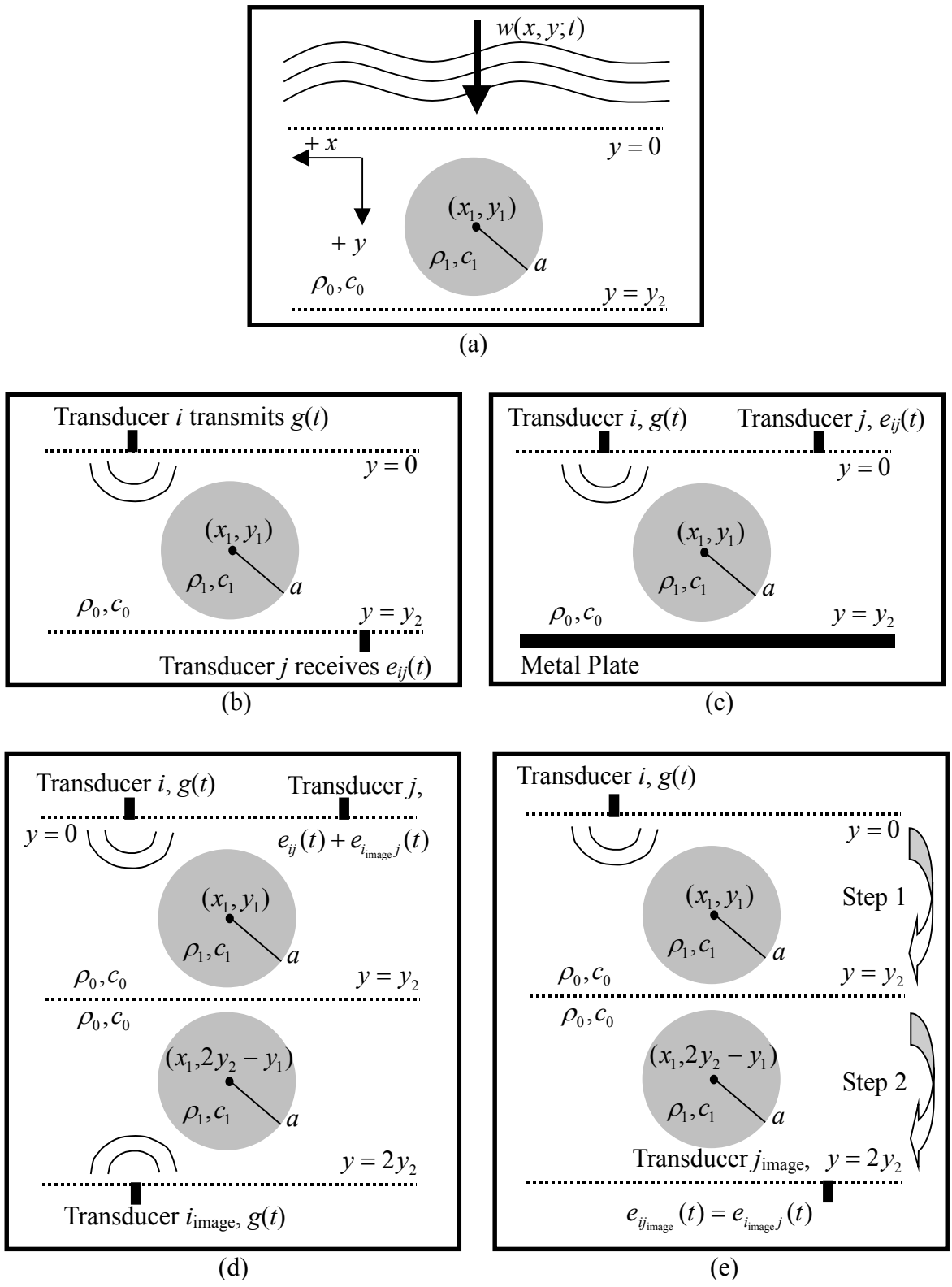

Fig. 3.1. Illustration of time-of-flight data generation (see text for details).

Let the angular spectrum of $W(x,0;f)$ be $\tilde{W}(k_x;0,f)$ [37], i.e.,

$$W(x,0;f)=\frac{1}{2\pi}\int \widetilde{W}(k_x;0,f)\exp(jk_x x)dk_x \ . \tag{3.19}$$

Except for those complex-exponential functions $\exp(jk_x x)$ with $|k_x| > 2\pi f / c_0(f)$, which represent evanescent waves, each $\exp(jk_x x)$ represents a plane wave propagating with the wave vector $\left(k_x, \sqrt{(2\pi f / c_0(f))^2 - k_x^2}\right)$. Thus

$$W(x,y_2;f) \cong \frac{1}{2\pi}\int_{-2\pi f / c_0(f)}^{2\pi f / c_0(f)} \widetilde{W}'(k_x;x,y_2,f)dk_x \ , \tag{3.20}$$

where $\widetilde{W}'(k_x;x,y_2,f)$ is the series solution corresponding to the term $\widetilde{W}(k_x;0,f)\exp(jk_x x)$.

For the configuration in Fig. 3.1(b), the method for calculating the signal, $e_{ij}(t)$, received by transducer j in the lower array when transducer i in the upper array transmits a short pulse $g(t)$ can be obtained based on the above discussion. To treat the case shown in Fig. 3.1(c), let the metal plate have physical parameters $(\rho_{\mathrm{m}}, c_{\mathrm{m}}(f))$ and assume that $\rho_{\mathrm{m}} >> \rho_0$ and $c_{\mathrm{m}}(f) >> c_0(f)$ so that the method of images can be adopted. If the plate is sufficiently thick such that the echoes from its upper and lower surfaces are well separated, then the plate can be treated as infinitely thick and $e_{ij}(t)$ in Fig. 3.1(c) is equal to $e_{ij}(t) + e_{i_{\mathrm{image}}j}(t)$ in Fig. 3.1(d). Furthermore, $e_{ij}(t)$ in Fig. 3.1(d) is negligible around $t = t_{ij}$ in Fig. 3.1(c) [t_{ij} is the time-of-flight and is the time needed for $g(t)$ to travel from transducer i to the metal plate, then to transducer j in Fig. 3.1(c)]. That is, when only t_{ij} is of interest, there is no need to calculate $e_{ij}(t)$ since $e_{ij}(t)$ can at most contain scattered waves relevant to transducer i around t_{ij} and thus neglecting transducer i does not alter the estimate of t_{ij}. Therefore, to obtain t_{ij} one only needs to consider the configuration in Fig. 3.1(e). Note that $e_{ij_{\mathrm{image}}}(t) = e_{i_{\mathrm{image}}j}(t)$. Obtaining $e_{ij_{\mathrm{image}}}(t)$ around t_{ij} is a

two-step process: the wave first propagates from plane $y = 0$ to plane $y = y_2$, and then propagates from plane $y = y_2$ to plane $y = 2y_2$. This method can still be applied when the object contains more cylinders with a circular cross section.

Note that there are limitations associated with this approach: relaxation absorption cannot be fully taken into consideration, and the medium can contain only cylindrical targets with a circular cross section. Nonetheless, a case (which is the same as the $1\times$ case in Section 3.3 except for the absence of relaxation absorption) was used for verification. The results show that the differences in time-of-flight between this method and the *k*-space method can be ignored.

3.3 Reconstruction without the B-mode image: Algorithm I

Conventional ultrasonic transmission tomography acquires complete projection data over an angular range of 180° [22], so that the reconstruction quality will be degraded if the data set does not span the full 180°. The more data are missing, the poorer the resulting reconstruction quality becomes [38]–[40].

Limited-angle transmission tomography using linear arrays does not provide a complete data set. As shown in Fig. 3.2(a), the incidence and reflection angles are both equal to θ. Collecting all the time-of-flight data with an angle of incidence of θ in Fig. 3.2(a) is effectively equal to inspecting the object at angle θ and angle $-\theta$ simultaneously in conventional transmission tomography, as shown in Fig. 3.2(b). To have a complete data set, the maximal available θ, denoted by $\theta_{\max}$, has to be 90°. This is impossible with a linear array. Assume that the array has N_A transducers, a pitch of p_A, and a distance between the array and the metal plate of D_A, then it can be easily shown that

$$\theta_{\max} = \tan^{-1}\left[\frac{(N_A - 1)p_A}{2D_A}\right]. \tag{3.21}$$

A typical $\theta_{\max}$ is 26.6° with $D_A = 35\,\text{mm}$ and $(N_A - 1)p_A = 35\,\text{mm}$. Note that the data at $\theta_{\max}$ are not complete since only one time-of-flight can be collected at this angle. Also note that $(N_A - 1)p_A$ is close to the array width $N_A p_A$. Thus, in

limited-angle transmission tomography, obtaining a large $\theta_{\max}$ is only possible with a large linear array, and hence the effect of the array size on reconstruction accuracy needs to be evaluated.

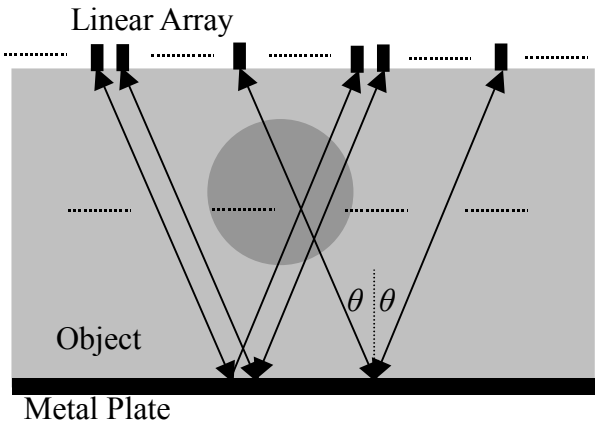

(a)

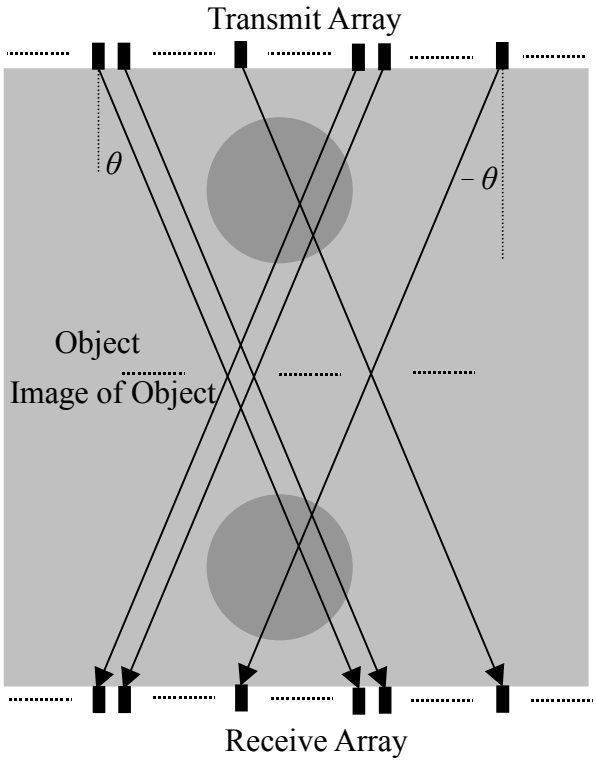

(b)

Fig. 3.2. (a) Collecting all the time-of-flight data with the angle of incidence of θ is equivalent to (b) inspecting the object at angle θ and angle $-\theta$ simultaneously in conventional transmission tomography.

Consider the configuration shown in Fig. 3.2(a). The image object consists of a

background of glandular material with a cylinder of fat with a radius of 4 mm at its center. The corresponding parameters of the different materials are listed in Table 3.1 [12], [19]. Each array channel has a Gaussian frequency response with a center frequency of 5 MHz and a two-way $-12\,\text{dB}$ fractional bandwidth of 0.6. All array elements are assumed to be a line source. The pitch is $p_A = 0.45\,\text{mm}$ and the distance is $D = 35\,\text{mm}$. Sound velocity distributions were reconstructed in three cases corresponding to N_A values of $312\,(4\times)$, $156\,(2\times)$ and $78\,(1\times)$.

Table 3.1. Parameters used in Fig. 3.2(a).

Material	Sound velocity c_∞ (m/s)	Density ρ $\left(\text{g/cm}^3\right)$	Absorption β at 5 MHz (dB/cm)	$\tau_1 = 20\,\text{ns}$ $(\kappa_1/\kappa_\infty)\times 10^3$	$\tau_2 = 200\,\text{ns}$ $(\kappa_2/\kappa_\infty)\times 10^3$
Glandular	1521	1.05	5.68	10.76	10.34
Fat	1471	0.94	2.68	4.91	4.72
Tumor	1549	1.12	7.39	14.27	13.71

$c_\infty \equiv \lim_{f\to\infty} c(f)$. At f = 5 MHz the sound velocities are 1515.0 m/s, 1468.3 m/s, and 1542.7 m/s in glandular tissue, fat, and tumor, respectively.

The time-of-flight data were first generated using the method described in Section 3.2. The attenuation resulting from relaxation absorption was neglected but the dependency of sound velocity c on frequency f, also resulting from relaxation absorption, was taken into account by the following equation [35]:

$$c(f) = \sqrt{\frac{2}{\rho}}\left\{\kappa_\infty + \sum_{q=1}^{2}\frac{\kappa_q}{1+4\pi^2\tau_q^2 f^2} + \left[\left(\kappa_\infty + \sum_{q=1}^{2}\frac{\kappa_q}{1+4\pi^2\tau_q^2 f^2}\right)^2 + \left(\sum_{q=1}^{2}\frac{2\pi\kappa_q\tau_q f}{1+4\pi^2\tau_q^2 f^2}\right)^2\right]^{\frac{1}{2}}\right\}^{-\frac{1}{2}}, \tag{3.22}$$

where ρ is the density of the medium, $\kappa_\infty = 1/\rho c_\infty^2$, c_∞ is the sound velocity of the medium when the temporal frequency f approaches infinity, τ_q is the relaxation time for the q th order relaxation process, and κ_q is the relaxation modulus for the q th order relaxation process. Fig. 3.3(a) shows all the receive envelope data when the 39th channel was used on transmit in the $1\times$ case with geometrical delays compensated. The corresponding time-of-flight was extracted from

the envelope based on the center of gravity of the square of the envelope (i.e., the center of gravity with the square of the envelope as its density distribution function) around the peak. Note that the cylinder of fat introduced both time-of-flight errors and waveform distortion. The presence of severe waveform distortion will make it difficult to determine a reliable time-of-flight, and thus this signal should be dropped. In this chapter, all cases followed the rule below except for the $4\times$ case. Let E_{ij} denote the energy of the signal around the time-of-flight t_{ij} received by channel j when channel i is transmitted. Then t_{ij} (and Δt_{ij}) is dropped if

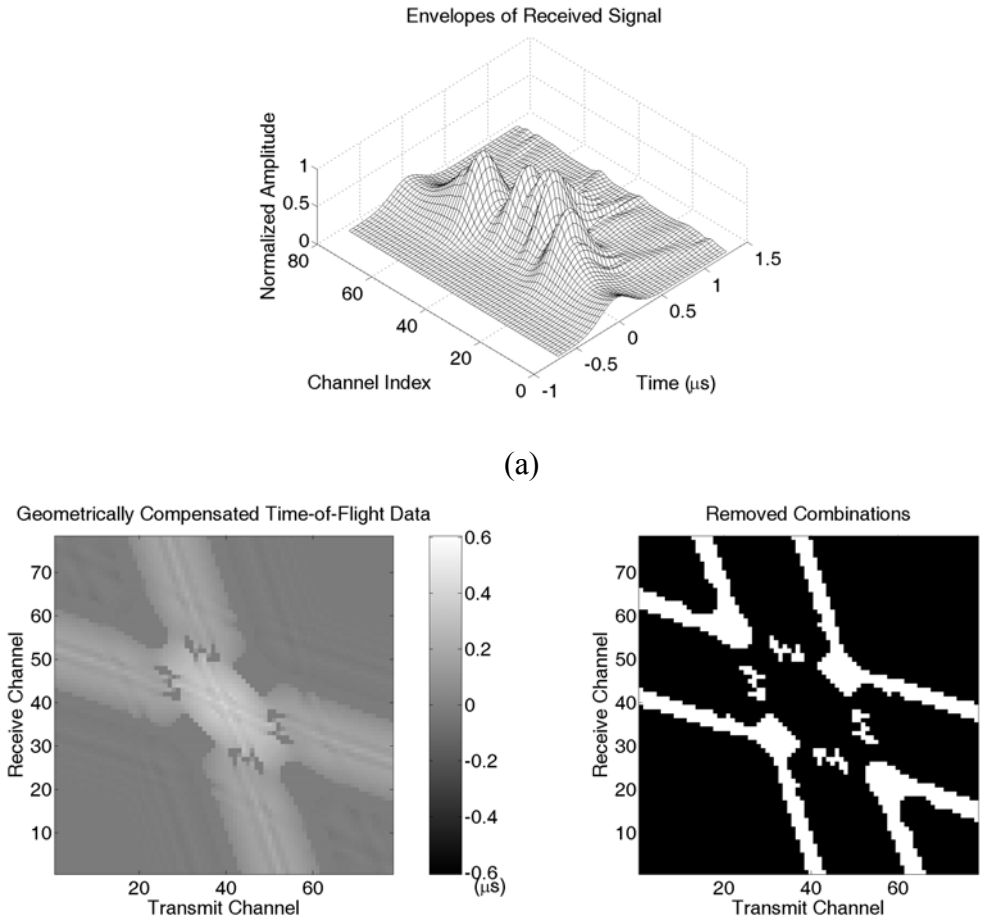

(a)

(b) (c)

Fig. 3.3. (a) The envelopes of the received signals when the 39th channel is transmitted in the $1\times$ case. Geometrical delays have been compensated. The attenuation resulting from relaxation absorption was neglected but the dependency of sound velocity c on frequency f, also resulting from relaxation absorption, was taken into account. (b) The geometrically compensated time-of-flight data in the $1\times$ case. Note that all the removed Δt_{ij} data values are replaced by 0. (c) White at position (i, j) means that the associated Δt_{ij} was removed.

$$E_{ij} < 0.25 \frac{1}{N_{\mathrm{A}}} \sum_{q=1}^{N_{\mathrm{A}}} E_{iq} \,. \tag{3.23}$$

In the $4\times$ case, the t_{ij} data were inspected manually when $1 \le i \le 70, 243 \le j \le 312$, or $243 \le i \le 312, 1 \le j \le 70$, because their corresponding envelopes were not severely distorted despite the energy being low. The geometrically compensated time-of-flight data in the $1\times$ case are shown in Fig. 3.3(b). Note that all the removed Δt_{ij} data values were replaced by 0. The removed transmit/receive combinations are shown in Fig. 3.3(c) in white.

After the time-of-flight data were obtained, sound velocity distributions in the central 35-mm width were reconstructed using Algorithm I (Fig. 3.4). Here, the sampling intervals Δx_{s} and Δy_{s} of the sound velocity distribution in the x and y directions were both 1 mm. The other parameters were $c_{\mathrm{lower}} = 1450$ m/s and $c_{\mathrm{upper}} = 1580$ m/s. Fig. 3.4(a) and (b), Fig. 3.4(c) and (d), and Fig. 3.4(e) and (f) display the results for $4\times$, $2\times$, and $1\times$, respectively. The reconstructed sound velocity distribution is shown in the left panels over a range from 1450 m/s to 1580 m/s, and the sound velocity error is shown in the right panels over a range from 0 m/s to 65 m/s. The sound velocity error is defined as the absolute value of the difference between the reconstructed sound velocity and the true sound velocity at 5 MHz (i.e., the transmit center frequency). It is obvious that with a larger array the sound velocity distribution can be reconstructed more accurately. To quantify the accuracy, define

$$\left|\Delta c\right| = \frac{1}{N_{\mathrm{fat}}} \sum_{(m,n)\in I_{\mathrm{f}}} \left| c(m,n) - c_{\mathrm{f,true}} \right|, \tag{3.24}$$

where $c(m,n)$ is the reconstructed sound velocity, $c_{\mathrm{f,true}} = 1468.3$ m/s is the true sound velocity at 5 MHz in the fat region, I_{f} is the index set containing all coordinates (m,n) of a rectangle locating entirely in the fat region, and N_{fat} is the number of elements in I_{f}. A smaller $\left|\Delta c\right|$ indicates higher accuracy. The $\left|\Delta c\right|$ values in the $4\times$, $2\times$, and $1\times$ cases were 11.8, 19.9, and 28.5 m/s, respectively.

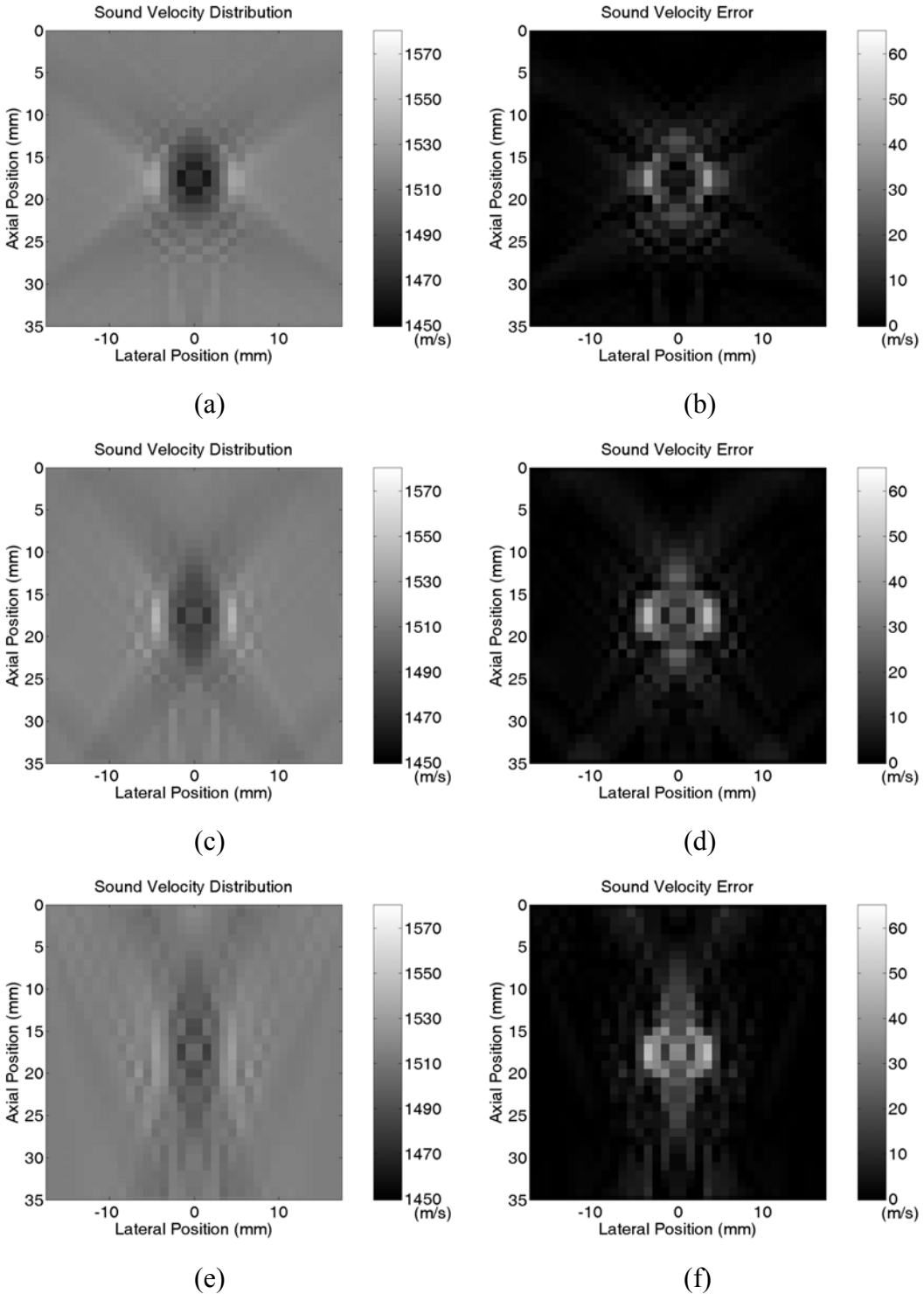

Fig. 3.4. (a), (c), (e) Sound velocity distributions in the central 35-mm width in the 4×, 2×, and 1× cases, respectively. (b), (d), (f) Reconstruction errors in the central 35-mm width in the 4×, 2×, and 1× cases, respectively. Algorithm I was employed; therefore, no B-mode image information was used. Note that absolute values of the errors are displayed. Also note that these results using Algorithm I are inferior to those of Algorithm II, as shown in the following figures.

The 4× case outperformed the 2× and 1× cases, but the array used in that

case is too large ($N_A p_A = 140.4\,\text{mm}$) and may not be clinically useful. On the other hand, the value of θ_{max} in the $4\times$ case is only 63.4°. In other words, the time-of-flight data for the $4\times$ case is far from a complete data set. Therefore, increasing the array size to enhance the quality of sound velocity distribution is impractical in limited-angle transmission tomography.

3.4 Reconstruction with the B-mode image information: Algorithm II

With only the time-of-flight data and the general constraints on the sound velocity, Section 3.3 shows that the accuracy of the sound velocity estimation is insufficient. This subsection uses Algorithm II, introduced in Section 2.3, in order to improve this. In this case, constraints are derived from the B-mode image and these are incorporated in the algorithm. The time-of-flight data were generated in the same way as described in Section 3.3.

Consider again the configuration shown in Fig. 3.2(a). In all cases shown below an array with $N_A = 234$ and $p_A = 0.15\,\text{mm}$ (giving an array width of $N_A p_A = 35.1\,\text{mm}$) was used. When generating the time-of-flight data, only every third channel both on transmit and receive in the array was used. The distance D_A between the array and the metal plate was 35 mm. The other parameters were $c_{lower} = 1450\,\text{m/s}$, $c_{upper} = 1580\,\text{m/s}$, $\Delta x_s = 0.5\,\text{mm}$, and $\Delta y_s = 0.5\,\text{mm}$.

The *k*-space method introduced in Section 3.1 was employed to generate all the B-mode images in this chapter. The pixel sizes used in the *k*-space method and the B-mode images are both 0.04 mm by 0.04 mm. Random perturbations to densities in different regions were introduced to produce speckle images since they can introduce acoustic impedance mismatches and therefore cause scattering. Spatial compounding [41] was then applied to reduce the speckle intensity variations before segmentation was subsequently applied. To reduce the computation time, only eight channels (channels 27, 53, 79, 105, 130, 156, 182, and 208) were used on transmit, and only receive channels with j values obeying $|j-i| \le 26$ were used on receive when channel i was fired. One subimage per transmit was reconstructed, and all eight

subimages were compounded into a single image. To further reduce the speckle noise, the compound B-mode image was low-pass filtered using a two-dimensional Gaussian filter with a $1/e$ cutoff at 0.152 mm to generate the final B-mode image. Once the filtered B-mode image was obtained, a single threshold was applied for segmentation.

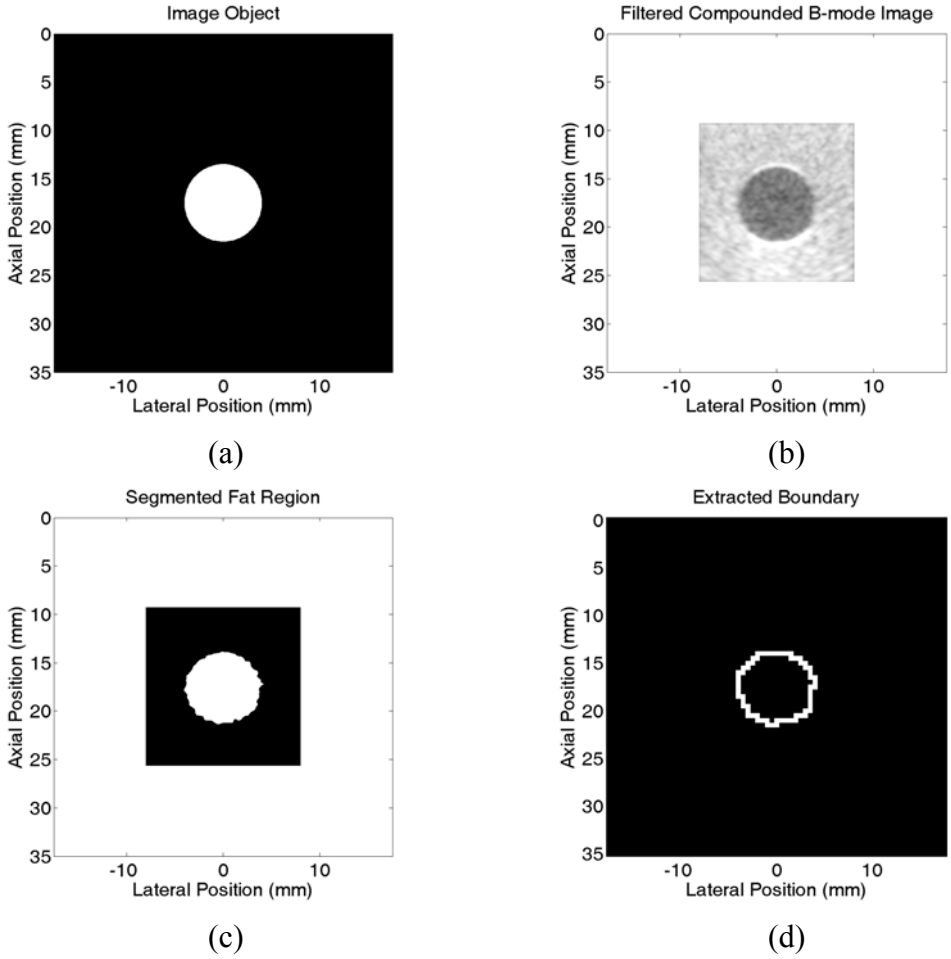

Fig. 3.5. (a) Image object comprising a background of glandular material with a cylinder of fat with a radius of 4 mm at its center. (b) B-mode image displayed with a 30-dB dynamic range. (c) Segmented fat region. (d) Boundary between the fat region and the background derived from the segmented fat region.

An object shown in Fig. 3.5(a) was considered first. It comprised a background of glandular material with a cylinder of fat with a radius of 4 mm at its center. The random perturbations added to the densities were 0.5% and 2.5% (root-mean-squared amplitude) for the cylinder and the background, respectively. The corresponding B-mode image is shown in Fig. 3.5(b). After applying a threshold to the processed B-mode image, the fat region was extracted as shown in Fig. 3.5(c). The boundary between the fat region and the background was directly derived from the segmented fat region by morphological dilation [42] (according to the disparity

between the segmented fat region and its dilated version) as shown in Fig. 3.5(d).

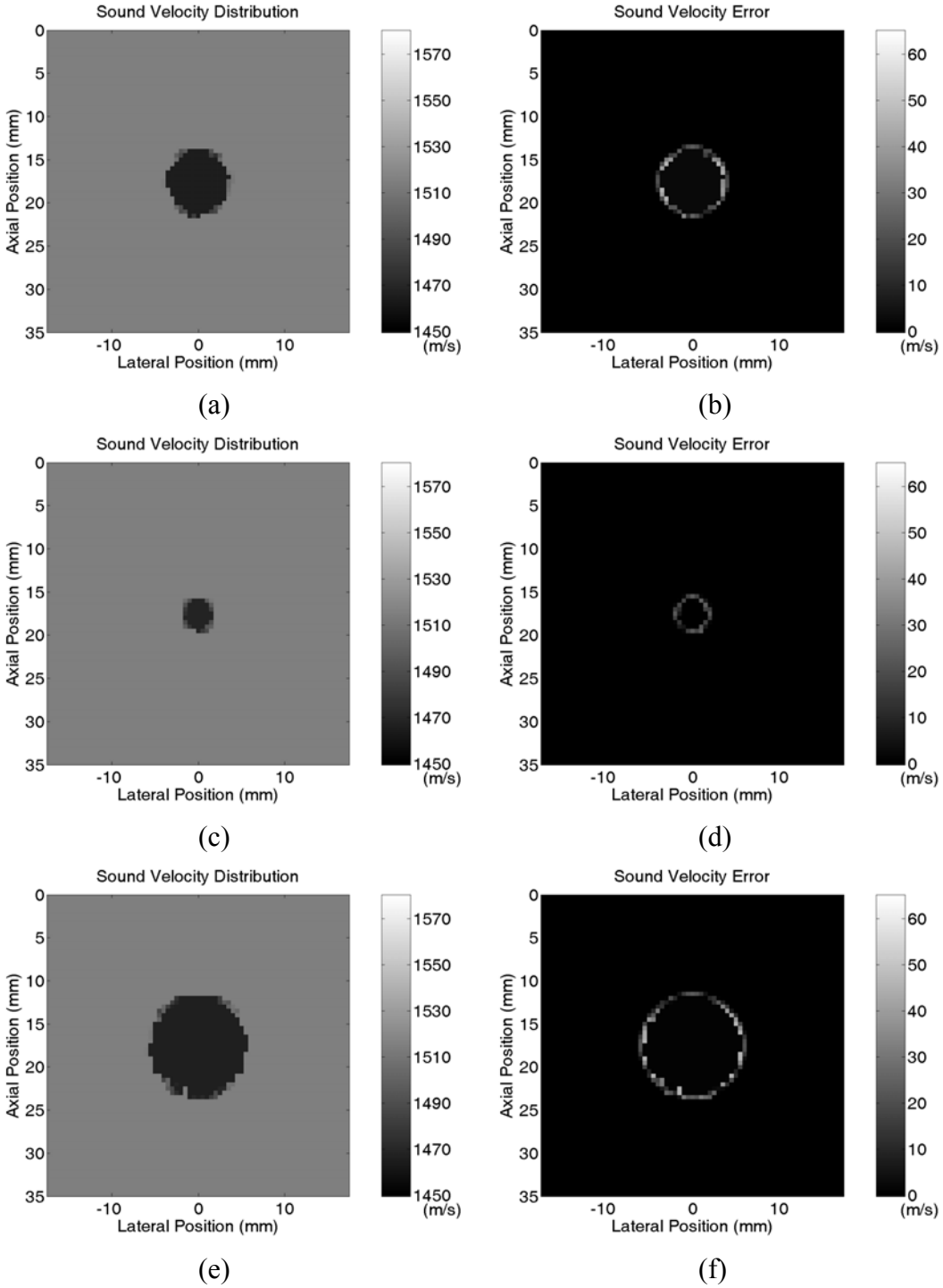

Fig. 3.6. Reconstructed sound velocity distributions and reconstruction errors. (a) and (b) Case i (cylinder radius = 4 mm, $c_{\mathrm{c,true}} = 1468.3\,\mathrm{m/s}$, and $c_{\mathrm{b,true}} = 1515.0\,\mathrm{m/s}$). (c) and (d) Case ii (cylinder radius = 2 mm, $c_{\mathrm{c,true}} = 1468.3\,\mathrm{m/s}$, and $c_{\mathrm{b,true}} = 1515.0\,\mathrm{m/s}$). (e) and (f) Case iii (cylinder radius = 6 mm, $c_{\mathrm{c,true}} = 1468.3\,\mathrm{m/s}$, and $c_{\mathrm{b,true}} = 1515.0\,\mathrm{m/s}$). Algorithm II was employed and hence the B-mode segmentation information was used. The simulation parameters are also listed in Table 3.2.

The reconstructed sound velocity distribution and the image of sound velocity error are shown in Fig. 3.6(a) and (b), respectively. This example is referred to as Case i in Table 3.2. The reconstructed sound velocity in the segmented fat region ($c_{\mathrm{c,recon}}$) is 1465.7 m/s, which is only 2.6 m/s slower than the true sound velocity of fat at 5 MHz ($c_{\mathrm{c,true}} = 1468.3\,\mathrm{m/s}$). Moreover, the reconstructed sound velocity in the background region, $c_{\mathrm{b,recon}}$, is the same as the true sound velocity of glandular material at 5 MHz ($c_{\mathrm{b,true}} = 1515.0\,\mathrm{m/s}$). Note that the subscripts c and b here stand for cylinder and background, respectively. Objects with different geometries and acoustic parameters were also evaluated. The parameters are summarized in Table 3.2 and the reconstructed results are shown in Fig. 3.6–Fig. 3.8 using Case i as the reference. In Fig. 3.6, effects of the size of the cylinder on the reconstruction accuracy are shown. In Fig. 3.7, the results correspond to different sound velocity in the cylinder. In Fig. 3.8, effects of the position of the cylinder in the axial dimension are demonstrated. Define errors as

$$\Delta c_{(\cdot)} = c_{(\cdot),\mathrm{recon}} - c_{(\cdot),\mathrm{true}}, \tag{3.25}$$

where $(\cdot)$ denotes b or c. In all cases, the errors in the background region were almost zero. However, the errors in the fat region were more significant. Also note that in all cases, larger errors occurred at boundaries. Fig. 3.6(a) and (b), Fig. 3.6(c) and (d), and Fig. 3.6(e) and (f) show the estimation results corresponding to cylinders with radii of 4 mm, 2 mm, and 6 mm, respectively. The left panels [Fig. 3.6(a), (c), and (e)] are the sound velocity distributions and the right panels [Fig. 3.6(b), (d), and (f)] are the sound velocity errors. The Δc_{c} values are –2.6 m/s, –0.1 m/s, and –1.4 m/s, respectively, and those of Δc_{b} are 0.0 m/s, 0.1 m/s, and 0.0 m/s, respectively. Fig. 3.7(a) and (b), Fig. 3.7(c) and (d), Fig. 3.7(e) and (f), and Fig. 3.7(g) and (h) show the sound velocity distributions and sound velocity errors corresponding to cylinders with sound velocities ($c_{\mathrm{c,true}}$) of 1468.3 m/s, 1493.2 m/s, 1505.8 m/s, and 1568.0 m/s, respectively. The Δc_{c} values are –2.6 m/s, –2.8 m/s, –2.5 m/s, and 2.0 m/s, respectively, and those of Δc_{b} are 0.0 m/s, 0.0 m/s, 0.0 m/s, and 0.1 m/s, respectively. Fig. 3.8(a) and (b), Fig. 3.8(c) and (d), and Fig. 3.8(e) and (f) show the sound velocity distributions and sound velocity errors corresponding to cylinders at different positions (center, upper, and lower, respectively). The Δc_{c} values are –2.6

m/s, –1.2 m/s, and –2.2 m/s, respectively, and those of Δc_b are all zero.

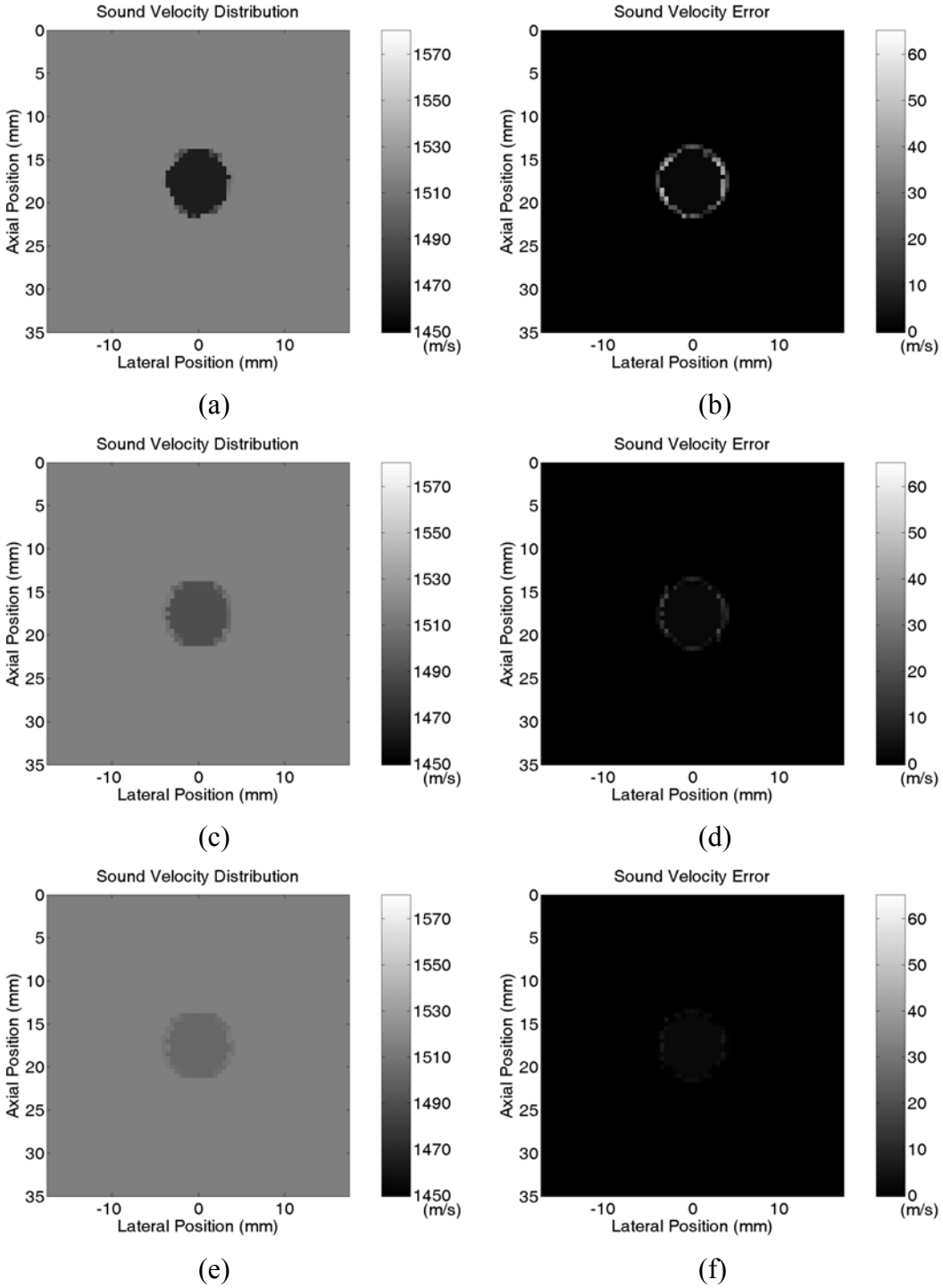

Fig. 3.7. Reconstructed sound velocity distributions and reconstruction errors. (a) and (b) Case i (cylinder radius = 4 mm, $c_{\mathrm{c,true}} = 1468.3$ m/s, and $c_{\mathrm{b,true}} = 1515.0$ m/s). (c) and (d) Case iv (cylinder radius = 4 mm, $c_{\mathrm{c,true}} = 1493.2$ m/s, and $c_{\mathrm{b,true}} = 1515.0$ m/s). (e) and (f) Case v (cylinder radius = 4 mm, $c_{\mathrm{c,true}} = 1505.8$ m/s, and $c_{\mathrm{b,true}} = 1515.0$ m/s). (g) and (h) Case vi (cylinder radius = 4 mm, $c_{\mathrm{c,true}} = 1568.0$ m/s, and $c_{\mathrm{b,true}} = 1515.0$ m/s). The simulation parameters are also listed in Table 3.2.

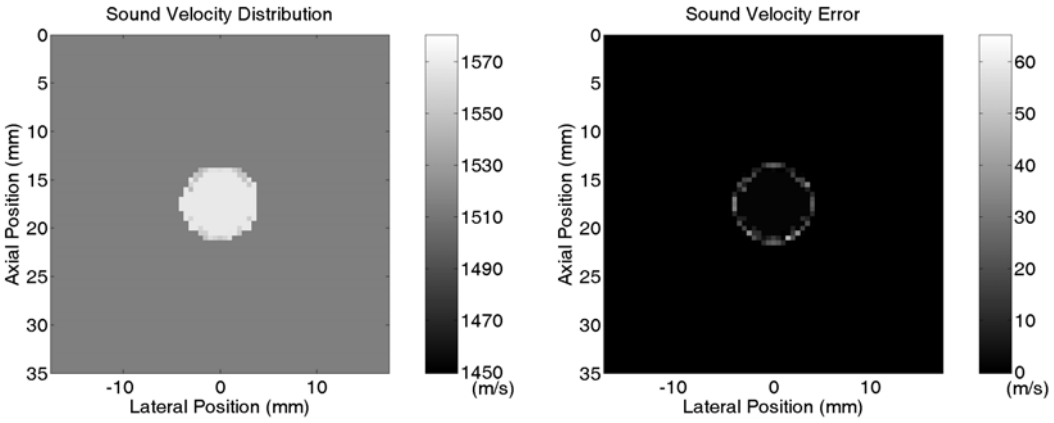

(g) (h)

Fig. 3.7. (Continued.)

Table 3.2. Parameters used in the cases shown in Fig. 3.6–Fig. 3.8 and the estimation results in simulations.

Case	$c_{\mathrm{c,true}}$ (m/s)	Cylinder radius (mm)	Δc_{c} (m/s)	$\Delta c_{\mathrm{c}}^{*}$ (m/s)	Δc_{b} (m/s)	$\Delta c_{\mathrm{b}}^{*}$ (m/s)	Cylinder position
i	1468.3	4	–2.6	1.5	0.0	0.1	Center
ii	1468.3	2	–0.1	5.8	0.1	0.1	Center
iii	1468.3	6	–1.4	0.4	0.0	0.0	Center
i	1468.3	4	–2.6	1.5	0.0	0.1	Center
iv	1493.2	4	–2.8	–0.1	0.0	0.0	Center
v	1505.8	4	–2.5	–1.3	0.0	0.0	Center
vi	1568.0	4	2.0	–5.6	0.1	0.0	Center
i	1468.3	4	–2.6	1.5	0.0	0.1	Center
vii	1468.3	4	–1.2	1.9	0.0	0.1	5.5 mm above the center
viii	1468.3	4	–2.2	1.3	0.0	0.0	5.5 mm below the center

Δc_{c} and Δc_{b} were obtained with the boundary derived from the B-mode images. $\Delta c_{\mathrm{b}}^{*}$ and $\Delta c_{\mathrm{c}}^{*}$ were obtained with the boundary set to perfectly match the original boundary. $c_{\mathrm{b,true}} = 1515.0\,\mathrm{m/s}$ in all cases.

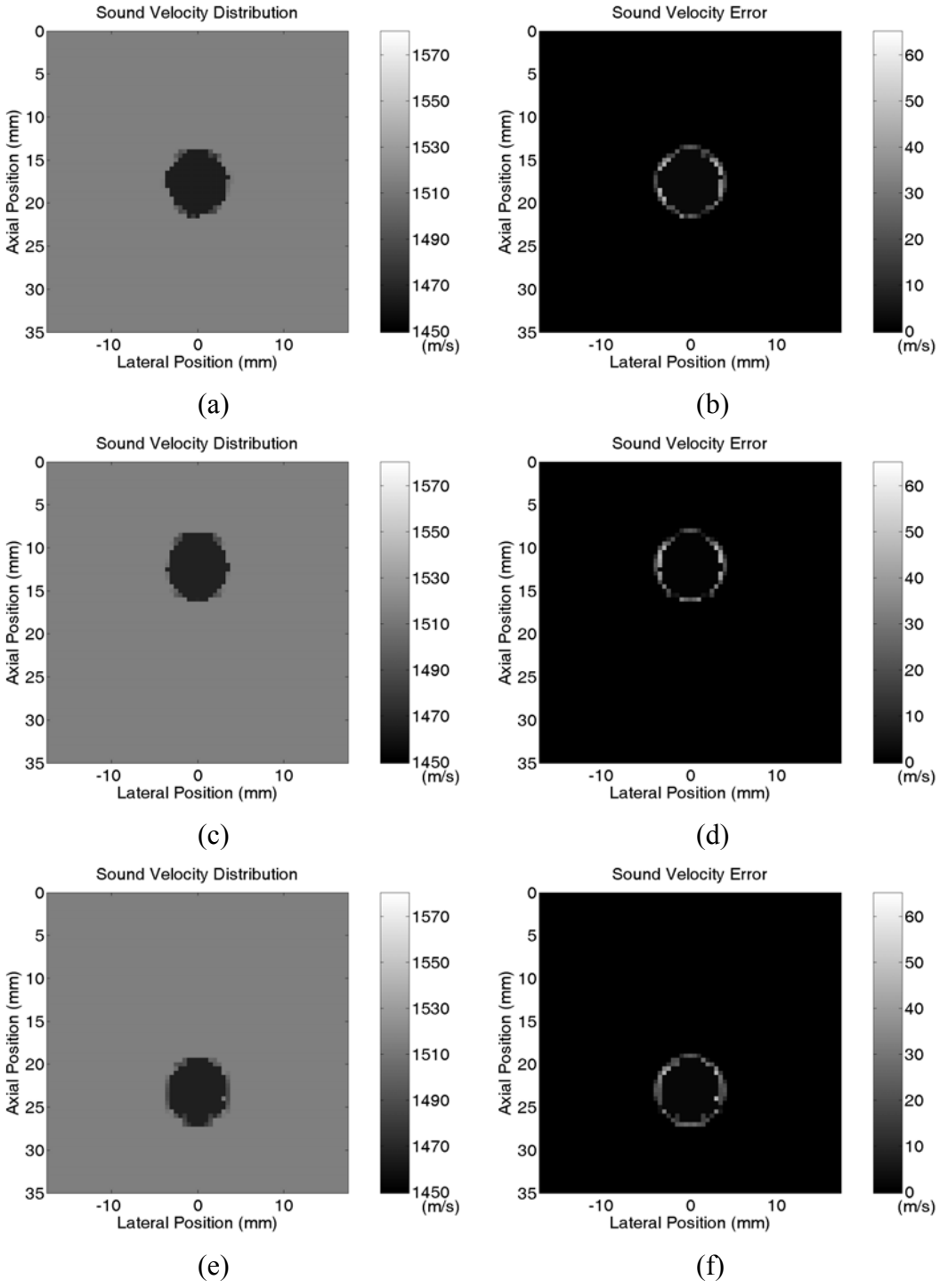

Fig. 3.8. Reconstructed sound velocity distributions and reconstruction errors. (a) and (b) Case i (the cylinder is at the center). (c) and (d) Case vii (the cylinder is at an upper position). (e) and (f) Case viii (the cylinder is at a lower position). In all cases cylinder radius = 4 mm, $c_{\mathrm{c,true}} = 1468.3\,\mathrm{m/s}$, and $c_{\mathrm{b,true}} = 1515.0\,\mathrm{m/s}$. The simulation parameters are also listed in Table 3.2.

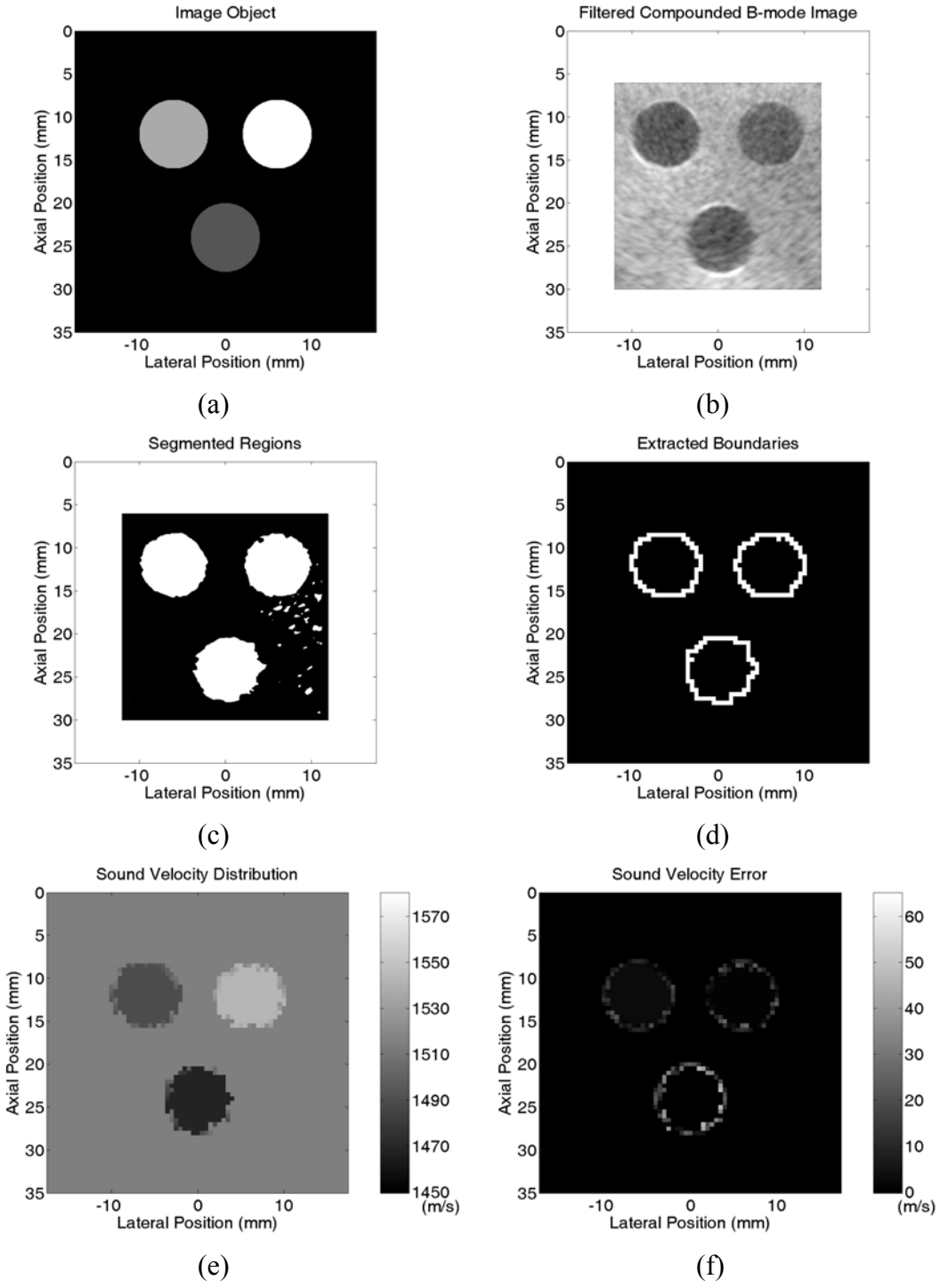

Fig. 3.9. (a) Image object comprising a background of glandular material ($c_{\mathrm{b},\infty} = 1521\,\mathrm{m/s}$, $\rho_{\mathrm{b}} = 1.05\,\mathrm{g/cm^3}$, and $\beta_{\mathrm{b}} = 5.68\,\mathrm{dB/cm}$ at 5 MHz) with three cylinders of the same radius of 4 mm ($c_{\mathrm{c},1,\infty} = 1496\,\mathrm{m/s}$, $\rho_{\mathrm{c},1} = 0.94\,\mathrm{g/cm^3}$ and $\beta_{\mathrm{c},1} = 2.68\,\mathrm{dB/cm}$ at 5 MHz in the upper-left cylinder, $c_{\mathrm{c},2,\infty} = 1549\,\mathrm{m/s}$, $\rho_{\mathrm{c},2} = 1.12\,\mathrm{g/cm^3}$ and $\beta_{\mathrm{c},2} = 7.39\,\mathrm{dB/cm}$ at 5 MHz in the upper-right cylinder, and $c_{\mathrm{c},3,\infty} = 1471\,\mathrm{m/s}$, $\rho_{\mathrm{c},3} = 0.94\,\mathrm{g/cm^3}$ and $\beta_{\mathrm{c},3} = 2.68\,\mathrm{dB/cm}$ at 5 MHz in the lower cylinder.). (b) B-mode image displayed with a 30-dB dynamic range. (c) Segmented regions. (d) Boundaries between the three cylinders and the background. (e) Reconstructed sound velocity distribution. (f) Sound velocity reconstruction error.

All the above cases considered only a single target in the object. A more complicated object comprising a background of glandular material with three cylinders, all with a radius of 4 mm, was also used to test Algorithm II. The geometry of the object is shown in Fig. 3.9(a). The first cylinder, located in the upper-left corner, was assigned the physical parameters of fat except for the sound velocity, which was set to $c_{\mathrm{c},1,\infty} = 1496\,\mathrm{m/s}$, where the subscripts c and 1 denote the first cylinder, and the subscript ∞ indicates an infinitely high frequency. The second cylinder, located in the upper-right corner, was assigned the parameters of a tumor, and the third cylinder, located in the lower region, was assigned those of fat. All parameters are listed in Table 3.1. The random perturbations added to the densities of the first, second, and third cylinder and the background were 0.5%, 0.5%, 0.89%, and 2.5% (root-mean-squared amplitude), respectively. The B-mode image is shown in Fig. 3.9(b). Fig. 3.9(c) shows the segmentation result after a $-14\,\mathrm{dB}$ (with respect to the maximal intensity) threshold is applied. In this case, several smaller regions randomly distributed in the background were also present. For each pixel of a size of $\Delta x_{\mathrm{s}} \cdot \Delta y_{\mathrm{s}}$, if the above-threshold area is lower than $0.96 \cdot \Delta x_{\mathrm{s}} \cdot \Delta y_{\mathrm{s}}$, then this pixel will be regarded as being outside the ROI. That is, an area ratio threshold of 0.96 was applied to the segmentation results shown in Fig. 3.9(c) before morphological dilation was applied. Therefore, these small regions were automatically removed during boundary extraction due to their smaller size; the boundaries are shown in Fig. 3.9(d). Note that removal of the smaller regions depends on the sampling intervals (Δx_{s} and Δy_{s}), and additional image processing techniques may be applied to improve boundary detection. The reconstructed sound velocity distribution is shown in Fig. 3.9(e) and the reconstruction error is shown in Fig. 3.9(f). In this case, $\Delta c_{\mathrm{b}} = 0.3\,\mathrm{m/s}$, $\Delta c_{\mathrm{c},1} = -3.2\,\mathrm{m/s}$, $\Delta c_{\mathrm{c},2} = 1.2\,\mathrm{m/s}$, and $\Delta c_{\mathrm{c},3} = 0.4\,\mathrm{m/s}$.

3.5 Discussion

3.5.1 Accuracy of sound velocity reconstruction

The derivation of (2.5) assumed straight-line propagation, whereas the time-of-flight data were generated with the effects of refraction. Nonetheless, sound velocity reconstruction generally still was accurate due to the use of hard constraints derived from the B-mode image. Besides, the time-of-flight was only used to derive soft constraints that were allowed to be violated, which reduced the impact of

refraction.

Note that the segmentation method employed in this chapter produced a detected area smaller than the original area. The accuracy of boundary extraction also affects the reconstruction results. All of the eight cases described in Section 3.4 were repeated using the true boundaries instead of boundaries derived from the segmented B-mode images. The results are denoted as $\Delta c_{\mathrm{c}}^{*}$ and $\Delta c_{\mathrm{b}}^{*}$, and are also listed in Table 3.2. In general, the reduction in the detected area has a bigger impact on smaller targets since the relative error of detected area (error of area over true area) is larger for smaller targets and a larger relative error of detected area will result in a larger sound velocity estimation error. Fig. 4.9 in Section 4.5 supports this point.

Large reconstruction errors occurred at the boundary, which is primarily due to refraction effects being much more significant there. Thus, either a significant portion of the time-of-flight data is discarded [as shown in Fig. 3.3(c)], or the remaining time-of-flight data have larger errors. Nonetheless, note that the "true" sound velocity at the boundary is not very meaningful because a sharp discontinuity in sound velocity is not expected in soft tissue.

3.5.2 Effect of pitch on sound velocity reconstruction

In the above simulations, only every third channel was used to obtain the time-of-flight data in order to save computation time. The effect of the number of channels on the accuracy of the reconstructed sound velocity was assessed, and the results are summarized in Table 3.3. The spatial sampling interval of the sound velocity distribution in the x and y directions were both 0.5 mm in all cases. The results show that the reconstruction accuracy does not necessarily improve when more channels are used. In fact, good accuracy was achieved even when using only 12 channels with an effective pitch of 3 mm, which is much larger than the spatial sampling interval of the sound velocity distribution.

The reason for the relative insensitivity of the accuracy to the pitch is that the time-of-flight constraints were only soft constraints and that there may be inconsistencies among them. Although more soft constraints may make the solution more reliable, the degree of inconsistency will not necessarily decrease as the number of soft constraints increases. Therefore, more time-of-flight data do not necessarily lead to a more accurate solution. However, these observations may be attributable to the objects under consideration having a simple geometry, and hence more studies are needed to better understand the performance of the algorithm with complex structures

and the application of time-of-flight constraints.

In Section 3.3, a pitch of $p_A = 0.45$ mm was used in the simulations for testing Algorithm I in order to reduce the computation time for the $4\times$ case. The reconstruction results shown in Table 3.3 support the conclusion that Algorithm II outperforms Algorithm I.

Table 3.3. Relation between reconstruction accuracy and effective pitch.

Effective pitch over 0.15 mm	Total number of channels	Δc in cylinder (m/s)	Δc in glandular material (m/s)
1	234	–2.6	0.0
2	117	–2.6	0.0
3	78	–2.6	0.0
4	59	–2.6	0.0
5	47	–2.7	0.0
6	39	–2.8	0.0
7	34	–2.2	0.0
8	30	–2.6	0.0
10	24	–3.7	0.0
12	20	–2.5	0.0
15	16	–3.7	0.1
20	12	–0.2	0.0

The n value in the first column means that only every nth channel in the array was used; the effective pitch was $n\times 0.15$ mm. Case i in Table 3.2 was evaluated. The spatial sampling intervals of sound velocity distribution in the x and y directions were both 0.5 mm.

3.5.3 Miscellaneous issues

Accurate reconstruction of the sound velocity distribution would allow it to be used to correct for waveform distortion resulting from sound velocity inhomogeneities and therefore enhancement of the B-mode image quality. The results shown in this chapter serve as a promising first step towards achieving this long-term research objective. Section 6.1 discusses the efficacy of applying the sound velocity distribution to correcting for the waveform distortions caused by sound velocity inhomogeneities. Note that in addition to the sound velocity distribution being used to correct for the waveform distortion, it can also be used as an independent image to complement the B-mode image.

To acquire the time-of-flight data, only one channel transmits at each firing. In

the simulations, no noise is added. In practice, however, the SNR may be insufficient due to attenuation and thus affecting the accuracy of time-of-flight estimation. To address this problem, coded excitation techniques [43] can be employed to increase the transmitted power while maintaining good temporal resolution. Note that an SNR enhancement of more than 20 dB is achievable because the code length is only limited by the distance between the metal plate and the array when only one channel is fired. Section 6.2 discusses the efficacy of applying coded excitation to collecting the time-of-flight data.

Although circular objects were used throughout this chapter, there is no fundamental restriction on the shape of ROI detectable by the proposed technique. The circular shape was chosen only for computation simplicity.

3.6 Concluding remarks

Here we have evaluated a method for incorporating the segmentation information of a B-mode image into the process of sound velocity reconstruction with limited-angle transmission tomography by simulations. A *k*-space method was used to simulate the B-mode images, and the series solution to the scattering of a plane wave incident on a fluid cylinder was used to generate the required time-of-flight data. Effects of wave propagation such as refraction and diffraction were included in the generated data. Simulation results based on a 5-MHz linear array show that the sound velocity error was generally 1–3 m/s, with a maximum of 5.8 m/s. The radius of the object under investigation was 2–6 mm, and the reconstructed sound velocities are accurate except at the boundaries. Thus, obtaining the sound velocity distribution is feasible with current B-mode imaging setup using linear arrays in simulations. Experiments were conducted in order to further evaluate the proposed technique in Chapter 4.

Chapter 4 Experimental results—sound velocity

In this chapter, a custom-made phantom containing a variety of image objects with differing physical properties was used to experimentally investigate the performance of the approach proposed in Chapter 2 and evaluated by simulations in Chapter 3.

4.1 Experimental setup and methods

A schematic of the experimental setup is shown in Fig. 4.1. The linear array (L6/128, STI, State College, PA) has $N_A = 128$ channels, an element pitch p_A of 0.3 mm, an elevation width of 5 mm, and an elevation focus of 25 mm. The array channels have a center frequency of 5.57 MHz and a –6 dB bandwidth of 4.10 MHz. A programmable digital array system (DiPhAS, Fraunhofer IBMT, Ingbert, Germany) [44] capable of transmitting a short pulse from any selected channel is used to acquire the channel data. All channel data were transferred from the array system to the computer for storage and further processing via a digital I/O (input/output) card (PCI-7300A, ADLINK, Taiwan County, Taiwan) on the computer. When channel i transmits, all channels except for channel j with $|j-i| = 64$ can receive (channel i and channel j with $|j-i| = 64$ share the same multiplexer and thus cannot be turned on simultaneously). That is, a channel data set $\{e_{ij}(t)\}, 1 \le i, j \le N_A, |j-i| \ne 64,$ can be collected by the array system. The transmitted pulse is a one-cycle square wave with a duration of $0.2\,\mu s$, and all $e_{ij}(t)$ were sampled at 40 MHz with a vertical resolution of 12 bits. For each transmit/receive combination, data corresponding to 16 consecutive firings were averaged off-line to enhance the SNR. The cross sections of the custom-made phantom (Dr. Ernest Madsen, Department of Medical Physics, University of Wisconsin-Madison, WI) are shown in Fig. 4.2(a) and (b) (top and side views, respectively). The corresponding parameters of the different materials

(mimicking different tissues in the breast), which were supplied by Dr. Madsen, are listed in Table 4.1. The nine cases listed in Table 4.2 were generated by moving the array along the *x*-axis.

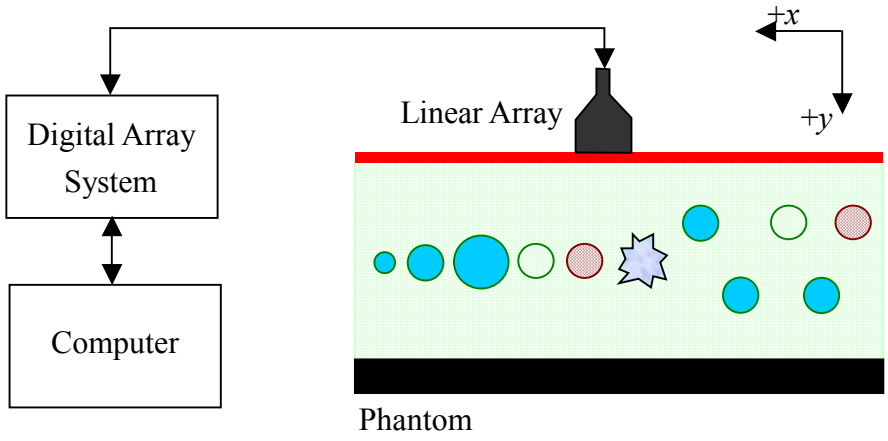

Fig. 4.1. Schematic of the data-acquisition setup.

Table 4.1. Parameters of the materials used in the phantom.

Material	Sound velocity c at 5 MHz and 22 ℃ (m/s)	Density ρ (g/cm^3)	Attenuation coefficient α at 5 MHz (dB/cm)	B-mode contrast relative to glandular tissue (dB)
Glandular tissue	1522	1.03	2.74	—
Fat	1464	0.94	2.21	–14
Cyst	1570	1.02	0.78	<–14
High-attenuation tumor	1547	1.10	7.36	–12
Irregular tumor	1553	1.07	4.26	–10

Note that the materials are mimicked.

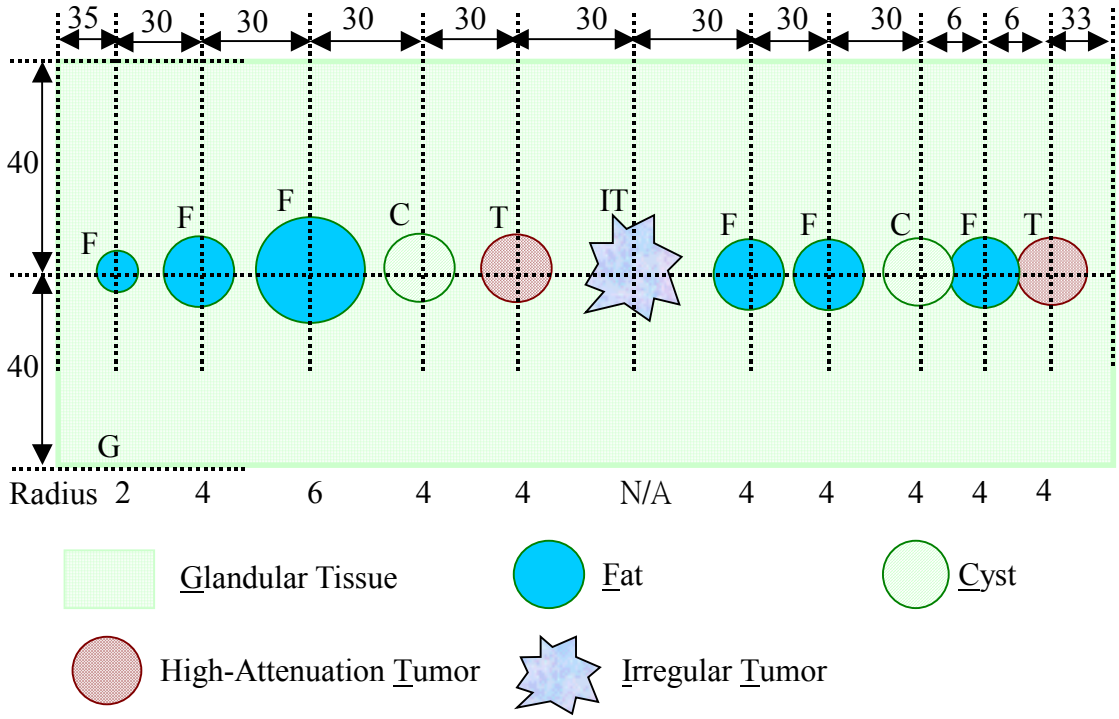

(a)

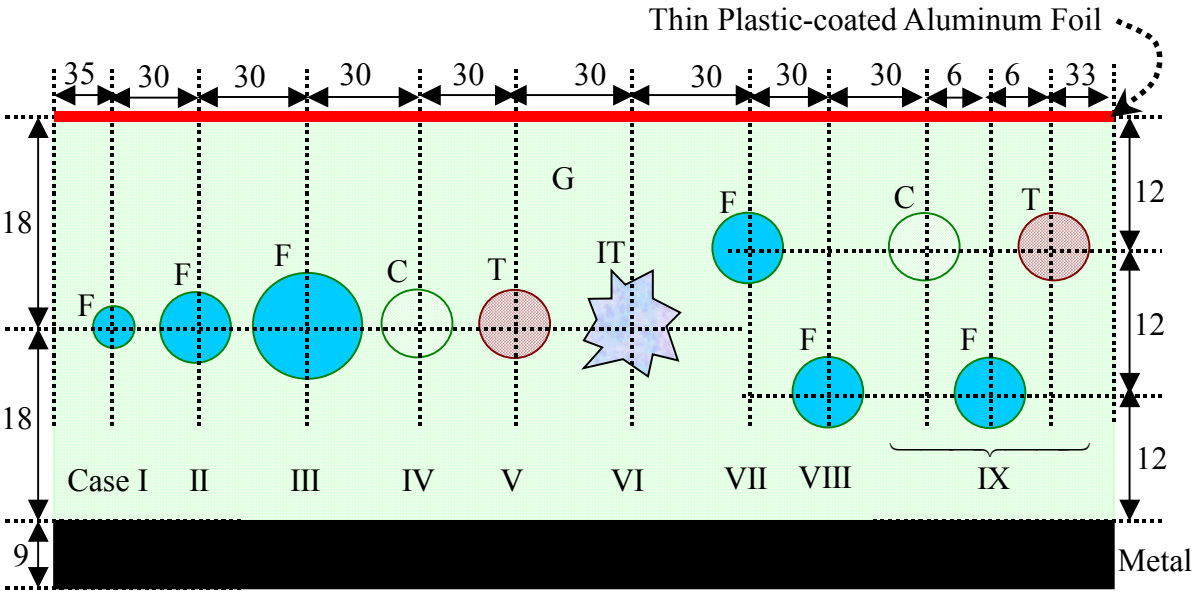

(b)

Fig. 4.2. Cross sections of the phantom used in experiments. (a) Top view. (b) Side view. All the dimensions are in millimeters.

Table 4.2. Objects included in different cases and the estimation results in experiments.

Case	ROI	Sphere radius (mm)	ROI position	Δc_{ROI} (m/s)	Δc_{G} (m/s)
I	Fat	2	Center	2.6	0.3
II	Fat	4	Center	4.5	0.3
III	Fat	6	Center	4.3	0.2
IV	Cyst	4	Center	3.9	0.3
V	High-attenuation tumor	4	Center	10.5	–0.2
VI	Irregular tumor	N/A	Center	11.5	0.9
VII	Fat	4	6 mm above the center	4.9	0.6
VIII	Fat	4	6 mm below the center	2.5	0.0
IX-1	Cyst	4	Upper-left corner	0.6	0.6
IX-2	High-attenuation tumor	4	Upper-right corner	9.5	
IX-3	Fat	4	6 mm below the center	0.9	

The material in the background was glandular tissue in all cases.

4.2 Extraction of time-of-flight data

To extract Δt_{ij} (the time of flight after geometrical delay compensation), the peak value e_{p} of the envelope of $e_{ij}(t)$ around $t_{ij,0}$ (with a time window of $10\,\mu\mathrm{s}$) was found, and then t_{ij} (the time of flight) was set to be the time when the envelope crossed $\frac{1}{2}e_{\mathrm{p}}$ at the rising edge of the peak. The following two rules were applied to remove the t_{ij} associated with severely distorted $e_{ij}(t)$ around $t_{ij,0}$. First, t_{ij} and Δt_{ij} were ignored if

$$E_{ij} < 0.15 \frac{1}{N_{\mathrm{A}}} \sum_{q=1}^{N_{\mathrm{A}}} E_{iq}\,, \tag{4.1}$$

where E_{ij} denotes the energy of the envelope of $e_{ij}(t)$ around $t_{ij,0}$ with element

factor compensation. Element factors for all transmit/receive combinations were estimated using a channel data set collected with only water between the array and the metal plate. After the first step, Δt_{u} and Δt_{l} were found, where Δt_{u} (Δt_{l}) is a time value such that 95% of the Δt_{ij} is smaller (larger) than it and the other is larger (smaller) than it. Second, t_{ij} was dropped if

$$\left|\Delta t_{ij} - \frac{\Delta t_{\mathrm{u}} + \Delta t_{\mathrm{l}}}{2}\right| > 2\left(\Delta t_{\mathrm{u}} - \Delta t_{\mathrm{l}}\right). \tag{4.2}$$

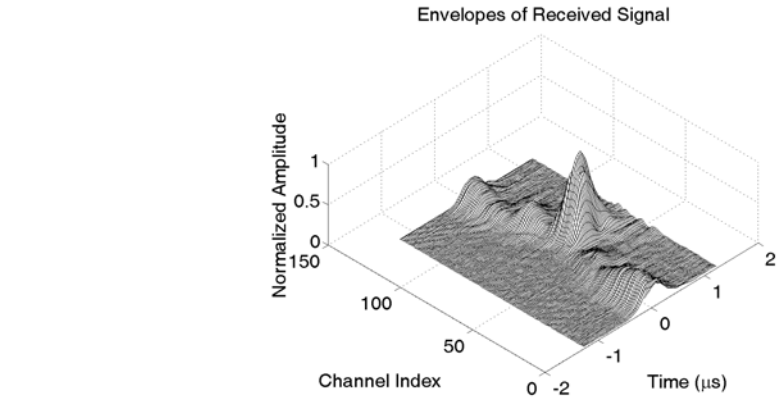

(a)

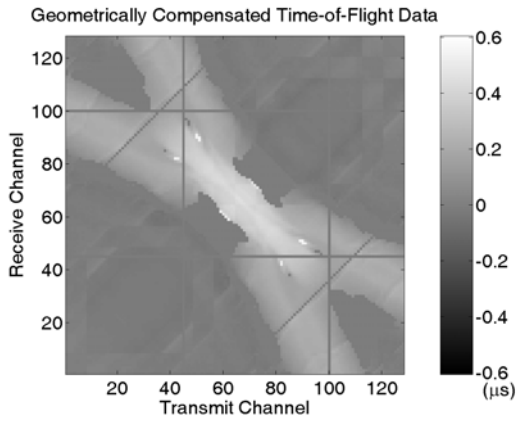

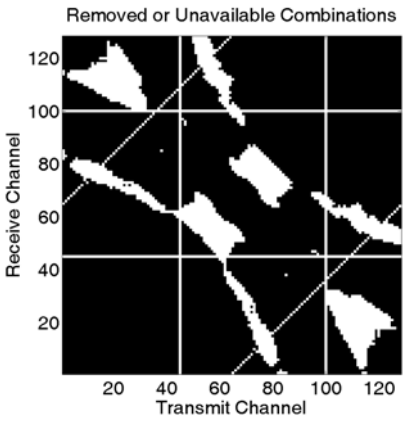

(b) (c)

Fig. 4.3. (a) Envelopes of the received signals when the 64th channel transmits in Case VIII. Geometrical delays and element factors have been compensated. (b) The geometrically compensated time-of-flight data. Note that all the removed and unavailable Δt_{ij} data values are replaced by 0. (c) A white pixel at position (i, j) means that the associated Δt_{ij} value was removed or unavailable.

Fig. 4.3(a) shows all the receive envelope data around $\Delta t_{ij,0}$ when the 64th channel was used on transmit in Case VIII with the element factor compensated. The

geometrically compensated time-of-flight data in Case VIII are shown in Fig. 4.3(b). Note that all the removed and unavailable Δt_{ij} data values are replaced by 0. The removed and unavailable transmit/receive combinations are shown in Fig. 4.3(c) in white, where the two vertical lines and the two horizontal lines were due to two dead elements of the array. The two lines at 45° were due to the multiplexer setup.

4.3 Generation of C_{image}

Spatial compounding [41] (with 5 subapertures all having 43 channels and centered at channels 22, 43, 65, 86, and 107) was performed to generate B-mode images with reduced speckle intensity variations. The pixel size was 0.038 mm (x-axis) by 0.037 mm (y-axis). Dynamic focusing was performed and dynamic aperture size was used with the lower limit of the F-number being 1 on both transmit and receive when forming a subimage. The steering angle of all subapertures was limited to within $\pm 45^{\circ}$. At each pixel, the signals of all contributing subapertures were averaged. In Case I, the speckle SNR, defined as the mean pixel intensity over the standard deviation of the pixel intensity, in the ROI was raised from 0.90 to 1.86 by spatial compounding. To further reduce the speckle variations, the compound B-mode image was low-pass filtered using a two-dimensional Gaussian filter with a $1/e$ cutoff at 0.152 mm to generate the final B-mode image. Once the filtered B-mode image was obtained, a single threshold was applied for segmentation and the regions in the thresholded binary image with an area smaller than π mm^2 were removed.

For most cases (Cases I–IV, VII, and VIII) the ROIs could be extracted successfully by the above procedures, but morphological dilation and erosion [42] (which were necessary for Cases V, VI, and IX) were applied to all cases after thresholding in order to remove the holes in ROI candidates and make the boundaries more regular. The morphological structuring element was disk shaped with a radius of 40 pixels for both dilation and erosion. The sampling intervals Δx_{s} and Δy_{s} of the sound velocity distribution in the x and y directions were 0.55 mm and 0.53 mm, respectively, which were different from those of the B-mode image. Therefore, after finding the ROIs, the resultant binary images were resampled by applying an area ratio threshold of 0.96. For each pixel of size $\Delta x_{\text{s}} \cdot \Delta y_{\text{s}}$ in the resampled binary image, if the above-threshold area was lower than $0.96 \cdot \Delta x_{\text{s}} \cdot \Delta y_{\text{s}}$, then this pixel was regarded as being outside the ROI. The boundaries were derived from the resampled ROIs by morphological dilation (according to the disparity between the ROIs and

their dilated versions), and with these boundaries C_{image} was generated using (2.16).

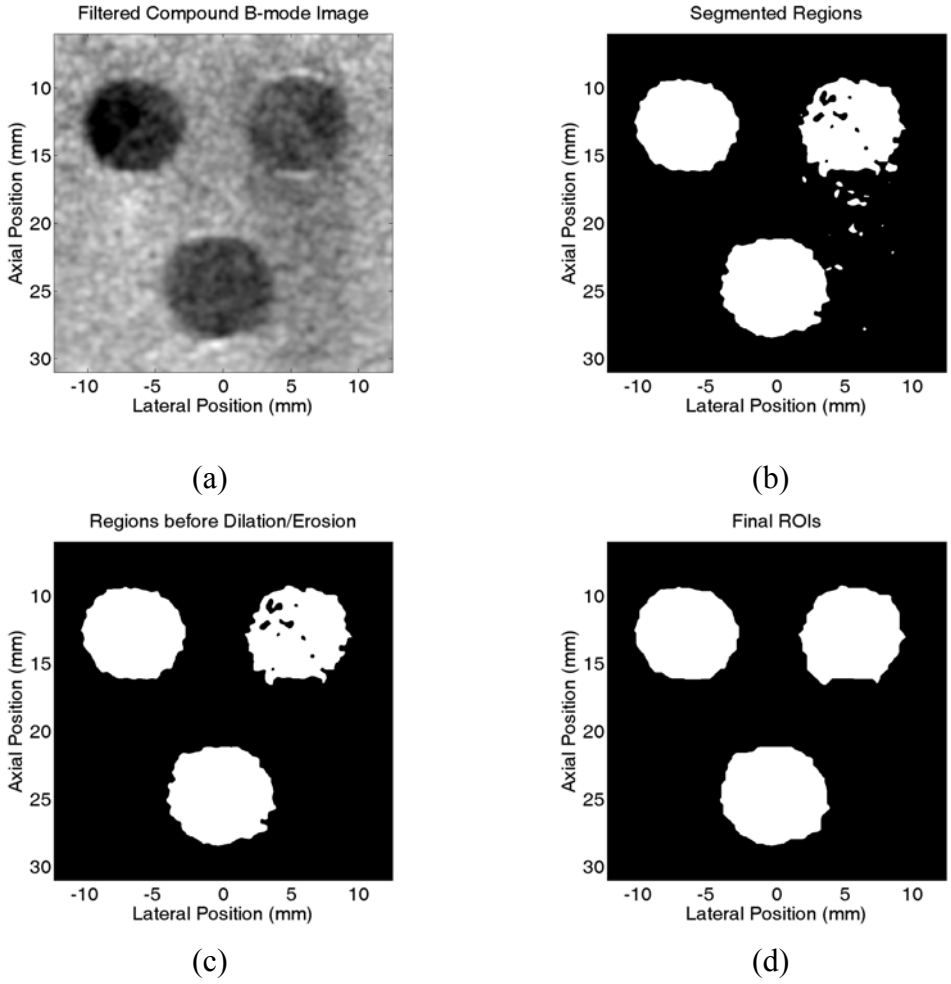

Fig. 4.4. Evaluation of Case IX. The image object comprises a background of glandular material ($c_{\text{G}} = 1522\,\text{m/s}$, $\rho_{\text{G}} = 1.03\,\text{g/cm}^3$, and $\alpha_{\text{G}} = 2.74\,\text{dB/cm}$) with three spheres, all with a radius of 4 mm ($c_{\text{C}} = 1570\,\text{m/s}$, $\rho_{\text{C}} = 1.02\,\text{g/cm}^3$ and $\alpha_{\text{C}} = 0.78\,\text{dB/cm}$ in the upper-left cyst sphere; $c_{\text{T}} = 1547\,\text{m/s}$, $\rho_{\text{T}} = 1.10\,\text{g/cm}^3$ and $\alpha_{\text{T}} = 7.36\,\text{dB/cm}$ in the upper-right high-attenuation tumor sphere; and $c_{\text{F}} = 1464\,\text{m/s}$, $\rho_{\text{F}} = 0.94\,\text{g/cm}^3$, and $\alpha_{\text{F}} = 2.21\,\text{dB/cm}$ in the lower fat sphere). (a) Filtered compound B-mode image displayed with a 30-dB dynamic range. (b) Segmented regions. (c) Binary image after removing smaller regions. (d) ROIs extracted by dilation and erosion based on the binary image in (c). (e) Boundaries between the three spheres and the background. (f) Reconstructed sound velocity distribution.

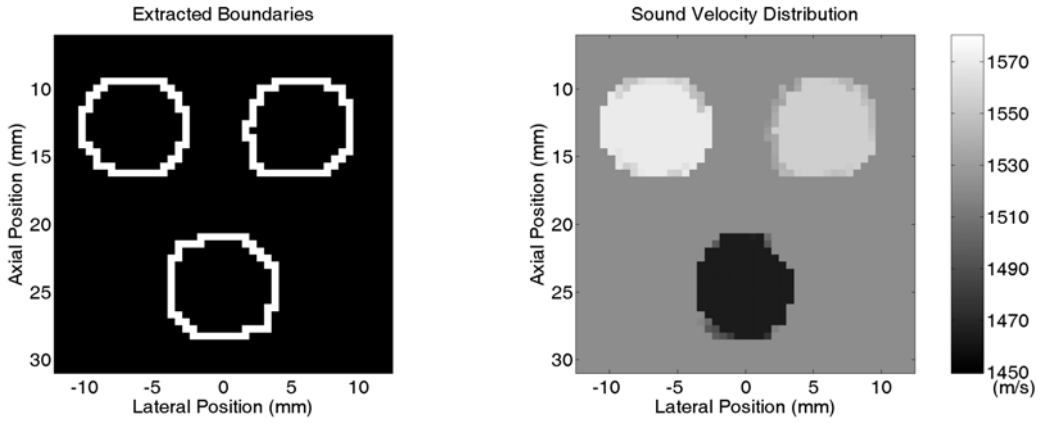

(e) (f)

Fig. 4.4. (Continued).

Fig. 4.4(a)–(e) show the results corresponding to different steps using Case IX as an example. The filtered compound B-mode image is displayed in Fig. 4.4(a) with a 30-dB dynamic range. Fig. 4.4(b) shows the segmentation result after a –16 dB threshold (with respect to the maximum intensity) was applied. The binary image after removing regions smaller than π mm^2 is shown in Fig. 4.4(c). Morphologically dilating the ROI candidates and then eroding the resultant binary image extracted the ROIs [see Fig. 4.4(d)]. Fig. 4.4(e) shows the extracted boundaries.

4.4 Reconstructed sound velocity images

The sound velocity images were reconstructed using Algorithm II introduced in Section 2.3, using $c_{\text{lower}} = 1450$ m/s and $c_{\text{upper}} = 1580$ m/s. All the reconstruction results are listed in Table 4.2. The reconstructed sound velocity distribution for Case IX is shown in Fig. 4.4(f) over the range 1450 m/s to 1580 m/s. Define errors as

$$\Delta c_{(\cdot)} = c_{(\cdot),\text{recon}} - c_{(\cdot),\text{true}}, \tag{4.3}$$

where $(\cdot)$ denotes F (fat), C (cyst), T (high-attenuation tumor), IT (irregular tumor), G (glandular tissue), or ROI, $c_{(\cdot),\text{true}}$ is the true sound velocity listed in Table 4.1, and $c_{(\cdot),\text{recon}}$ is the reconstructed sound velocity. In Case IX, $\Delta c_{\text{C}} = 0.6$ m/s, $\Delta c_{\text{T}} = 9.5$ m/s, $\Delta c_{\text{F}} = 0.9$ m/s, and $\Delta c_{\text{G}} = 0.6$ m/s.

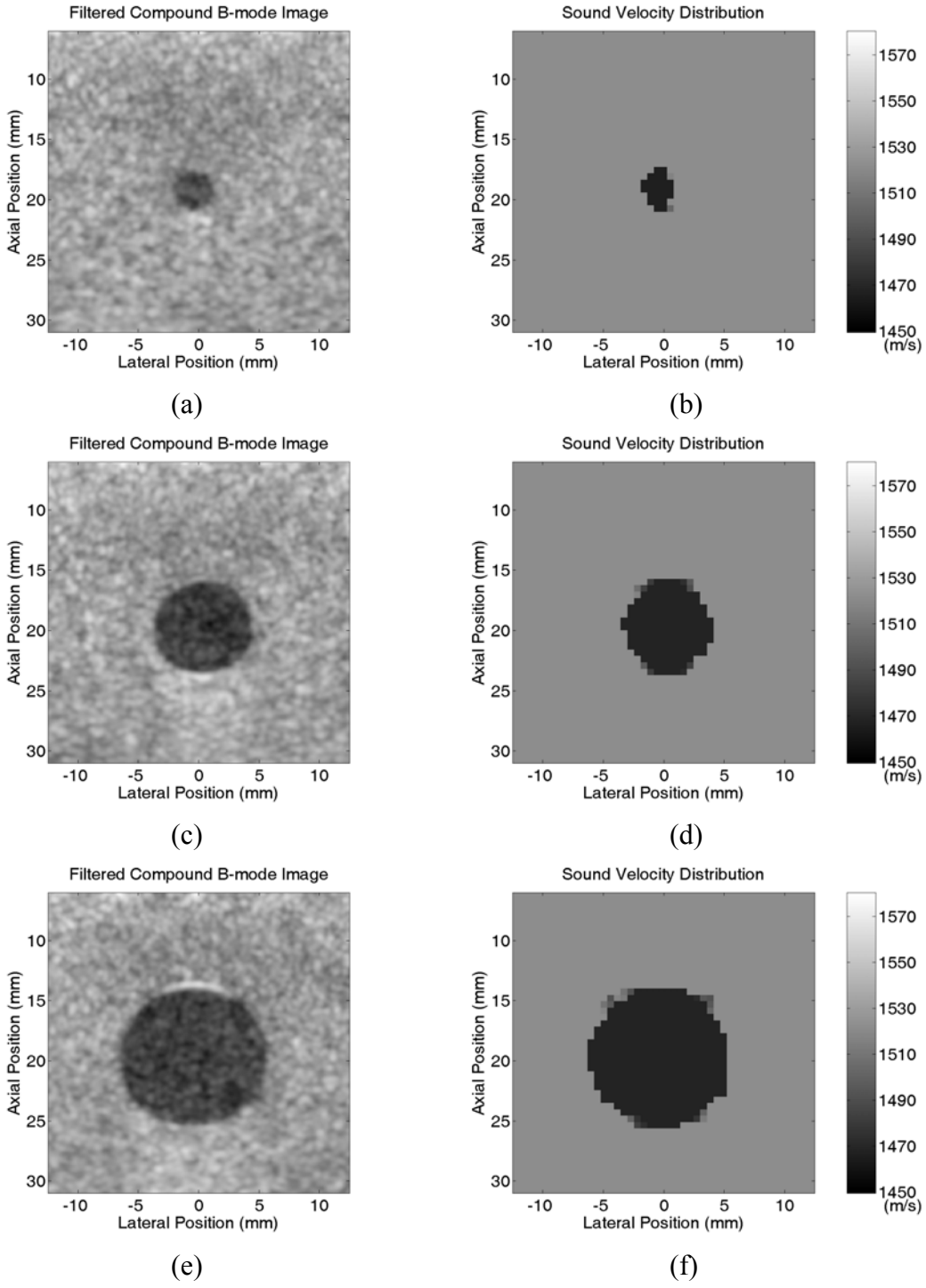

Fig. 4.5. Filtered compound B-mode images (displayed with a 30-dB dynamic range) and reconstructed sound velocity distributions of objects containing fat spheres ($c_{\mathrm{F}} = 1464\,\mathrm{m/s}$, $\rho_{\mathrm{F}} = 0.94\,\mathrm{g/cm^3}$, and $\alpha_{\mathrm{F}} = 2.21\,\mathrm{dB/cm}$) with different radii. (a) and (b): Case I (radius = 2 mm). (c) and (d): Case II (radius = 4 mm). (e) and (f): Case III (radius = 6 mm).

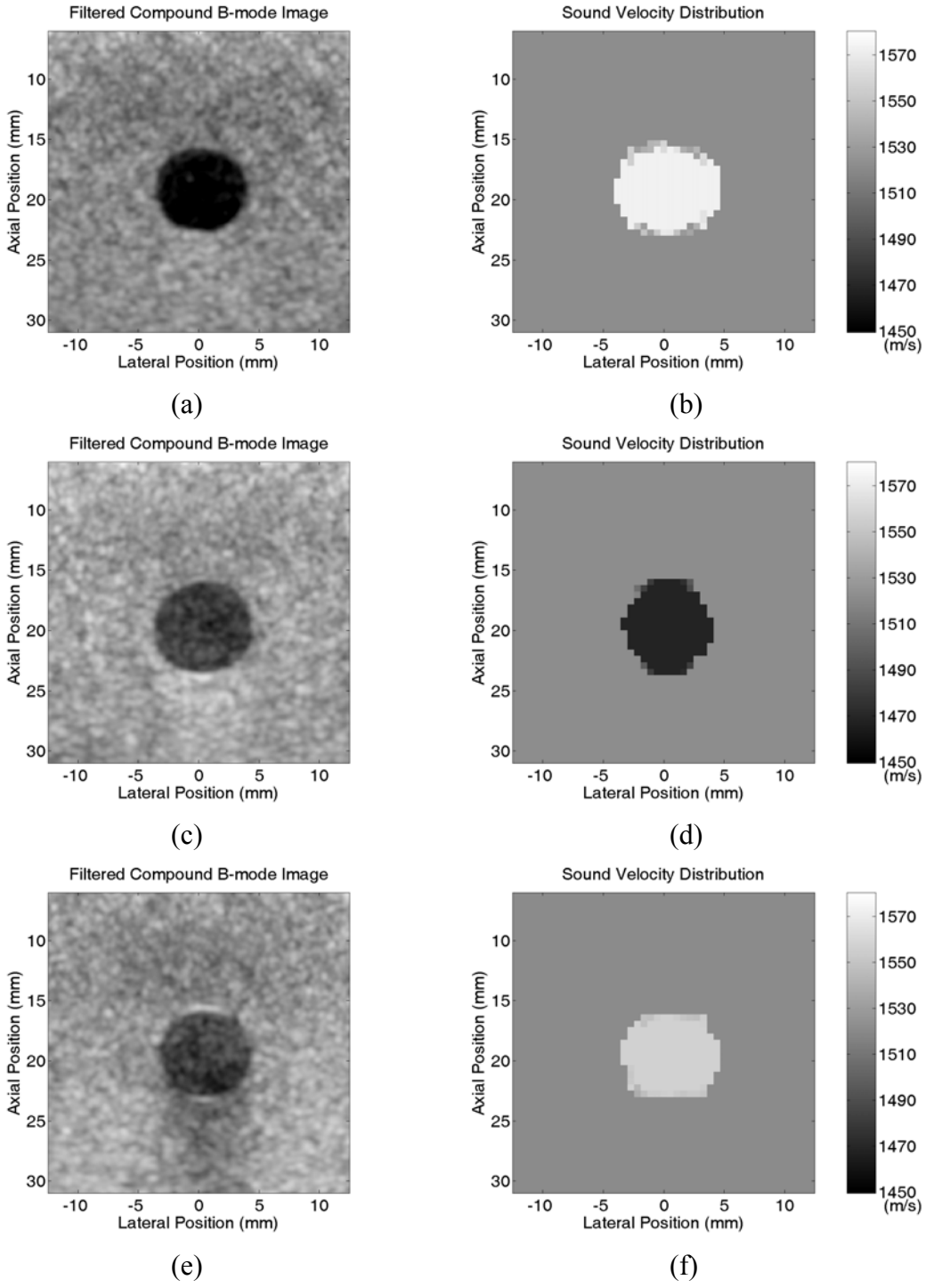

Fig. 4.6. Filtered compound B-mode images (displayed with a 30-dB dynamic range) and reconstructed sound velocity distributions of objects containing spheres all with a radius of 4 mm but representing different tissue types. (a) and (b): Case IV (cyst; $c_{\mathrm{C}} = 1570\,\mathrm{m/s}$, $\rho_{\mathrm{C}} = 1.02\,\mathrm{g/cm^3}$, and $\alpha_{\mathrm{C}} = 0.78\,\mathrm{dB/cm}$). (c) and (d): Case II (fat; $c_{\mathrm{F}} = 1464\,\mathrm{m/s}$, $\rho_{\mathrm{F}} = 0.94\,\mathrm{g/cm^3}$, and $\alpha_{\mathrm{F}} = 2.21\,\mathrm{dB/cm}$). (e) and (f): Case V (tumor; $c_{\mathrm{T}} = 1547\,\mathrm{m/s}$, $\rho_{\mathrm{T}} = 1.10\,\mathrm{g/cm^3}$, and $\alpha_{\mathrm{T}} = 7.36\,\mathrm{dB/cm}$).

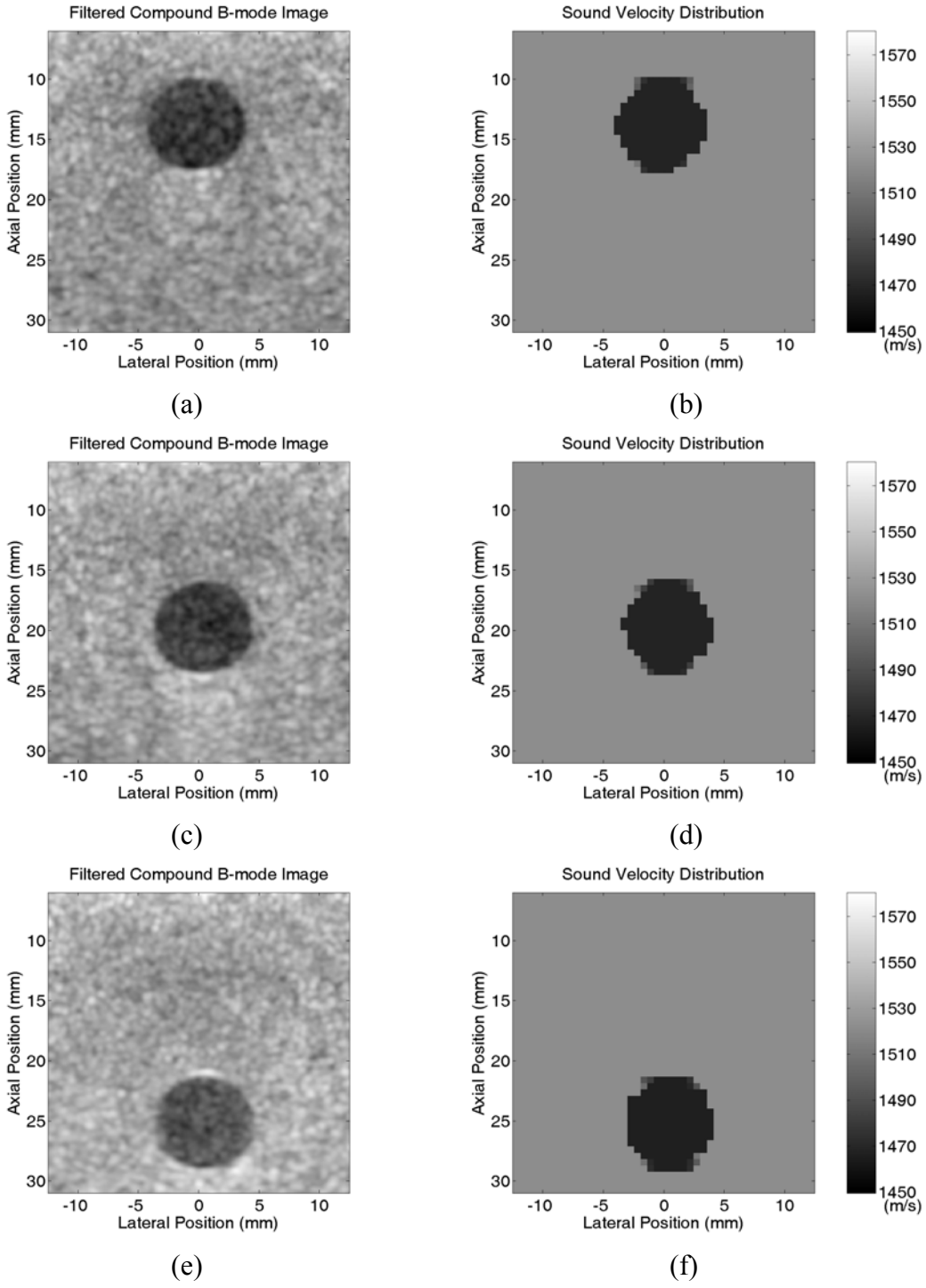

Fig. 4.7. Filtered compound B-mode images (displayed with a 30-dB dynamic range) and reconstructed sound velocity distributions of objects containing fat spheres ($c_{\mathrm{F}} = 1464\,\mathrm{m/s}$, $\rho_{\mathrm{F}} = 0.94\,\mathrm{g/cm^3}$, and $\alpha_{\mathrm{F}} = 2.21\,\mathrm{dB/cm}$) all with a radius of 4 mm but at different positions. (a) and (b): Case VII (the sphere is above the center). (c) and (d): Case II (the sphere is at the center). (e) and (f): Case VIII (the sphere is below the center).

The filtered compound B-mode images and reconstructed sound velocity images for Cases I–VIII are shown in Fig. 4.5–Fig. 4.8. Fig. 4.5–Fig. 4.7 demonstrate the

effects on the reconstruction accuracy of the size of the spherical objects, different sound velocities in the objects, and the depth of the objects, respectively. In all cases the errors in the background region are small. Fig. 4.5(a) and (b), Fig. 4.5(c) and (d), and Fig. 4.5(e) and (f) show the estimation results corresponding to fat spheres with a radius of 2 mm, 4 mm, and 6 mm, respectively. The left panels [Fig. 4.5(a), (c), and (e)] are the filtered compound B-mode images, and the right panels [Fig. 4.5(b), (d), and (f)] are the estimated sound velocity distributions. The Δc_{ROI} values are 2.6 m/s, 4.5 m/s, and 4.3 m/s, respectively, and those of Δc_{G} are 0.3 m/s, 0.3 m/s, and 0.2 m/s, respectively. Fig. 4.6(a) and (b), Fig. 4.6(c) and (d), and Fig. 4.6(e) and (f) show the filtered compound B-mode images and the sound velocity distributions corresponding to spheres consisting of different tissues (cyst, fat, and tumor, respectively). The Δc_{ROI} values are 3.9 m/s, 4.5 m/s, and 10.5 m/s, respectively, and those of Δc_{G} are 0.3 m/s, 0.3 m/s, and –0.2 m/s, respectively. Fig. 4.7(a) and (b), Fig. 4.7(c) and (d), and Fig. 4.7(e) and (f) show the filtered compound B-mode images and the sound velocity distributions corresponding to fat spheres at different positions (upper, center, and lower, respectively). The Δc_{ROI} values are 4.9 m/s, 4.5 m/s, and 2.5 m/s, respectively, and those of Δc_{G} are 0.6 m/s, 0.3 m/s, and 0.0 m/s, respectively. Finally, Fig. 4.8(a) and (b) show the filtered compound B-mode image and the sound velocity distribution for Case VI, respectively. In this case $\Delta c_{\mathrm{IT}} = 11.5\,\mathrm{m/s}$, $\Delta c_{\mathrm{G}} = 0.9\,\mathrm{m/s}$, and the original sound velocity difference between the irregular tumor and the glandular background is 31 m/s, as shown in Table 4.1. Fig. 4.8(b) exhibits large errors in boundary extraction that affect the accuracy of sound velocity estimation.

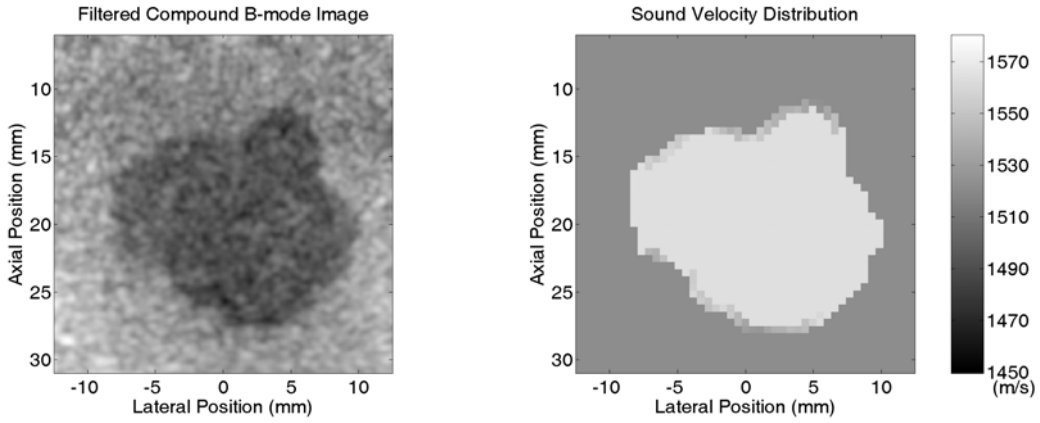

(a) (b)

Fig. 4.8. (a) Filtered compound B-mode image (displayed with a 30-dB dynamic range) and (b) reconstructed sound velocity distribution of an object containing an irregular tumor. $c_{\mathrm{IT}} = 1553\,\mathrm{m/s}$, $\rho_{\mathrm{IT}} = 1.07\,\mathrm{g/cm^3}$, and $\alpha_{\mathrm{T}} = 4.26\,\mathrm{dB/cm}$.

4.5 Discussion

To evaluate the sensitivity of the sound velocity error to the area of the segmented ROI, the ROIs in Case I and III were artificially changed and the corresponding sound velocity distributions were then estimated. Every new ROI was generated from the original ROI by adding pixels on the outer boundary or removing pixels on the inner boundary. Ten different ROIs were randomly generated given a total ROI area. Fig. 4.9(a) and (b) show the curves of mean sound velocity difference (between the new estimated sound velocity and the original one in the ROI) versus ROI area difference for Case I and III, respectively. The ROI area difference was normalized with respect to the nominal area (i.e., 4π mm^2 and 36π mm^2 for Case I and III, respectively). Also shown in Fig. 4.9 are the error bars specifying ± one standard deviation. Note that the standard deviation corresponding to the zero ROI area difference was zero since the ROI was fixed at this point and no randomly generated ROIs were generated. It was found that the sound velocity difference is less than ±3 m/s when the ROI area difference is within ±5% in these cases.

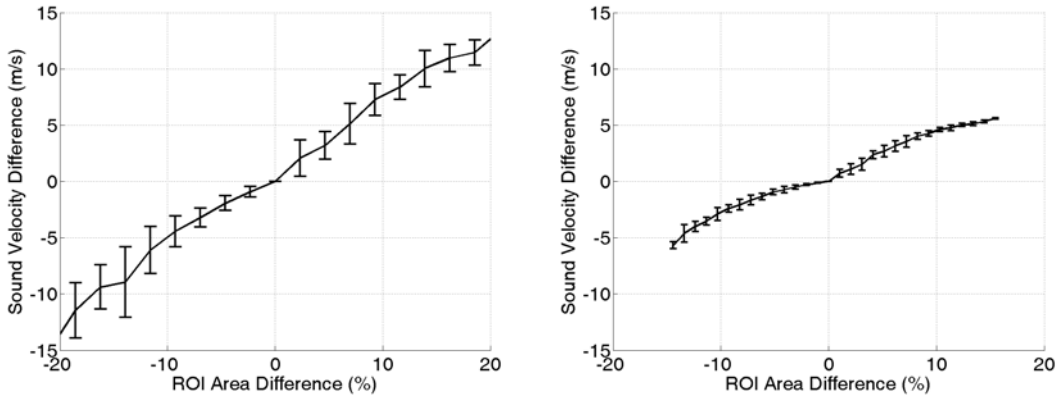

(a) (b)

Fig. 4.9. The curves of mean sound velocity difference (between the new estimated sound velocity and the original one in the ROI) versus ROI area difference in percentage for (a) Case I and (b) Case III. Ten different ROIs were randomly generated given an ROI area. The error bars specify ± one standard deviation. Note that the standard deviation corresponding to the zero ROI area difference was zero since the ROI was fixed at this point and no randomly generated ROIs were generated.

The imaging setup shown in Fig. 1.1 treats image objects as two-dimensional. Although the image objects in experiments were three-dimensional, generally good sound velocity estimation accuracy was achieved. The reconstruction errors are larger for the high-attenuation and irregular tumors. A new phantom is required in order to

experimentally investigate whether or not the higher attenuations result in larger errors. The large error in the boundary extraction for Case VI partially contributes to the sound velocity estimation error in that case.

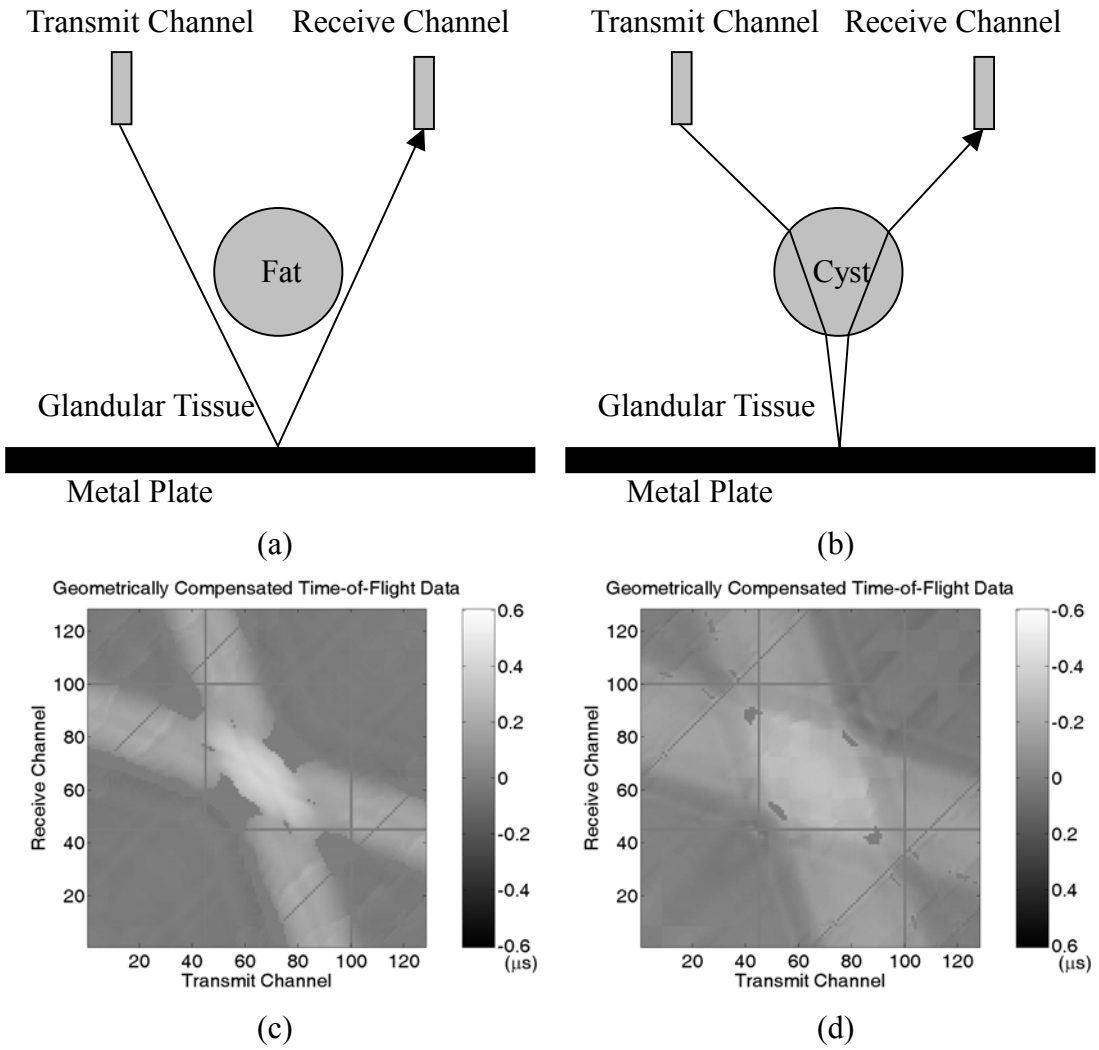

Fig. 4.10. The ray-tracing diagrams for (a) Case II and (b) Case IV, and the geometrically compensated time-of-flight data in (c) Case II and (d) Case IV. Note that the colormap in (d) for Case IV has been reversed for display purposes.

The sound velocity error in ROI tends to be positive in experiments (this phenomenon did not occur in simulations). One possible reason is the expansion (contraction) of the fat (cyst, high-attenuation tumor, or irregular tumor) region in the B-mode image with respect to its original size – a lower (higher) sound velocity is equivalent to a longer (shorter) distance. Because the area of the background is much larger than that of the ROI, the sound velocity estimation is more sensitive to the sound velocity error in the background than that in the ROI. Therefore, the reconstructed sound velocity in the background will only be slightly affected, and the

absolute value of the difference of the reconstructed sound velocities between the ROI and the background tends to decrease as the area of ROI increases. Another potential source of error is a refraction artifact. The ray-tracing diagrams shown in Fig. 4.10(a) and (b) for Cases II and IV, respectively, illustrate that the number of transmit/receive combinations with times of flight affected by the sphere is larger in Case IV than in Case II. This point is further demonstrated by Fig. 4.10(c) and (d), which show the geometrically compensated time-of-flight data for Cases II and IV, respectively (note that the colormap for Case IV has been reversed for display purposes). Thus, a higher sound velocity in the ROI will increase its effective area when measuring the time-of-flight data. Consequently, the area in B-mode image is effectively contracted during reconstruction.

In a few cases there were multiple reflections between the array and the top surface of the phantom, which made finding the peak of the echo from the metal plate difficult. This explains why we used the rising edge rather than the peak to estimate the time of flight.

The shadows of the high-attenuation and irregular tumors are clearly seen in B-mode images for Cases V, VI, and IX. These shadows complicated the extraction of ROIs. If only the tissue type is important, then sound velocity images are not necessary in these simple cases. However, if the image contains more complicated objects, B-mode image alone may be insufficient for identifying different tissue types. In this case, the sound velocity distribution can be used to complement conventional B-mode ultrasound and to enhance breast cancer detection in the situations where a fat region may be incorrectly diagnosed as a tumor, because the fat region typically has a sound velocity lower than the glandular tissue whereas a tumor typically has a higher sound velocity. Based on the result of Case I, a tumor with a diameter as small as 4 mm may be distinguishable using B-mode ultrasound with the help of the sound velocity information.

4.6 Concluding remarks

In this chapter, we experimentally investigated the technique proposed in Chapter 2, including Algorithm II in Section 2.3, for reconstructing the sound velocity distribution in the breast. The experimental setup, which consisted of a 128-channel array, a digital array system, a phantom, and a computer, allowed acoustic data acquisition for simultaneous B-mode image formation and limited-angle tomographic

sound velocity reconstruction. The reconstruction algorithm incorporates the segmentation information from the B-mode image of the same object. Nine cases were evaluated by scanning the phantom at different positions. Although the image objects were three-dimensional, good sound velocity estimation results were obtained using the one-dimensional array, with sound velocity errors being less than 5 m/s in eight of eleven ROIs. Although the errors associated with tumor objects were larger, successful tissue classification was still possible using the information that the sound velocity should be higher in the ROI than in the background for those cases. Therefore, this method makes obtaining the sound velocity distribution feasible with the current B-mode imaging setup using linear arrays.

Chapter 5 Experimental results—attenuation coefficient

5.1 Introduction

When a single-frequency acoustic plane wave propagates in a homogeneous soft tissue, its amplitude A can be assumed to exponentially decay with the propagation distance d_{p} [22], [45]. Specifically,

$$-20\log_{10}\left(\frac{A}{A_0}\right)=\alpha d_{\mathrm{p}}, \tag{5.1}$$

where A_0 is the original amplitude and α is the attenuation coefficient of the tissue. In general, the attenuation coefficient varies from tissue to tissue. For example, the attenuation coefficient of cancerous tissue is higher than that of cyst [19]–[21]. Therefore, the attenuation coefficient distribution in the breast can help detect cancer.

In this chapter, the attenuation coefficient distributions were reconstructed for the nine cases described in Chapter 4 using the convex programming formulation. Furthermore, in order to improve the estimation accuracy, a technique based on the angular spectrum method was developed to compensate the effects of refraction on the attenuation data.

5.2 Reconstruction method

In addition to B-mode image and sound velocity distribution, the setup shown in Fig. 1.1 can also be used to measure the attenuation coefficient distribution. Let $\{e_{ij}(t)\}, 1\le i,j\le N_{\mathrm{A}}$, be the complete channel data set with an object between the array and the metal plate, and $\{e_{\mathrm{w},ij}(t)\}$ be the complete channel data set with water

between. With $e_{ij}(t)$ [$e_{\mathrm{w},ij}(t)$], the echo $a_{ij}(t)$ [$a_{\mathrm{w},ij}(t)$] reflected from the bottom metal plate corresponding to the same transmit/receive combination can be obtained. Let $\alpha(x,y;f)$ [$\alpha_{\mathrm{w}}(x,y;f)=\alpha_{\mathrm{w}}(f)$] and $A_{ij}(f)$ [$A_{\mathrm{w},ij}(f)$] denote the attenuation coefficient distribution in the object (water) and the temporal spectrum of $a_{ij}(t)$ [$a_{\mathrm{w},ij}(t)$], respectively. Assume the straight-line propagation along the path L_{ij} and define

$$\Delta A_{ij}(f) = -20\log_{10}\left(\left|A_{ij}(f)\right|\right) - \left[-20\log_{10}\left(\left|A_{\mathrm{w},ij}(f)\right|\right)\right], \tag{5.2}$$

then

$$\Delta A_{ij}(f) = \int_{L_{ij}} \left[\alpha(x,y;f) - \alpha_{\mathrm{w}}(f)\right] dl \tag{5.3}$$

based on (5.1). Since the attenuation coefficient of water is negligible in general [22], (5.3) can be reduced to

$$\Delta A_{ij}(f) = \int_{L_{ij}} \alpha(x,y;f)\, dl\,. \tag{5.4}$$

(5.4) is analogous to (2.3). Thus, following the procedure described in Section 2.1, (5.4) becomes

$$\mathbf{L}\boldsymbol{\alpha} = \Delta\mathbf{a}\,, \tag{5.5}$$

where the attenuation coefficient distribution $\boldsymbol{\alpha} = \boldsymbol{\alpha}(f)$ is an $MN \times 1$ column vector consisting of the attenuation coefficients at the grid points, and the attenuation data $\Delta\mathbf{a} = \Delta\mathbf{a}(f)$ is an $\left[N_{\mathrm{A}}(N_{\mathrm{A}}+1)/2\right]\times 1$ column vector consisting of $\Delta A_{ij}(f)$.

The convex programming formulation introduced in Section 2.2 was used to solve (5.5) [32]. Two kinds of a priori knowledge of $\boldsymbol{\alpha}(f)$ are used. First, the attenuation coefficient is assumed to be in $[\alpha_{\mathrm{lower}}, \alpha_{\mathrm{upper}}]$ (where $\alpha_{\mathrm{lower}} = 0$ dB/cm, $\alpha_{\mathrm{upper}} = 2f$ dB/cm, and f is in the unit of MHz in this

chapter) and, therefore, $\boldsymbol{\alpha}(f)$ must belong to

$$C_{\text{attenuation}} = \left\{\mathbf{x} \in \mathbf{R}^{MN} : x_l \in [\alpha_{\text{lower}}, \alpha_{\text{upper}}], 1 \le l \le MN\right\}. \tag{5.6}$$

Second, the B-mode image information is used. That is, $\boldsymbol{\alpha}(f)$ must belong to C_{image}.

Express $\Delta\mathbf{a}$ as $\Delta\mathbf{a} = \left[\Delta A_1 \quad \Delta A_2 \quad \cdots \quad \Delta A_{N_{\text{A}}(N_{\text{A}}+1)/2}\right]^{\text{T}}$ and define

$$C_{\Delta A_i} = \left\{\mathbf{x} \in \mathbf{R}^{MN} : \left\langle \mathbf{x}, \mathbf{l}_i \right\rangle = \Delta A_i\right\}, i = 1,2,\cdots, N_{\text{A}}(N_{\text{A}}+1)/2\,, \tag{5.7}$$

then an attenuation coefficient distribution $\mathbf{x} \in C_{\text{attenuation}} \bigcap C_{\text{image}}$ minimizing the cost function (i.e., the total amount of violation of the attenuation data)

$$\Phi_{\text{A}}^{\text{s}}(\mathbf{x}) = \frac{1}{2}\sum_{i=1}^{N_{\text{A}}(N_{\text{A}}+1)/2} w_i d^2(\mathbf{x}, C_{\Delta A_i}) \tag{5.8}$$

can be found by taking $\mathbf{x}$ as the limit of the sequence $\{\mathbf{x}_n\}$. The $\mathbf{x}_0 \in C_{\text{attenuation}} \bigcap C_{\text{image}}$ is an initial attenuation coefficient distribution, and

$$\mathbf{x}_{n+1} = (1-\lambda_n)\mathbf{x}_n + \lambda_n P_{C_{\text{attenuation}} \cap C_{\text{image}}}\left[(1-\gamma)\mathbf{x}_n + \gamma \sum_{i=1}^{N_{\text{A}}(N_{\text{A}}+1)/2} w_i P_{C_{\Delta A_i}}(\mathbf{x}_n)\right], n \ge 0\,. \tag{5.9}$$

Each case in this chapter employed uniform weighting (i.e., each attenuation value is equally important), $\lambda_n = 0.5$ for all $n \ge 0$, and $\gamma = 1$.

5.3 Experimental results

The attenuation coefficient distributions at $f_0 = 5$ MHz (close to 5.57 MHz, the center frequency of the array) were reconstructed. To extract the attenuation data, the time $t_{ij,\text{p}}$ corresponding to the peak of the envelope of $e_{ij}(t)$ around $t_{ij,0}$ (with a

time window of $10\,\mu s$) was found, and then $a_{ij}(t)$ was extracted using the following equation:

$$a_{ij}(t) \equiv \begin{cases} w_{\mathrm{T}}(t+T/2-t_{ij,\mathrm{p}};r)e_{ij}(t) & t_{ij,\mathrm{p}}-T/2 \le t < t_{ij,\mathrm{p}}+T/2 \\ 0 & \text{elsewhere} \end{cases}, \tag{5.10}$$

where T is the duration of w_{T}, and

$$w_{\mathrm{T}}(t;r) = \begin{cases} \sin^2\left(\dfrac{\pi t}{rT}\right) & 0 \le t < \dfrac{rT}{2} \\ 1 & \dfrac{rT}{2} \le t \le T - \dfrac{rT}{2} \\ \sin^2\left[\dfrac{\pi(T-t)}{rT}\right] & T - \dfrac{rT}{2} < t \le T \\ 0 & \text{elsewhere} \end{cases} \tag{5.11}$$

is a Tukey window with a taper ratio of r [46]. $a_{\mathrm{w},ij}(t)$ was similarly extracted from $e_{\mathrm{w},ij}(t)$. In soft tissues, the attenuation coefficient is approximately a linear function of frequency in the MHz range [22], [45]. That is,

$$\alpha(x,y;f) \cong \alpha'(x,y)|f|. \tag{5.12}$$

Therefore, instead of (5.2), the following equation was used to estimate $\Delta A_{ij}(f_0)$ in order to increase the estimation stability:

$$\Delta A_{ij}(f_0) = \frac{1}{\Delta f}\int_{f_0-\Delta f/2}^{f_0+\Delta f/2} \frac{f_0}{f}\left\{-20\log_{10}\left(\left|A_{ij}(f)\right|\right) - \left[-20\log_{10}\left(\left|A_{\mathrm{w},ij}(f)\right|\right)\right]\right\} df\,. \tag{5.13}$$

In this chapter, $T = 4$ μ s, $r = 0.4$, and $\Delta f = 4$ MHz. The transmit/receive combinations removed when extracting the time-of-flight data were also removed here due to the invalidity of the assumption of straight-line propagation.

The attenuation coefficient images were reconstructed using the method introduced in Section 5.2 for the nine cases described in Chapter 4. All the reconstruction results are listed in Table 5.1. The errors are defined as

$$\Delta\alpha_{(\cdot)} = \alpha_{(\cdot),\text{recon}}(f_0) - \alpha_{(\cdot),\text{true}}(f_0), \tag{5.14}$$

where $(\cdot)$ denotes F (fat), C (cyst), T (high-attenuation tumor), IT (irregular tumor), G (glandular tissue), or ROI, $\alpha_{(\cdot),\text{true}}(f_0)$ is the attenuation coefficient listed in Table 4.1, and $\alpha_{(\cdot),\text{recon}}(f_0)$ is the reconstructed attenuation coefficient. In all cases the errors in the background region are small, but the errors in the ROI(s) are larger. Note that $\alpha_{\text{F,recon}}(f_0) = 0$ dB/cm in Case I and $\alpha_{\text{T,recon}}(f_0) = 10$ dB/cm in Case V have reached the lower bound and the upper bound for the attenuation coefficient, respectively. Also note that all $\Delta\alpha_{\text{F}}$ values are negative, and all $\Delta\alpha_{\text{C}}$, $\Delta\alpha_{\text{T}}$, and $\Delta\alpha_{\text{IT}}$ values are positive. This is mainly attributable to the energy redistribution caused by refraction. The fat sphere, which has a sound velocity lower than that of the background, tends to distribute more energy to the transmit/receive combinations with a path across the ROI, while the cyst sphere, high-attenuation tumor sphere, and the irregular tumor region, all having a sound velocity higher than that of the background, act contrary.

Table 5.1. The estimation results of the attenuation coefficients at $f_0 = 5$ MHz.

Case	ROI	Sphere radius (mm)	ROI position	$\alpha_{\text{ROI,true}}$ (dB/cm)	$\Delta\alpha'_{\text{ROI}}$ / $\Delta\alpha_{\text{ROI}}$ (dB/cm)	$\Delta\alpha'_{\text{G}}$ / $\Delta\alpha_{\text{G}}$ (dB/cm)
I	Fat	2	Center	2.21	–1.50/–2.21	–0.08/0.02
II	Fat	4	Center	2.21	–0.39/–1.22	–0.07/0.06
III	Fat	6	Center	2.21	–0.14/–0.78	–0.08/0.04
IV	Cyst	4	Center	0.78	0.87/3.64	–0.17/–0.17
V	HA tumor	4	Center	7.36	1.76/2.64	–0.09/–0.09
VI	Irregular tumor	N/A	Center	4.26	0.87/1.45	0.29/0.26
VII	Fat	4	Up	2.21	1.69/–0.24	–0.14/0.02
VIII	Fat	4	Down	2.21	–1.30/–1.19	–0.02/0.11
IX-1	Cyst	4	Upper-left	0.78	–0.07/2.82	0.00/0.02
IX-2	HA tumor	4	Upper-right	7.36	1.78/2.53	
IX-3	Fat	4	Down	2.21	–1.73/–2.05	

5.4 Experimental results with compensation for the refraction effects

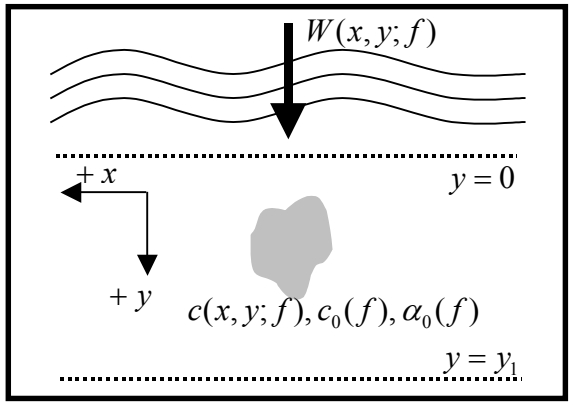

(a)

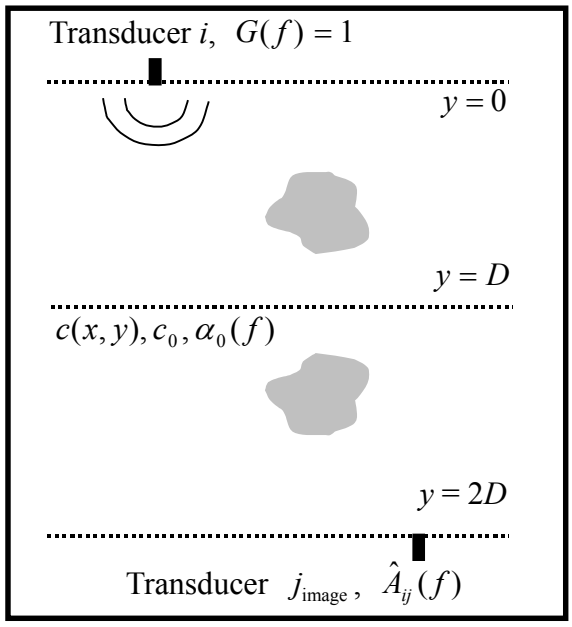

(b)

Fig. 5.1. Illustration of the technique for finding an estimate $\hat{A}_{ij}(f)$ of $A_{ij}(f)$. (a) Basic form of the problem. (b) Configuration used to find $\hat{A}_{ij}(f)$.

The estimation accuracy of the attenuation coefficient distributions will improve if the effects of refraction on the attenuation data can be compensated. Using the angular spectrum method [37], such effects can be roughly estimated by numerical propagation through the image object [15], [47], despite the density distribution and backscattering being ignored. Note that the effects of attenuation coefficient inhomogeneities on the attenuation data are also ignored since it is unknown at the

moment. With reference to Fig. 5.1(a), consider an acoustic wave $W(x,y;f)$ propagating along the $+y$ direction in a linear fluid medium with a sound velocity distribution of $c(x,y;f)$, a background sound velocity of $c_0(f)$, and an attenuation coefficient of $\alpha_0(f)$ independent of the position. The problem is: find $W(x,y_1;f)$ assuming that $W(x,0;f)$ is known.

$W(x,y_1;f)$ can be found by finding $W(x,\mathrm{d}y;f)$, $W(x,2\mathrm{d}y;f)$, $\cdots$, and $W(x,N_y\mathrm{d}y;f)$ sequentially with $N_y\mathrm{d}y = y_1$. Assume that $W(x,q\mathrm{d}y;f)$ has been found. Let the angular spectrum of $W(x,q\mathrm{d}y;f)$ be $\tilde{W}(k_x;q\mathrm{d}y,f)$, i.e.,

$$W(x,q\mathrm{d}y;f) = \frac{1}{2\pi}\int \tilde{W}(k_x;q\mathrm{d}y,f)\exp(jk_x x)dk_x\,, \tag{5.15}$$

then

$$W(x,(q+1)\mathrm{d}y;f) \cong \frac{h_q(x;f)}{2\pi}\int_{-2\pi f/c_0(f)}^{2\pi f/c_0(f)} H(k_x;\mathrm{d}y,f)\tilde{W}(k_x;q\mathrm{d}y,f)\exp(jk_x x)dk_x\,, \tag{5.16}$$

where

$$h_q(x;f) = \exp\left\{j2\pi f\int_{q\mathrm{d}y}^{(q+1)\mathrm{d}y}\left[c^{-1}(x,y;f) - c_0^{-1}\right]dy\right\} \tag{5.17}$$

and

$$H(k_x;\mathrm{d}y,f) = \exp\left[j2\pi\mathrm{d}y\sqrt{(f/c_0)^2 - k_x^2}\right]\cdot 10^{-\frac{\alpha(f)\mathrm{d}y}{20}\left\{\cos\left[\sin^{-1}(k_x c_0/f)\right]\right\}^{-1}} \quad [48]. \tag{5.18}$$

An estimate $\hat{A}_{ij}(f)$ of $A_{ij}(f)$ can be obtained using the above method by considering the configuration in Fig. 5.1(b), in which $G(f)$ is the temporal spectrum of the transmitted signal, $c(x,y;f) = c(x,y)$, $0 \le y \le D$ (the distance between the array and the metal plate), is the reconstructed sound velocity distribution and independent of f, c_0 is the sound velocity in the background, and $\alpha_0(f) = 0.5f$ dB/cm with f in the unit of MHz. Note that $c(x,y;f) = c(x,2D-y;f)$ for $D \le y \le 2D$. The estimate of $A_{\mathrm{w},ij}(f)$, $\hat{A}_{\mathrm{w},ij}(f)$, was similarly obtained with $c(x,y;f) = c_0$ and $\alpha(f) = 0$. Define

$$\Delta\hat{A}_{ij}(f) = -20\log_{10}\left(\left|\hat{A}_{ij}(f)\right|\right) - \left[-20\log_{10}\left(\left|\hat{A}_{\mathrm{w},ij}(f)\right|\right)\right], \tag{5.19}$$

then a vector $\Delta\mathbf{a}' = \Delta\mathbf{a}'(f)$ consisting of $\Delta A'_{ij}(f) = \Delta A_{ij}(f) - \Delta\hat{A}_{ij}(f)$ can be built. After solving

$$\mathbf{L}\boldsymbol{\alpha} = \Delta\mathbf{a}' \tag{5.20}$$

using the convex programming formulation introduced in Section 5.2, the attenuation coefficient distribution with compensation is

$$\boldsymbol{\alpha}' = \boldsymbol{\alpha} + \alpha_0(f_0)\,. \tag{5.21}$$

All the reconstruction results with the refraction effects being (partly) compensated are also listed in Table 5.1. The errors are denoted as $\Delta\alpha'_{(\cdot)}$. The reconstructed attenuation coefficient images are shown in Fig. 5.2–Fig. 5.5. Fig. 5.2–Fig. 5.4 demonstrate the effects on the reconstruction accuracy of the size of the spherical objects, different sound velocities and attenuation coefficients in the objects, and the depth of the objects, respectively. In all cases the errors in the background region are small. Fig. 5.2(a) and (b), Fig. 5.2(c) and (d), and Fig. 5.2(e) and (f) show the estimation results corresponding to fat spheres with a radius of 2 mm, 4 mm, and 6 mm, respectively. The left panels [Fig. 5.2(a), (c), and (e)] are the estimated attenuation coefficient images with compensation, and the right panels [Fig. 5.2(b), (d), and (f)] are the estimated attenuation coefficient images without compensation. The $\Delta\alpha'_{\mathrm{ROI}}$ ($\Delta\alpha_{\mathrm{ROI}}$) values are –1.50 (–2.21) dB/cm, –0.39 (–1.22) dB/cm, and –0.14 (–0.78) dB/cm, respectively, and those of $\Delta\alpha'_{\mathrm{G}}$ ($\Delta\alpha_{\mathrm{G}}$) are –0.08 (0.02) dB/cm, –0.07 (0.06) dB/cm, and –0.08 (0.04) dB/cm, respectively. Fig. 5.3(a) and (b), Fig. 5.3(c) and (d), and Fig. 5.3(e) and (f) show the estimated attenuation coefficient images with and without compensation corresponding to spheres consisting of different tissues (cyst, fat, and tumor, respectively). The $\Delta\alpha'_{\mathrm{ROI}}$ ($\Delta\alpha_{\mathrm{ROI}}$) values are 0.87 (3.64) dB/cm, –0.39 (–1.22) dB/cm, and 1.76 (2.64) dB/cm, respectively, and those of $\Delta\alpha'_{\mathrm{G}}$ ($\Delta\alpha_{\mathrm{G}}$) are –0.17 (–0.17) dB/cm, –0.07 (0.06) dB/cm, and –0.09 (–0.09) dB/cm, respectively. Fig. 5.4(a) and (b), Fig. 5.4(c) and (d), and Fig. 5.4(e) and (f) show the estimated attenuation coefficient images with and without compensation corresponding to fat spheres at different positions (upper, center, and lower, respectively). The $\Delta\alpha'_{\mathrm{ROI}}$ ($\Delta\alpha_{\mathrm{ROI}}$) values are 1.69 (–0.24) dB/cm, –0.39 (–1.22) dB/cm, and –1.30 (–1.19) dB/cm, respectively, and those of $\Delta\alpha'_{\mathrm{G}}$ ($\Delta\alpha_{\mathrm{G}}$) are –0.14 (0.02) dB/cm, –0.07 (0.06) dB/cm, and –0.02 (0.11) dB/cm, respectively.

Finally, Fig. 5.5(a) and (b), and Fig. 5.5(c) and (d) show the estimated attenuation coefficient images with and without compensation for Case VI and Case IX, respectively. In Case VI, $\Delta\alpha'_{\mathrm{IT}} = 0.87$ dB/cm ($\Delta\alpha_{\mathrm{IT}} = 1.45$ dB/cm) and $\Delta\alpha'_{\mathrm{G}} = 0.29$ dB/cm ($\Delta\alpha_{\mathrm{G}} = 0.26$ dB/cm). In Case IX, $\Delta\alpha'_{\mathrm{C}} = -0.07$ dB/cm ($\Delta\alpha_{\mathrm{C}} = 2.82$ dB/cm), $\Delta\alpha'_{\mathrm{T}} = 1.78$ dB/cm ($\Delta\alpha_{\mathrm{T}} = 2.53$ dB/cm), $\Delta\alpha'_{\mathrm{F}} = -1.73$ dB/cm ($\Delta\alpha_{\mathrm{F}} = -2.05$ dB/cm), and $\Delta\alpha'_{\mathrm{G}} = 0.00$ dB/cm ($\Delta\alpha_{\mathrm{G}} = 0.02$ dB/cm). Except for Case VII and VIII, the reconstruction accuracy in the ROI was improved with the compensation technique.

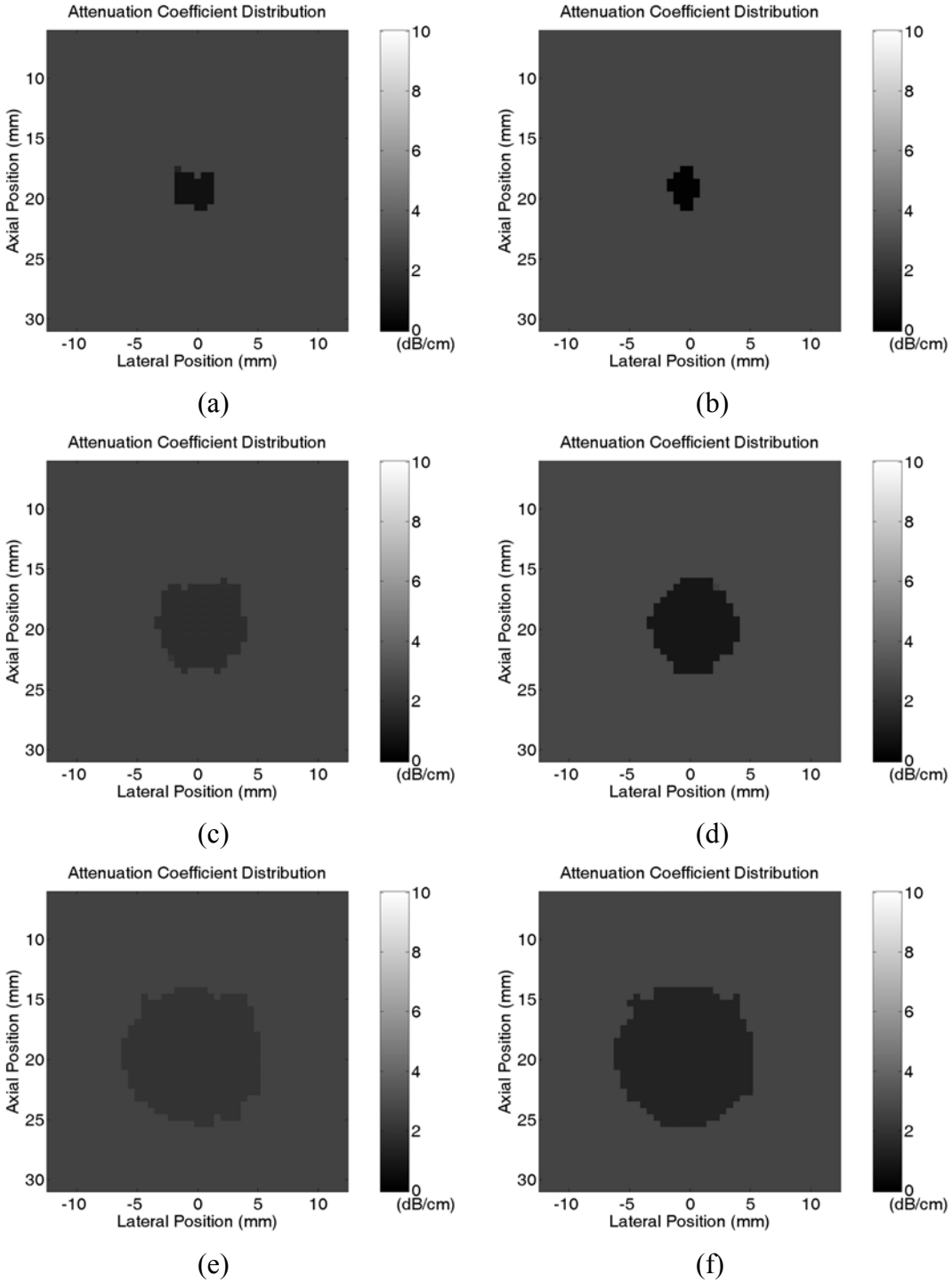

Fig. 5.2. Estimated attenuation coefficient images, with and without compensation, of objects containing fat spheres ($c_F = 1464$ m/s, $\rho_F = 0.94$ g/cm^3, and $\alpha_F = 2.21$ dB/cm) with different radii. (a) and (b): Case I (radius = 2 mm). (c) and (d): Case II (radius = 4 mm). (e) and (f): Case III (radius = 6 mm).

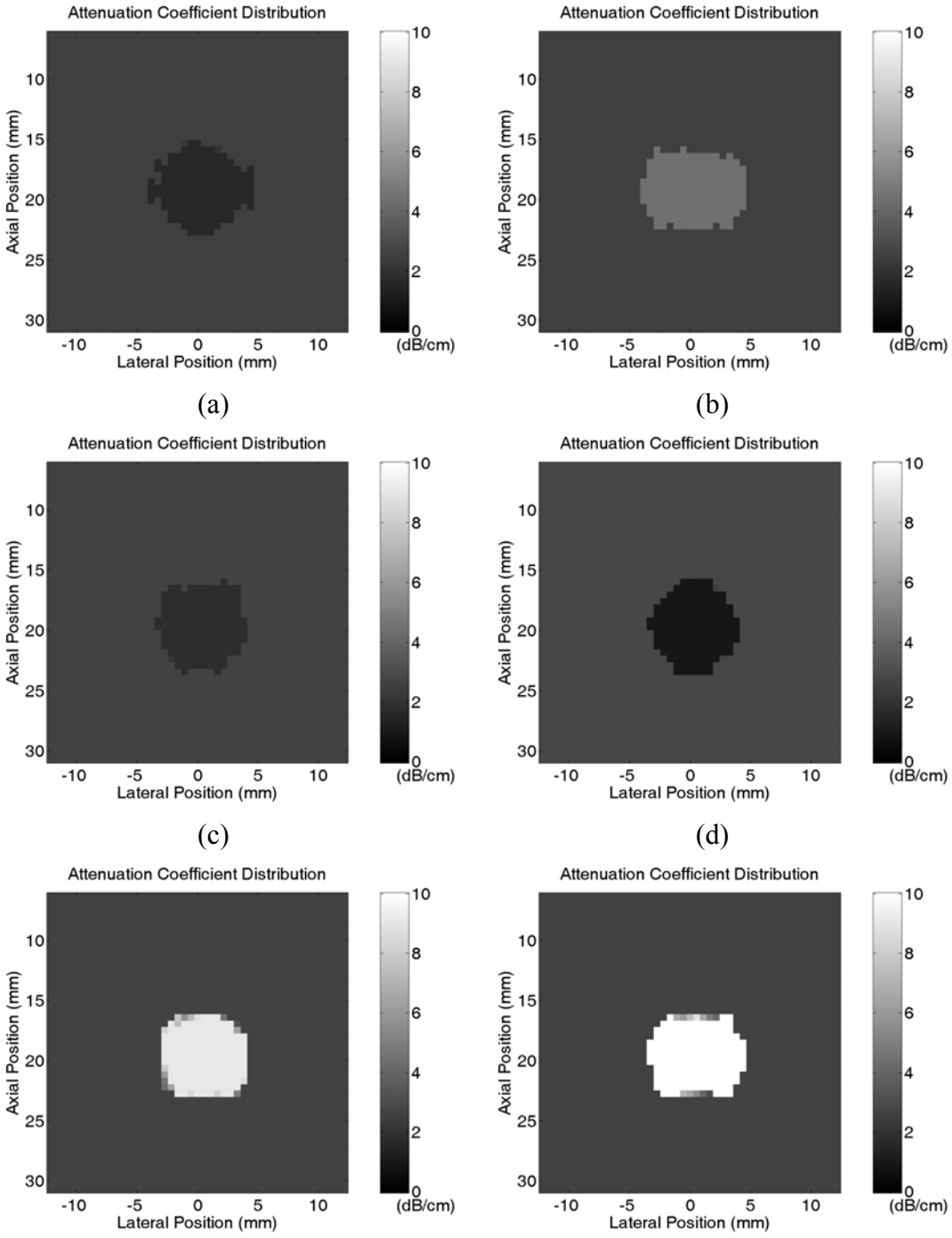

Fig. 5.3. Estimated attenuation coefficient images, with and without compensation, of objects containing spheres all with a radius of 4 mm but representing different tissue types. (a) and (b): Case IV (cyst; $c_{\mathrm{C}} = 1570\,\mathrm{m/s}$, $\rho_{\mathrm{C}} = 1.02\,\mathrm{g/cm^3}$, and $\alpha_{\mathrm{C}} = 0.78\,\mathrm{dB/cm}$). (c) and (d): Case II (fat; $c_{\mathrm{F}} = 1464\,\mathrm{m/s}$, $\rho_{\mathrm{F}} = 0.94\,\mathrm{g/cm^3}$, and $\alpha_{\mathrm{F}} = 2.21\,\mathrm{dB/cm}$). (e) and (f): Case V (tumor; $c_{\mathrm{T}} = 1547\,\mathrm{m/s}$, $\rho_{\mathrm{T}} = 1.10\,\mathrm{g/cm^3}$, and $\alpha_{\mathrm{T}} = 7.36\,\mathrm{dB/cm}$).

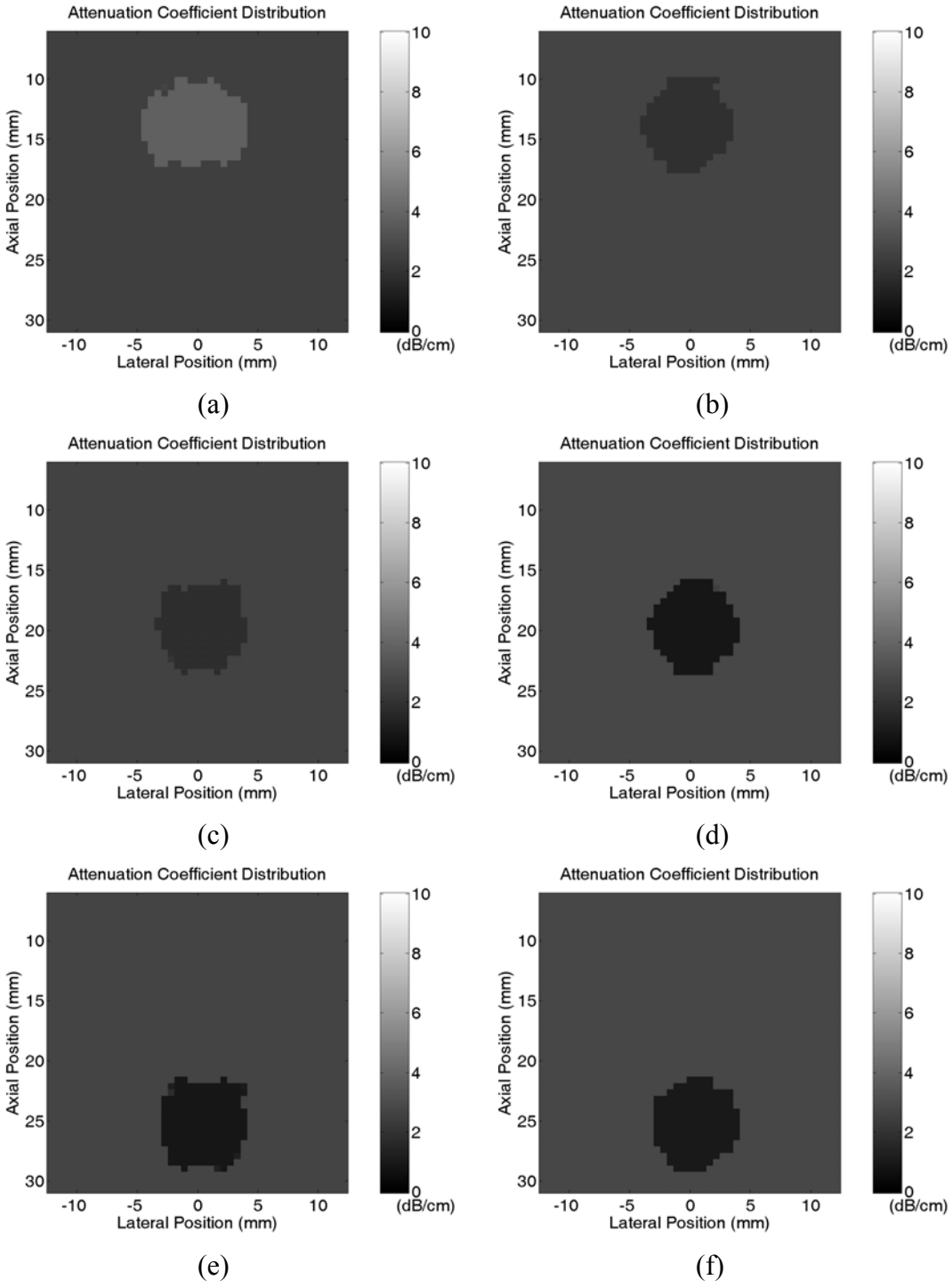

Fig. 5.4. Estimated attenuation coefficient images, with and without compensation, of objects containing fat spheres ($c_{\mathrm{F}} = 1464\,\mathrm{m/s}$, $\rho_{\mathrm{F}} = 0.94\,\mathrm{g/cm^3}$, and $\alpha_{\mathrm{F}} = 2.21\,\mathrm{dB/cm}$) all with a radius of 4 mm but at different positions. (a) and (b): Case VII (the sphere is above the center). (c) and (d): Case II (the sphere is at the center). (e) and (f): Case VIII (the sphere is below the center).

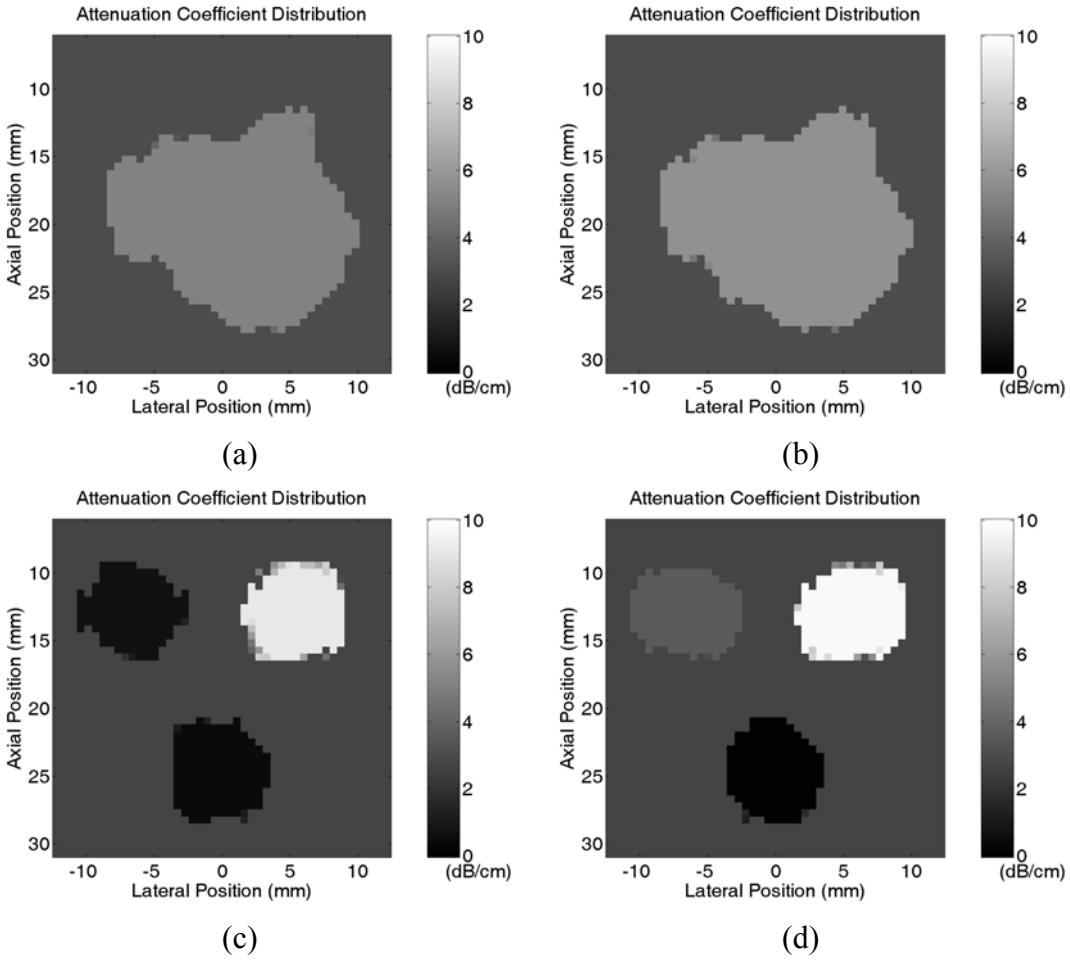

Fig. 5.5. Estimated attenuation coefficient images with and without compensation. (a) and (b): Case VI. The image object contains an irregular tumor. $c_{\mathrm{IT}} = 1553\,\mathrm{m/s}$, $\rho_{\mathrm{IT}} = 1.07\,\mathrm{g/cm^3}$, and $\alpha_{\mathrm{T}} = 4.26\,\mathrm{dB/cm}$. (c) and (d): Case IX. The image object contains three spheres, all with a radius of 4 mm ($c_{\mathrm{C}} = 1570\,\mathrm{m/s}$, $\rho_{\mathrm{C}} = 1.02\,\mathrm{g/cm^3}$ and $\alpha_{\mathrm{C}} = 0.78\,\mathrm{dB/cm}$ in the upper-left cyst sphere; $c_{\mathrm{T}} = 1547\,\mathrm{m/s}$, $\rho_{\mathrm{T}} = 1.10\,\mathrm{g/cm^3}$ and $\alpha_{\mathrm{T}} = 7.36\,\mathrm{dB/cm}$ in the upper-right high-attenuation tumor sphere; and $c_{\mathrm{F}} = 1464\,\mathrm{m/s}$, $\rho_{\mathrm{F}} = 0.94\,\mathrm{g/cm^3}$, and $\alpha_{\mathrm{F}} = 2.21\,\mathrm{dB/cm}$ in the lower fat sphere).

5.5 Concluding remarks

In this chapter, the attenuation coefficient distributions were reconstructed for the nine cases described in Chapter 4 using the convex programming formulation. Furthermore, in order to improve the estimation accuracy, a technique based on the angular spectrum method was developed to compensate the effects of refraction on the attenuation data. With this technique, the reconstruction accuracy in the ROI was improved except for Case VII and VIII. To verify the efficacy of the compensation technique for complex objects, more studies are needed.

The attenuation coefficient distribution in the breast can be used to enhance the detection of the breast caner. Using only the sound velocity image, a fat region is distinguishable from a tumor, but a cyst may not be due to their close sound velocities. Since the experimental results show that the difference between the reconstructed attenuation coefficients in a cyst and a tumor is large, when a cyst and a tumor are indistinguishable using the B-mode image and the sound velocity image, the attenuation coefficient image can be used to help distinguish them.

Chapter 6 Discussion

6.1 Aberration correction

Sound velocity inhomogeneities results in waveform distortions in B-mode pulse-echo data, including phase aberrations and wavefront amplitude distortions [5]–[9]. With the imaging setup shown in Fig 1.1, the reconstructed sound velocity distribution can be used to perform aberration correction and hence improve the B-mode image quality.

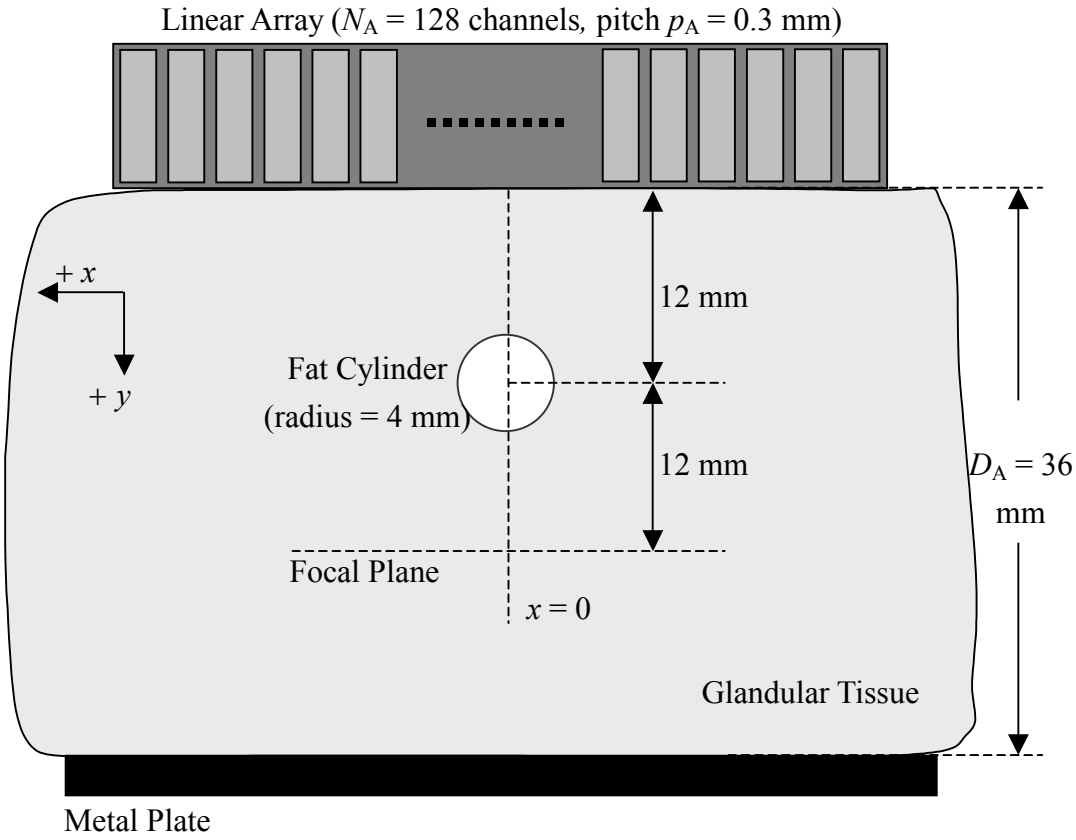

Fig. 6.1. Image object considered in this chapter. It comprises a glandular tissue with a cylinder of fat with a radius of 4 mm at its center.

Consider the image object shown in Fig. 6.1. The *k*-space method [33] introduced in Section 3.1 was used to generate the required data. The parameters of the fat cylinder and the glandular tissue are those listed in Table 4.1 and each array channel has a Gaussian frequency response with a center frequency of 5 MHz and a

two-way -12 dB fractional bandwidth of 0.6. The B-mode image and the sound velocity distribution were reconstructed using the same settings as those used in Chapter 4 except for all channel data being available in this case. When calculating the beam patterns and the point spread functions (PSFs), only the central 50 elements in the array were used (i.e., the F-number was 1.6). Fig. 6.2(a) shows the normalized transmit beam patterns at the focal plane corresponding to three different conditions: without the fat cylinder in the image object (solid line), with the fat cylinder in the image object (dashed line), and with the fat cylinder in the image object and aberration correction using a technique similar to that developed in Section 5.4 for compensating the refraction effects (dotted line). The normalized receive beam patterns and two-way beam patterns are shown in Fig. 6.2(b) and (c), respectively, and Fig. 6.2(d)–(f) shows the two-way PSFs without the fat cylinder in the image object, with the fat cylinder in the image object, and with the fat cylinder in the image object and aberration correction, respectively, with a 60-dB dynamic range. The simulation results show that using the sound velocity distribution to compensate for the waveform distortions can improve the focusing performances.

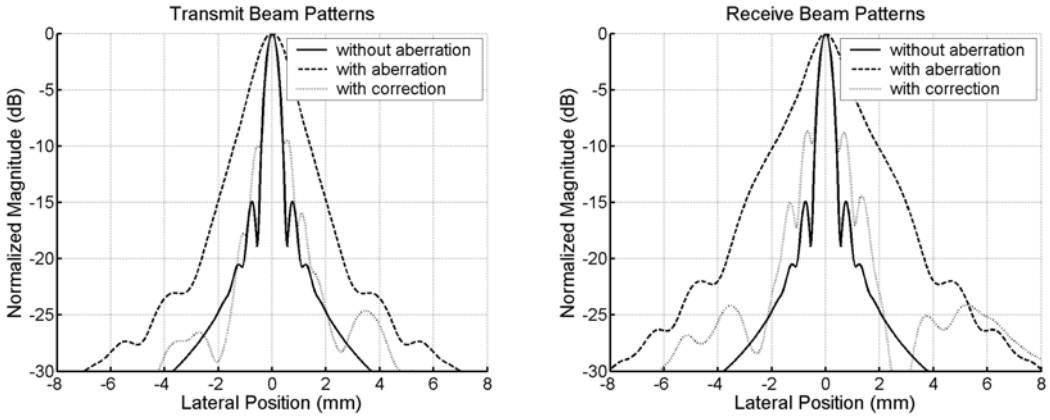

(a) (b)

Fig. 6.2. (a) Normalized transmit beam patterns at the focal plane. (b) Normalized receive beam patterns at the focal plane. (c) Normalized two-way beam patterns at the focal plane (d) Two-way PSF without the fat cylinder in the image object. (e) Two-way PSF with the fat cylinder in the image object. (f) Two-way PSF with the fat cylinder in the image object and with aberration correction. The PSFs are displayed with a 60-dB dynamic range.

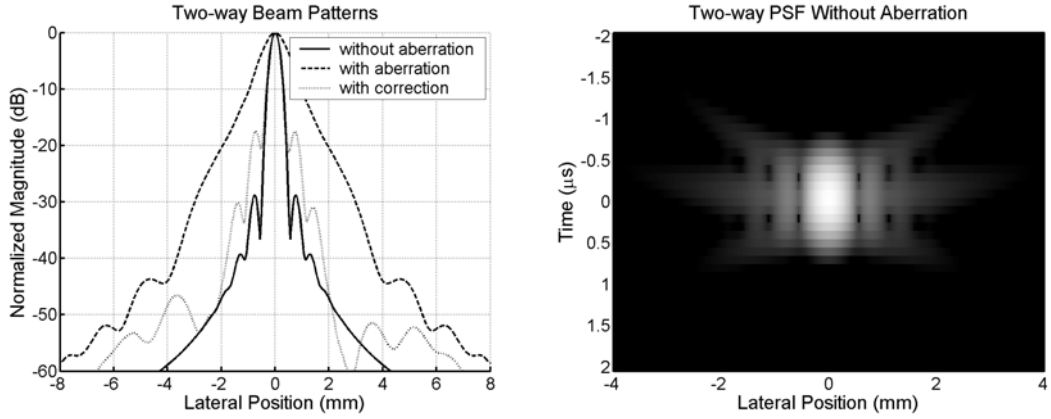

(c) (d)

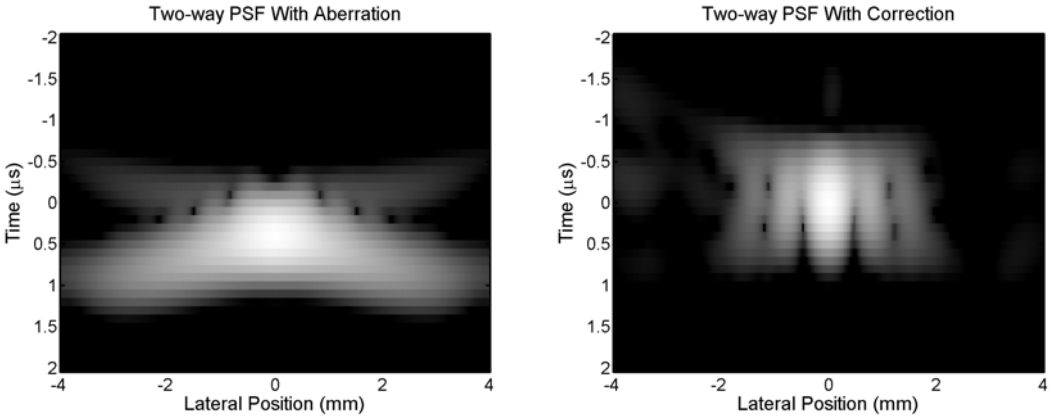

(e) (f)

Fig. 6.2. (Continued.)

6.2 SNR enhancement

To acquire the time-of-flight data, only one channel transmits at each firing. In this thesis, no noise was added in the simulations and the SNR was enhanced with averaging in experiments. However, in order to reduce the time required for collecting the time-of-flight data, no averaging will be preferable. In this situation, the SNR may be insufficient due to attenuation and thus affecting the accuracy of time-of-flight estimation. To address this problem, coded excitation techniques [43] can be employed to increase the transmitted power while maintaining good temporal resolution. Note that an SNR enhancement of more than 20 dB is achievable because the code length is only limited by the distance between the metal plate and the array when only one channel is fired.

The time-of-flight data collected by transmitting a coded signal were compared

with those collected by transmitting a wideband pulse. The image object and the array were those shown in Fig. 6.1. The coded signal was a binary Tukey-windowed chirp described in Section A.4.1 with $f_0 = 5\,\text{MHz}$, $\Delta f = 3.25\,\text{MHz}$, $T = 10\,\mu\text{s}$, and $r = 0.15$. The other parameters were $f_{\text{s,ADC}} = 80\,\text{MHz}$, $M = 36$, $\beta = 3.7$, $f_{\text{c}} = 0.05625$, $D = 10$, and $\sigma_{\text{w}}^2 = 1$. The compression filter was designed using the method described in Section A.3. The mainlobe was defined as the central nine points of the compressed signal, $N_{\text{f}} = 80$, and $s_{\text{dB}} =$ –40 dB. Fig. 6.3 shows the geometrically compensated time-of-flight data collected by transmitting the binary Tukey-window chirp (dashed line) and the wideband pulse (solid line) at the 64th channel. Note that all the removed time-of-flight data were replaced with 0. The time-of-flight data corresponding to different transmitting signals are close to each other for the same transmit/receive combinations; therefore, applying coded excitation to SNR enhancement when collecting the time-of-flight data may be feasible.

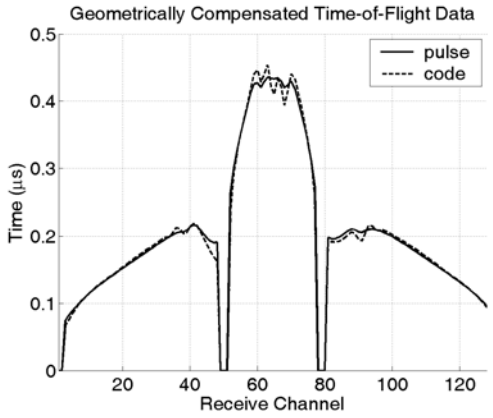

Fig. 6.3. The geometrically compensated time-of-flight data collected by transmitting the binary Tukey-window chirp (dashed line) and the wideband pulse (solid line) at the 64th channel. The image object and the array were those shown in Fig. 6.1. Note that all the removed time-of-flight data were replaced with 0.

Chapter 7 Conclusions and future works

In this thesis, a limited-angle transmission tomography setup using a linear array was investigated. This setup can be used to obtain the B-mode image, the sound velocity distribution, and the attenuation coefficient distribution. To improve the estimation accuracy of sound velocity distribution, a new reconstruction algorithm incorporating segmentation information from the B-mode image of the same object was proposed. Simulation results and experimental results demonstrate the efficacy of the algorithm. Furthermore, with the sound velocity distribution, waveform distortions caused by sound velocity inhomogeneities can be partly compensated. When reconstructing the attenuation coefficient distribution, in addition to incorporating information from the B-mode image, the sound velocity distribution of the same object was used to compensate the effects of refraction in order to improve the estimation accuracy. The efficacy of the compensation technique was demonstrated using experimental data.

To enhance the detection of breast cancer, B-mode image, sound velocity distribution, and attenuation coefficient distribution can be applied in order. When a region cannot be identified using the B-mode image, this region can be rejected as a tumor if its sound velocity is lower than a threshold (e.g., 1500 m/s). If the sound velocity in this region is higher, the attenuation coefficient can then be used to distinguish a tumor from a cyst.

Future works include an efficient implementation of the reconstruction algorithms, realization of coded excitation, further investigation on the application of the sound velocity information and attenuation coefficient information to aberration correction, and performance evaluation of the technique in clinical situations.

Appendix A Arbitrary waveform coded excitation using bipolar square wave pulsers in medical ultrasound

This appendix presents a new coded excitation scheme that efficiently synthesizes codes for arbitrary waveforms using a bipolar square wave pulser. In a coded excitation system, pulse compression is performed to restore the axial resolution. If the system can transmit waveforms with specific spectral characteristics, pulse compression at the receiver – which typically involves inverse filtering – can be implemented more efficiently. However, such a transmitter requires the generation of arbitrary waveforms and is therefore more expensive. In other words, a trade-off is necessary between the compression performance and the transmitter cost. Here we propose a method that preserves the low-cost advantage of a bipolar pulser while achieving approximately the same compression performance as an arbitrary waveform generator. The key idea of the proposed method is the conversion of a nonbinary code (i.e., requiring an arbitrary waveform generator) with good compression performance into a binary code (i.e., requiring only a bipolar pulser) by code translation and code tuning. The code translation is implemented by sending the nonbinary code into a virtual one-bit sigma-delta modulator, and the code tuning involves minimizing the root-mean-square error between the resultant binary code and the original nonbinary code by sequential and iterative tuning, whilst taking the transducer response into account. Tukey-windowed chirps – which have good compression performance – of different durations (16, 20, and 24 μs), all with a taper ratio of 0.15, a center frequency of 2.5 MHz, and an equivalent bandwidth of 1.5 MHz, were converted into binary Tukey-windowed chirps that were compared with pseudochirps (i.e., direct binary approximations of the original chirp) over the same spectral band. The bit rate was 40 MHz. Simulation results show that the use of binary Tukey-windowed chirps can reduce the code duration by 20.6% or the peak sidelobe level by 6 dB compared to the commonly used pseudochirps. Experimental results obtained under the same settings were in agreement with the simulations. Our results demonstrate that arbitrary waveform coded excitation can be realized using bipolar square wave pulsers for applications in medical ultrasound.

A.1 Introduction

Coded excitation has been studied for many years in medical ultrasound [43], [49]–[62]. It is primarily used to either improve the signal-to-noise ratio (SNR) without increasing the excitation voltage or lower the excitation voltage without sacrificing the SNR [43], [49]–[51]. Other applications of coded excitation include increasing the frame rate and improving resolution [52], enhancing the detection of contrast agent [53], increasing the depth of field [54], improving the SNR in finite amplitude distortion based harmonic imaging [55], enhancing the generation of harmonics by contrast agent microbubbles [56], [57], and suppressing selected harmonic components in nonlinear imaging [58].

In this study, coded excitation is treated as an approach to improving the SNR under the condition of a fixed peak acoustic power. In a coded excitation system, a wide transmit bandwidth is maintained while the transmit pulse length is increased. Thus, the axial resolution can be preserved at the receiver with pulse compression. If multiple firings along the same direction are allowed, the use of (orthogonal) Golay coded excitation [50] makes pulse compression straightforward, in which case the axial sidelobes after pulse compression are eliminated by filtering and by cancellation in the coherent sum of the received signals corresponding to different firings. However, pulse compression becomes more challenging when only single firing is allowed for each beam direction, since only filtering can be used to restore the axial resolution. In this study, we only consider the single-firing case.

The performance of pulse compression is generally characterized by the mainlobe width (related to the axial resolution), the sidelobe level (related to the dynamic range and contrast resolution), and the SNR improvement. Given a code, once the filter length is fixed, the more stringent the constraints [such as the mainlobe width or the peak sidelobe level (PSL)] imposed on the compression results, the lower the output SNR is. Furthermore, the filter must be extended when the constraints cannot be satisfied. Therefore, the code must be properly designed to meet the system requirements.

Achieving optimal pulse compression performance requires the ability to generate an arbitrary transmit waveform in order to realize the desired spectral characteristics. However, an arbitrary waveform generator is expensive. Here we propose a method that preserves the low-cost advantage of a bipolar pulser while achieving compression performance similar to that of an arbitrary waveform generator.

The key idea of the proposed method is the conversion of a nonbinary code into a binary code by code translation and code tuning. The code translation is implemented by sending the nonbinary code into a virtual one-bit sigma-delta modulator, and the code tuning involves minimizing the root-mean-square error between the resultant binary code and the original nonbinary code by sequential and iterative tuning using the output of the sigma-delta modulator as the initial condition, whilst taking the transducer response into account. It is shown that good compression performance can be achieved by using the converted binary code instead of the original code. Hence, the proposed method can be used to effectively realize arbitrary waveform coded excitation with bipolar pulsers.

This appendix is organized as follows. Section A.2 describes the method used to translate an arbitrary code into a binary code, and the method used to tune the binary code. Section A.2.4 introduces the formulas for designing the compression filter. Section A.3 demonstrates the efficacy of the proposed method using simulations and experimental data. Section A.4 discusses characteristics, applications, and extensions of the proposed method, and the appendix concludes in Section A.5.

A.2 Code conversion

The overall goal of code conversion is to convert a nonbinary code into a binary code that exhibits similar compression performance. A two-step method was developed to achieve this goal. The first step uses a sigma-delta modulator to translate the nonbinary code into a temporary binary code. As shown in Section A.2.3, this temporary code only exhibits acceptable compression performance when the bit rate is excessive, and hence a second step is needed. The algorithm introduced in Section A.2.4 is employed as the second step to tune the temporary code into a new code which has improved compression performance.

A.2.1 Sigma-delta modulation

Let $x(t)$ be a band-limited continuous time signal and $x(n)$ be its corresponding discrete time signal uniformly sampled at f_s:

$$x(n) = x(t)\big|_{t=n/f_s}. \tag{A.1}$$

In this Appendix, t denotes the time, and the letters n, k, p, q, and l within

parentheses denote discrete time indices.

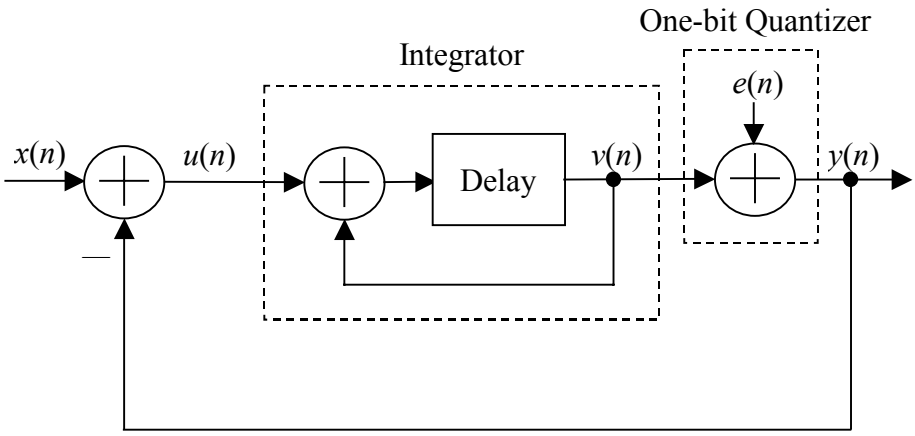

Fig. A.1. Block diagram of the first-order one-bit sigma-delta modulator.

Fig. A.1 shows a block diagram of a first-order one-bit sigma-delta modulator [63], where $e(n)$ is the quantization error. Note that the entire system is in the discrete domain because the modulator is only used for discrete code conversion (and not analog-to-digital conversion). Without loss of generality, assume that the input signal $x(n)$ is bounded by $\pm V$ and that the output signal $y(n)$ is within $\{+1,-1\}$. The quantizer will not be overloaded if $V=1$ and $|v(0)| \le 2$, (i.e., $|e(n)| \le 1$ for all $n \ge 0$). Based on Fig. A.1,

$$v(n) = y(n) - e(n), \tag{A.2}$$

$$\begin{aligned} v(n) &= u(n-1) + v(n-1) = [x(n-1) - y(n-1)] + [y(n-1) - e(n-1)] \\ &= x(n-1) - e(n-1) \end{aligned}. \tag{A.3}$$

Thus,

$$y(n) = x(n-1) + e(n) - e(n-1). \tag{A.4}$$

If f_s is much higher than the bandwidth of $x(n)$, $x(n)$ can be efficiently reconstructed by appropriately filtering $y(n)$.

A.2.2 Code translation

Let $x(t)$ be the desired band-limited waveform for coded excitation. The goal is to build a binary version of the original code such that after being filtered by the transducer, the filtered binary waveform is similar to the filtered version of the original code. In other words, the transducer's frequency response is used as the

reconstruction filter in a sigma-delta modulator. We first choose a sampling frequency f_s and discretize $x(t)$ into $x(n)$, then send the sequence $x(n)$ into the sigma-delta modulator shown in Fig. A.1. The output signal $y(n)$ of the modulator is the corresponding binary code of $x(t)$ with a bit rate of f_s, and the actual transmitted signal is

$$y(t; f_s) = \sum_n y(n+1)\Pi\left(f_s t - n\right), \tag{A.5}$$

where

$$\Pi(t) = \begin{cases} 1 \text{ if } 0 \le t \le 1 \\ 0 \text{ otherwise} \end{cases}. \tag{A.6}$$

A.2.3 Preliminary evaluation

Let $h_t(t)$ be the impulse response of the transducer and $\otimes$ denote convolution. It is desirable for $x(t) \otimes h_t(t) \otimes h_t(t)$ to have a flat spectrum over the passband so that compression, which typically involves inversion filtering, can be efficiently implemented at the receiver. Since $h_t(t)$ can be viewed as the reconstruction filter for the sigma-delta modulator, a higher f_s is desired such that $y(t; f_s) \otimes h_t(t)$ is approximately the same as $x(t) \otimes h_t(t)$. However, f_s is also the bit rate of the binary code and must be within a certain range due to hardware limitations of the bipolar pulser.

The effects of the bit rate on pulse compression are illustrated using a Tukey-windowed chirp [59] as an example. Specifically,

$$x(t) = w_T(t; r) \sin\left\{2\pi\left[\left(f_0 - \frac{\Delta f}{2}\right)t + \frac{\alpha}{2}t^2\right]\right\}, 0 \le t \le T, \tag{A.7}$$

where f_0 is the carrier frequency, Δf is the bandwidth of the linear chirp, T is the pulse duration, α is the slope of the linear chirp (i.e., $\alpha = \Delta f / T$), and

$$w_T(t; r) = \begin{cases} \sin^2\left(\dfrac{\pi t}{rT}\right) & 0 \le t < \dfrac{rT}{2} \\ 1 & \dfrac{rT}{2} \le t \le T - \dfrac{rT}{2} \\ \sin^2\left[\dfrac{\pi(T-t)}{rT}\right] & T - \dfrac{rT}{2} < t \le T \\ 0 & \text{elsewhere} \end{cases} \tag{A.8}$$

is a Tukey window with a taper ratio of r [46]. The compression filter $h_c(t)$ is chosen to be a windowed matched filter:

$$h_c(t) = w_C(t) \cdot \sin\left\{2\pi\left[\left(f_0 - \frac{\Delta f}{2}\right)(T-t) + \frac{\alpha}{2}(T-t)^2\right]\right\}, 0 \le t \le T, \quad \text{(A.9)}$$

where $w_C(t)$ is a Chebyshev window with a sidelobe attenuation of -90 dB [64]. The signal

$$x_c(t) = x(t) \otimes h_t(t) \otimes h_t(t) \otimes h_c(t) \quad \text{(A.10)}$$

is the ideal pulse-echo compressed signal and is used as a reference to evaluate the pulse-echo compression results at different bit rates:

$$y_c(t; f_s) = y(t; f_s) \otimes h_t(t) \otimes h_t(t) \otimes h_c(t). \quad \text{(A.11)}$$

Let $f_0 = 2.5$ MHz, $\Delta f = 1.85$ MHz, $T = 20$ μs, $r = 0.3$, and the transducer have a Gaussian frequency response with a center frequency of f_0 and a -6 dB bandwidth of 1.5 MHz. Fig. A.2 shows the normalized envelopes of $x_c(t)$ (solid line) and $y_c(t; f_s)$ for $f_s = 40$, 100, and 200 MHz (dotted line, dash-dotted line, and dashed line, respectively). Fig. A.2 demonstrates that $y(t; f_s)$ with a higher f_s has lower axial sidelobes after compression.

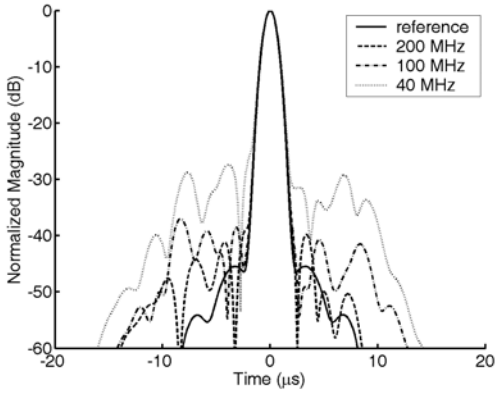

Fig. A.2. Normalized envelopes of $x_c(t)$, and $y_c(t; f_s)$ for $f_s = 40$, 100, and 200 MHz.

A.2.4 Code tuning

Fig. 2 shows that the PSL exceeds –30 dB with a bit rate of 40 MHz, and that a rate of 200 MHz is needed to suppress the PSL to the –40 dB level. Such a high bit rate is not acceptable in most systems. In addition to the filtering approach commonly

used in the literature [1], [13], tuning of the output code $y(n)$ of the sigma-delta modulator is performed in this study to further improve the compression results.

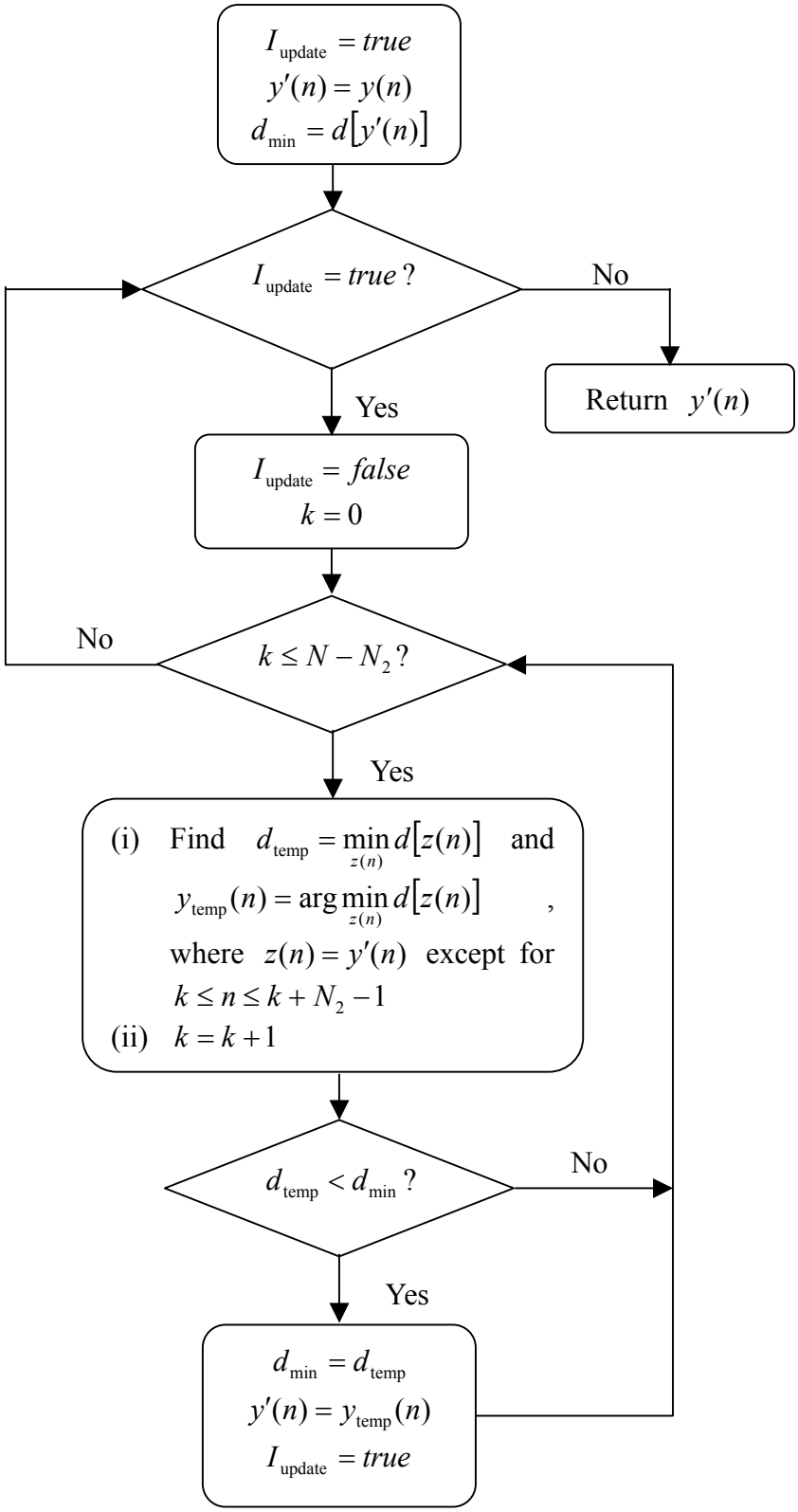

Fig. A.3. Flow diagram for code tuning.

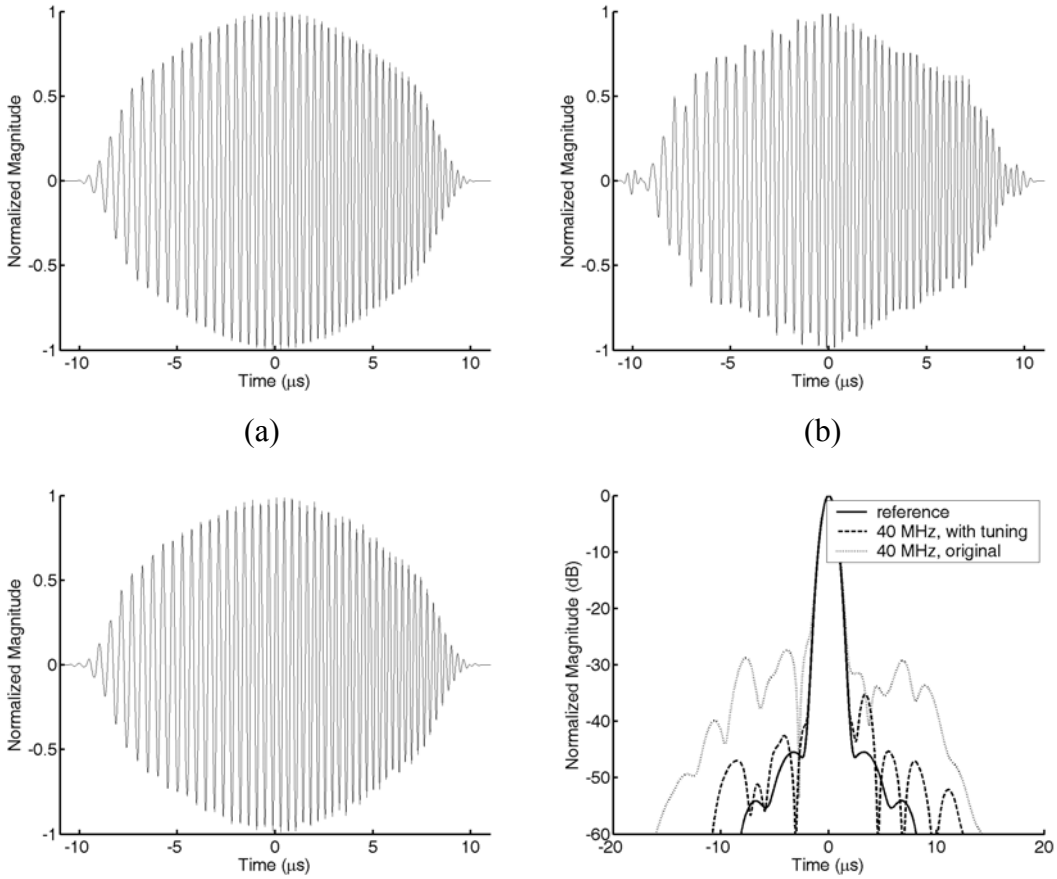

Fig. A.4. (a) $x(t) \otimes h_t(t)$. (b) $y(t;40\text{ MHz}) \otimes h_t(t)$. (c) $y'(t;40\text{ MHz}) \otimes h_t(t)$. (d) Normalized envelopes of $x_c(t)$ (solid line), $y_c(t;40\text{ MHz})$ (dotted line), and $y'_c(t;40\text{ MHz})$ (dashed line).

The algorithm for tuning an *N*-bit code $y(n)$, $0 \le n \le N-1$, into a new code $y'(n)$ is illustrated using the flow diagram shown in Fig. A.3. We define

$$d\left[y(n)\right] = \left\| \left[y(t;f_s) - x(t)\right] \otimes h_t(t) \right\|, \tag{A.12}$$

where $\|\cdot\|$ denotes the L^2 norm; then $d\left[y(n)\right]$ is a measure of the similarity between $y(t;f_s)$ and $x(t)$. If $y(n)$ is tuned into a code $y_{\text{temp},1}(n)$ such that $d\left[y_{\text{temp},1}(n)\right] < d\left[y(n)\right]$, $y_{\text{temp},1}(n)$ is considered better than $y(n)$ and will be the current candidate for the final code $y'(n)$. If a code $y_{\text{temp},2}(n)$ generated by tuning $y_{\text{temp},1}(n)$ satisfies $d\left[y_{\text{temp},2}(n)\right] < d\left[y_{\text{temp},1}(n)\right]$, $y_{\text{temp},2}(n)$ will become the new

candidate for $y'(n)$. The process continues until the candidate code cannot be further updated. In this algorithm, any new candidate for $y'(n)$ is different from the current candidate in at most N_2 ($N_2 = 16$ in this Appendix) consecutive bits, and the start index of the 16 bits is shifted sequentially and iteratively until the similarity to $x(n)$ cannot be further improved.

Fig. A.4(a)–(c) show $x(t) \otimes h_t(t)$, $y(t;40\,\text{MHz}) \otimes h_t(t)$, and $y'(t;40\,\text{MHz}) \otimes h_t(t)$, respectively. The parameters are the same as those used in Section A.2.3. Fig. A.4(d) shows the normalized envelopes of $x_c(t)$ (solid line), $y_c(t;40\,\text{MHz})$ (dotted line), and $y'_c(t;40\,\text{MHz})$ (dashed line). Fig. A.4 demonstrates that tuning a code can significantly improve the compression performance.

A.3 Design of the compression filter

This section presents the design principles of the compression filter. In this study, pulse compression is realized at baseband.

A.3.1 Design criterion

Assume that the digitized echo signal is

$$y'_{\text{rf}}(n) = \left[y'(t; f_s) \otimes h_t(t) \otimes h_t(t) \right]_{t=n/f_{s,\text{ADC}}}, \tag{A.13}$$

where $f_{s,\text{ADC}}$ is the sampling rate of the analog-to-digital converter (ADC) at the receiver. The $y'_{\text{rf}}(n)$ is demodulated into a baseband signal

$$y'_{\text{bb}}(n) = h_K(n) \otimes \left[y'_{\text{rf}}(n) \cdot \exp\left(-j2\pi f_0 n / f_{s,\text{ADC}} \right) \right], \tag{A.14}$$

where $h_K(n)$ is a Kaiser-windowed finite impulse response low-pass filter [65], i.e.,

$$h_K(n) = \frac{\sin 2\pi f_c (n - M/2)}{\pi (n - M/2)} \frac{I_0\left\{ \beta \left(1 - \left[(n - M/2)/(M/2) \right]^2 \right)^{1/2} \right\}}{I_0(\beta)}, 0 \le n \le M, \tag{A.15}$$

where $I_0(\cdot)$ represents the zeroth-order modified Bessel function of the first kind, f_c is the -6 dB cutoff frequency, $(M+1)$ is the filter length, and β is a shape

parameter. The $y'_{\mathrm{bb}}[n]$ is then D times downsampled to obtain

$$y'_{\mathrm{d}}(n) = y'_{\mathrm{bb}}(Dn)\,. \tag{A.16}$$

Given a compression filter $h_{\mathrm{d,c}}(n)$, the compressed signal is

$$y'_{\mathrm{d,c}}(n) = y'_{\mathrm{d}}(n) \otimes h_{\mathrm{d,c}}(n)\,. \tag{A.17}$$

Let $n_{\mathrm{d}}(n)$ and $n_{\mathrm{d,c}}(n)$ denote the noise after downsampling and compression, respectively, and define the autocorrelation function of a random process $s(n)$ as

$$R_s(k) = E\left\{s(n)s^*(n-k)\right\}, \tag{A.18}$$

where the asterisk denotes complex conjugation and E denotes the statistical expectation operator; then [66]

$$R_{n_{\mathrm{d,c}}}(k) = R_{n_{\mathrm{d}}}(k) \otimes h_{\mathrm{d,c}}(k) \otimes h^*_{\mathrm{d,c}}(-k) \tag{A.19}$$

and the ensemble-averaged noise power after pulse compression is $R_{n_{\mathrm{d,c}}}(0)$. If the peak of the compressed signal is normalized to unity by scaling the filter coefficients, the inverse of $R_{n_{\mathrm{d,c}}}(0)$ is the output SNR.

Given a filter length N_{f}, let m denote the index of the peak position of $y'_{\mathrm{d,c}}(n)$, I_{sl} denote the index set of the sidelobes, s specify the predetermined allowable PSL, and $s_{\mathrm{dB}} = 20\log s$. The goal is to find a compression filter $h'_{\mathrm{o}}(n)$ such that $R_{n_{\mathrm{d,c}}}(0)$ is minimized under the constraints of $y'_{\mathrm{d,c}}(m) = 1$ and $\left|y'_{\mathrm{d,c}}(n)\right| \le s$ for $n \in I_{\mathrm{sl}}$ [i.e., $h'_{\mathrm{o}}(n)$ maximizes the output SNR while maintaining the axial resolution and dynamic range specified by I_{sl} and s, respectively]. Unfortunately, this problem cannot be solved systematically, so the above formulation is slightly modified to the following: find the optimal compression filter $h_{\mathrm{o}}(n)$

resulting in the minimal $R_{n_{\mathrm{d,c}}}(0)$ under the constraints of $y'_{\mathrm{d,c}}(m)=1$, and $\left|\mathrm{Re}\left\{y'_{\mathrm{d,c}}(n)\right\}\right|$, $\left|\mathrm{Im}\left\{y'_{\mathrm{d,c}}(n)\right\}\right| \le s/\sqrt{2}$ for $n \in I_{\mathrm{sl}}$, where $\mathrm{Re}\{\cdot\}$ and $\mathrm{Im}\{\cdot\}$ denote the real part and the imaginary part, respectively. That is,

$$h_{\mathrm{o}}(n) = \arg\min_{h_{\mathrm{d,c}}} R_{n_{\mathrm{d,c}}}(0) \quad \text{subject to} \begin{cases} y'_{\mathrm{d,c}}(m)=1 \\ \left|\mathrm{Re}\left\{y'_{\mathrm{d,c}}(n)\right\}\right| \le s/\sqrt{2} \quad \text{for } n \in I_{\mathrm{sl}} \\ \left|\mathrm{Im}\left\{y'_{\mathrm{d,c}}(n)\right\}\right| \le s/\sqrt{2} \quad \text{for } n \in I_{\mathrm{sl}} \end{cases}. \tag{A.20}$$

A.3.2 Formulation for finding the optimal compression filter

Given a filter length of N_{f} [i.e., $h_{\mathrm{d,c}}(n)$ is nonzero only for $0 \le n \le N_{\mathrm{f}}-1$], then

$$\begin{aligned} R_{n_{\mathrm{d,c}}}(0) &= \sum_{q=0}^{N_{\mathrm{f}}-1}\sum_{p=0}^{N_{\mathrm{f}}-1} R_{n_{\mathrm{d}}}(-p+q)h_{\mathrm{d,c}}(p)h^{*}_{\mathrm{d,c}}(q) \\ &= \mathbf{h}^{\mathrm{H}}\mathbf{H}\mathbf{h} \end{aligned}, \tag{A.21}$$

where

$$\mathbf{h} \equiv \left[h_{\mathrm{d,c}}(0) \quad h_{\mathrm{d,c}}(1) \quad \cdots \quad h_{\mathrm{d,c}}(N_{\mathrm{f}}-1)\right]^{\mathrm{T}}, \tag{A.22}$$

$\mathbf{H}$ is an $N_{\mathrm{f}} \times N_{\mathrm{f}}$ Hermitian matrix (i.e., $\mathbf{H}=\mathbf{H}^{\mathrm{H}}$) and

$$\left(\mathbf{H}\right)_{pq} \equiv R_{n_{\mathrm{d}}}(p-q), \tag{A.23}$$

T denotes transpose, and H denotes the Hermitian (i.e., conjugate transpose). Because

$$\mathbf{h}^{\mathrm{H}}\mathbf{H}\mathbf{h} = \left(\mathbf{h}^{\mathrm{H}}\mathbf{H}\mathbf{h}\right)^{\mathrm{H}} = \left(\mathbf{h}^{\mathrm{H}}\mathbf{H}\mathbf{h}\right)^{*}, \tag{A.24}$$

$\mathrm{Im}\left\{\mathbf{h}^{\mathrm{H}}\mathbf{H}\mathbf{h}\right\}=0$ and

$$\mathbf{h}^{\mathrm{H}}\mathbf{H}\mathbf{h} = \left(\mathbf{h}^{\mathrm{H}}\mathbf{H}\mathbf{h}\right)^{\mathrm{T}}. \tag{A.25}$$

Let $\mathrm{Re}\{\mathbf{H}\} \equiv \mathbf{H}_{\mathrm{r}}$, $\mathrm{Im}\{\mathbf{H}\} \equiv \mathbf{H}_{\mathrm{i}}$, $\mathrm{Re}\{\mathbf{h}\} \equiv \mathbf{h}_{\mathrm{r}}$, $\mathrm{Im}\{\mathbf{h}\} \equiv \mathbf{h}_{\mathrm{i}}$, $\mathrm{Re}\left\{y'_{\mathrm{d}}(k)\right\} \equiv y_{\mathrm{r}}(k)$,

$\mathrm{Im}\{y'_{\mathrm{d}}(k)\} \equiv y_{\mathrm{i}}(k)$, and $j \equiv \sqrt{-1}$, then

$$
\begin{aligned}
\mathbf{h}^{\mathrm{H}}\mathbf{H}\mathbf{h} &= \mathbf{h}_{\mathrm{r}}^{\mathrm{T}}\mathbf{H}\mathbf{h}_{\mathrm{r}} + \mathbf{h}_{\mathrm{i}}^{\mathrm{T}}(-j\mathbf{H})\mathbf{h}_{\mathrm{r}} + \mathbf{h}_{\mathrm{r}}^{\mathrm{T}}(j\mathbf{H})\mathbf{h}_{\mathrm{i}} + \mathbf{h}_{\mathrm{i}}^{\mathrm{T}}\mathbf{H}\mathbf{h}_{\mathrm{i}} \\
&= \begin{bmatrix}\mathbf{h}_{\mathrm{r}}\\ \mathbf{h}_{\mathrm{i}}\end{bmatrix}^{\mathrm{T}}\begin{bmatrix}\mathbf{H} & j\mathbf{H}\\ -j\mathbf{H} & \mathbf{H}\end{bmatrix}\begin{bmatrix}\mathbf{h}_{\mathrm{r}}\\ \mathbf{h}_{\mathrm{i}}\end{bmatrix} = \left(\begin{bmatrix}\mathbf{h}_{\mathrm{r}}\\ \mathbf{h}_{\mathrm{i}}\end{bmatrix}^{\mathrm{T}}\begin{bmatrix}\mathbf{H} & j\mathbf{H}\\ -j\mathbf{H} & \mathbf{H}\end{bmatrix}\begin{bmatrix}\mathbf{h}_{\mathrm{r}}\\ \mathbf{h}_{\mathrm{i}}\end{bmatrix}\right)^{\mathrm{T}} \\
&= \begin{bmatrix}\mathbf{h}_{\mathrm{r}}\\ \mathbf{h}_{\mathrm{i}}\end{bmatrix}^{\mathrm{T}}\begin{bmatrix}\mathbf{H}^{\mathrm{T}} & -j\mathbf{H}^{\mathrm{T}}\\ j\mathbf{H}^{\mathrm{T}} & \mathbf{H}^{\mathrm{T}}\end{bmatrix}\begin{bmatrix}\mathbf{h}_{\mathrm{r}}\\ \mathbf{h}_{\mathrm{i}}\end{bmatrix} \\
&= \begin{bmatrix}\mathbf{h}_{\mathrm{r}}\\ \mathbf{h}_{\mathrm{i}}\end{bmatrix}^{\mathrm{T}}\begin{bmatrix}(\mathbf{H}+\mathbf{H}^{\mathrm{T}})/2 & j(\mathbf{H}-\mathbf{H}^{\mathrm{T}})/2\\ -j(\mathbf{H}-\mathbf{H}^{\mathrm{T}})/2 & (\mathbf{H}+\mathbf{H}^{\mathrm{T}})/2\end{bmatrix}\begin{bmatrix}\mathbf{h}_{\mathrm{r}}\\ \mathbf{h}_{\mathrm{i}}\end{bmatrix} \\
&= \begin{bmatrix}\mathbf{h}_{\mathrm{r}}\\ \mathbf{h}_{\mathrm{i}}\end{bmatrix}^{\mathrm{T}}\begin{bmatrix}\mathbf{H}_{\mathrm{r}} & -\mathbf{H}_{\mathrm{i}}\\ \mathbf{H}_{\mathrm{i}} & \mathbf{H}_{\mathrm{r}}\end{bmatrix}\begin{bmatrix}\mathbf{h}_{\mathrm{r}}\\ \mathbf{h}_{\mathrm{i}}\end{bmatrix} \\
&\equiv \mathbf{g}^{\mathrm{T}}\mathbf{G}\mathbf{g}
\end{aligned}
\tag{A.26}
$$

and

$$
y'_{\mathrm{d,c}}(n) = \sum_{p=0}^{N_{\mathrm{f}}-1} h_{\mathrm{d,c}}(p)\, y'_{\mathrm{d}}(n-p) = \mathbf{y}_{n,\mathrm{r}}^{\mathrm{T}}\mathbf{g} + j\mathbf{y}_{n,\mathrm{i}}^{\mathrm{T}}\mathbf{g}, \tag{A.27}
$$

where

$$
\mathbf{g} = \begin{bmatrix}\mathbf{h}_{\mathrm{r}}\\ \mathbf{h}_{\mathrm{i}}\end{bmatrix}, \tag{A.28}
$$

$$
\mathbf{G} = \begin{bmatrix}\mathbf{H}_{\mathrm{r}} & -\mathbf{H}_{\mathrm{i}}\\ \mathbf{H}_{\mathrm{i}} & \mathbf{H}_{\mathrm{r}}\end{bmatrix}, \tag{A.29}
$$

$$
\mathbf{y}_{n,\mathrm{r}} = \begin{bmatrix} y_{\mathrm{r}}(n) & y_{\mathrm{r}}(n-1) & \cdots & y_{\mathrm{r}}(n-N_{\mathrm{f}}+1) & -y_{\mathrm{i}}(n) & -y_{\mathrm{i}}(n-1) & \cdots & -y_{\mathrm{i}}(n-N_{\mathrm{f}}+1)\end{bmatrix}^{\mathrm{T}}
$$

, (A.30)

and

$$
\mathbf{y}_{n,\mathrm{i}} = \begin{bmatrix} y_{\mathrm{i}}(n) & y_{\mathrm{i}}(n-1) & \cdots & y_{\mathrm{i}}(n-N_{\mathrm{f}}+1) & y_{\mathrm{r}}(n) & y_{\mathrm{r}}(n-1) & \cdots & y_{\mathrm{r}}(n-N_{\mathrm{f}}+1)\end{bmatrix}^{\mathrm{T}}.
$$

(A.31)

Thus the constraint $y'_{\mathrm{d,c}}(m)=1$ can be formulated as

$$\mathbf{y}_{m,\mathrm{r}}^{\mathrm{T}}\mathbf{g}=1 \text{ and } \mathbf{y}_{m,\mathrm{i}}^{\mathrm{T}}\mathbf{g}=0, \tag{A.32}$$

and $\left|\mathrm{Re}\left\{y'_{\mathrm{d,c}}(n)\right\}\right|\le s/\sqrt{2}$ and $\left|\mathrm{Im}\left\{y'_{\mathrm{d,c}}(n)\right\}\right|\le s/\sqrt{2}$ can be formulated as

$$\mathbf{y}_{n,\mathrm{r}}^{\mathrm{T}}\mathbf{g}\le\frac{s}{\sqrt{2}},\ \left(-\mathbf{y}_{n,\mathrm{r}}\right)^{\mathrm{T}}\mathbf{g}\le\frac{s}{\sqrt{2}},\ \mathbf{y}_{n,\mathrm{i}}^{\mathrm{T}}\mathbf{g}\le\frac{s}{\sqrt{2}},\ \text{and}\ \left(-\mathbf{y}_{n,\mathrm{i}}\right)^{\mathrm{T}}\mathbf{g}\le\frac{s}{\sqrt{2}}. \tag{A.33}$$

(A.21), (A.26), (A.32) and (A.33) show that (A.20) is a quadratic programming problem with a convex feasible set [67]. Furthermore, $\mathbf{G}$ is positive definite (i.e., $\mathbf{g}^{\mathrm{T}}\mathbf{G}\mathbf{g}>0$ for all $\mathbf{g}$ nonzero) since $\mathbf{g}^{\mathrm{T}}\mathbf{G}\mathbf{g}=R_{n_{\mathrm{d,c}}}(0)$. Therefore, if the constraints can be satisfied using a filter length of N_{f}, the optimal compression filter $h_{\mathrm{o}}(n)$ of this length exists, is unique, and can be found [67].

A.4 Performance of the proposed method

In this section, the method introduced in Section A.2 is applied and compared with the pseudochirp approach proposed in [43]. The pseudochirp is the binary version of the original chirp signal which can also be implemented using a bipolar square wave pulser. All codes operate at a sampling frequency (or bit rate) of 40 MHz. The mainlobe is defined as the central nine points of the compressed signal, with the rest of the signal being defined as the sidelobe region.

A.4.1 Simulation results

In the simulations, the additive noise sampled by the ADC was assumed to be a white noise $n_{\mathrm{w}}(n)$ with a variance of σ_{w}^2. Therefore,

$$n_{\mathrm{d}}(n)=\left\{h_{\mathrm{K}}(l)\otimes\left[n_{\mathrm{w}}(l)\cdot\exp\left(-j2\pi f_0 l/f_{\mathrm{s,ADC}}\right)\right]\right\}_{l=Dn} \tag{A.34}$$

and

$$
\begin{aligned}
R_{n_{\mathrm{d}}}(k) &= E\Bigg\{\sum_{p} h_{\mathrm{K}}(p) n_{\mathrm{w}}(Dn-p)\exp\left[-j2\pi f_0 (Dn-p)/f_{\mathrm{s,ADC}}\right]\cdot \\
&\qquad \sum_{q} h_{\mathrm{K}}^{*}(q) n_{\mathrm{w}}^{*}(Dn-Dk-q)\exp\left[j2\pi f_0 (Dn-Dk-q)/f_{\mathrm{s,ADC}}\right]\Bigg\} \\
&= \sum_{p,q} h_{\mathrm{K}}(p) h_{\mathrm{K}}^{*}(q)\exp\left[-j2\pi f_0 (Dk-p+q)/f_{\mathrm{s,ADC}}\right]\cdot \\
&\qquad E\left\{n_{\mathrm{w}}(Dn-p) n_{\mathrm{w}}^{*}(Dn-Dk-q)\right\} \\
&= \sum_{p,q} h_{\mathrm{K}}(p) h_{\mathrm{K}}^{*}(q)\exp\left[-j2\pi f_0 (Dk-p+q)/f_{\mathrm{s,ADC}}\right] R_{n_{\mathrm{w}}}(Dk-p+q) \\
&= \sigma_{\mathrm{w}}^2 \sum_{q} h_{\mathrm{K}}(Dk+q) h_{\mathrm{K}}^{*}(q) = \sigma_{\mathrm{w}}^2 \cdot \left[h_{\mathrm{K}}(l) \otimes h_{\mathrm{K}}^{*}(-l)\right]_{l=Dk}
\end{aligned}
\quad . \text{(A.35)}
$$

Note that $R_{n_{\mathrm{w}}}(k) = \sigma_{\mathrm{w}}^2 \delta(k)$, where $\delta(k)$ is a discrete-time impulse [65].

A chirp $x_{\mathrm{cp}}(n)$ with a duration of T and a sampling frequency of f_{s} can be defined as

$$
x_{\mathrm{cp}}(n) = \sin\left\{2\pi\left[\left(f_0 - \frac{\Delta f}{2}\right)\frac{n}{f_{\mathrm{s}}} + \frac{\alpha}{2}\left(\frac{n}{f_{\mathrm{s}}}\right)^2\right]\right\},\ 0 \le n \le N-1, \tag{A.36}
$$

where $N = f_{\mathrm{s}} T$, and its corresponding pseudochirp $z_{\mathrm{pc}}(n)$ is defined by

$$
z_{\mathrm{pc}}(n) = \begin{cases} 1 \text{ if } x_{\mathrm{cp}}(n) \ge 0 \\ -1 \text{ otherwise} \end{cases}. \tag{A.37}
$$

The following pseudochirp signal was used to evaluate its performance in SNR enhancement:

$$
z_{\mathrm{pc}}(t; f_{\mathrm{s}}) = \sum_{n} z_{\mathrm{pc}}(n)\Pi\left(f_{\mathrm{s}} t - n\right). \tag{A.38}
$$

The transducer was assumed to have a Gaussian frequency response with a center frequency of 2.5 MHz and a –6 dB bandwidth of 1.5 MHz. The other parameters were $f_{\mathrm{s,ADC}} = 20\,\mathrm{MHz}$, $M = 18$, $\beta = 3.7$, $f_{\mathrm{c}} = 0.1125$, $D = 5$ (i.e., corresponding to a sampling rate after downsampling, $f_{\mathrm{s,d}}$, of 4 MHz), $\sigma_{\mathrm{w}}^2 = 1$, $f_0 = 2.5\,\mathrm{MHz}$, and

$\Delta f = 1.5\,\text{MHz}$. Fig. A.5(a) shows the downsampled baseband signal $z_{\text{pc,d}}(n)$ for $T = 12\,\mu\text{s}$ (dashed line) and the compressed signal $z_{\text{pc,d,c}}(n)$ corresponding to $N_{\text{f}} = 64$ and $s_{\text{dB}} =$ –40 dB (solid line). The optimal SNR, which corresponds to the minimal $R_{n_{\text{d,c}}}(0)$ in (A.20), is 15.0 dB. Fig. A.5(b) is a plot of the optimal SNR versus N_{f} corresponding to $s_{\text{dB}} =$ –40 dB and $T = 12\,\mu\text{s}$. The figure shows that the optimal SNR increases with N_{f}.

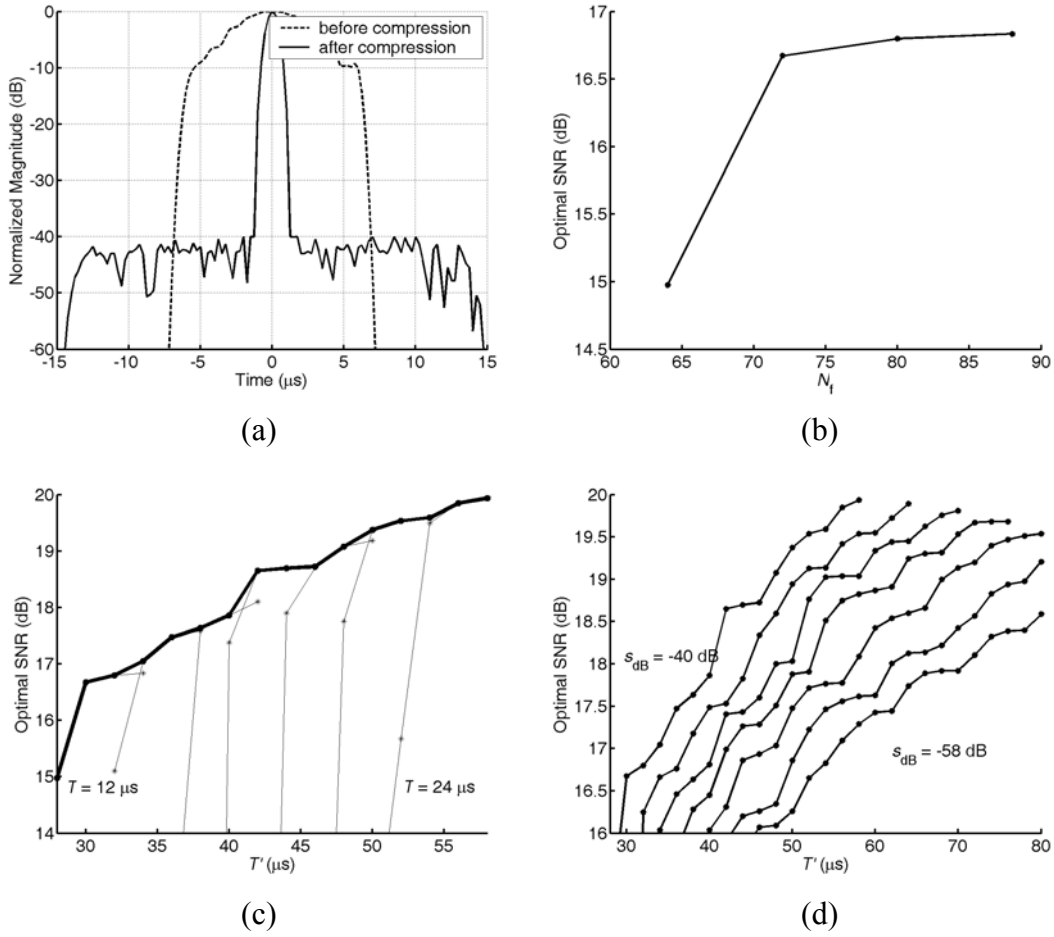

Fig. A.5. (a) The demodulated and downsampled pseudochirp with T = 12 μs (dashed line) and the compressed signal corresponding to $N_{\text{f}} = 64$ and $s_{\text{dB}} =$ –40 dB (solid line). (b) The curve of optimal SNR versus N_{f} corresponding to $s_{\text{dB}} =$ –40 dB for the pseudochirp with T = 12 μs. (c) The curves of optimal SNR versus T' corresponding to $s_{\text{dB}} =$ –40 dB for the pseudochirps with T = 12 μs to 24 μs with a step of 2 μs. The characteristic curve of the pseudochirp corresponding to $s_{\text{dB}} =$ –40 dB is also shown here as a thick solid line. (d) The characteristic curves of pseudochirps corresponding to $s_{\text{dB}} =$ –40 dB to –58 dB with a step of –3 dB.

Define $T' = \left(T + N_{\mathrm{f}} / f_{\mathrm{s,d}}\right)$ as the total temporal duration of the compressed signal. The performance of a code is determined by the optimal SNR, assuming T' and s_{dB} are fixed. Plots of the optimal SNR versus T' corresponding to s_{dB} = –40 dB and $T = 12\,\mu\mathrm{s}$ to $24\,\mu\mathrm{s}$ with a step of $2\,\mu\mathrm{s}$ are shown in Fig. A.5(c) for the pseudochirps. At a given T', the maximum of the optimal SNRs corresponding to various T values are found. A curve connecting such points is also shown in Fig. A.5(c) as a thick solid line. This curve is called the characteristic curve of the pseudochirp at s_{dB} = –40 dB. In this format, a code with a (vertically) higher curve outperforms a code with a lower curve. Seven characteristic curves of pseudochirps corresponding to s_{dB} = –40 dB to –58 dB with a step of –3 dB are shown in Fig. A.5(d). These curves were subsequently used to evaluate the performance of the binary Tukey-windowed chirps.

Tukey-windowed chirps [defined in (A.7) and denoted by $x_{\mathrm{Tc}}(t;T)$] were converted into binary Tukey-windowed chirps [denoted by $y'_{\mathrm{bTc}}(n;T)$] using the method presented in Section A.2. All Tukey-windowed chirps had $f_0 = 2.5\,\mathrm{MHz}$, $\Delta f = 1.625\,\mathrm{MHz}$, and a taper ratio of 0.15. With these settings, the –12 dB bandwidths of a Tukey-windowed chirp and a pseudochirp with $f_0 = 2.5\,\mathrm{MHz}$ and $\Delta f = 1.5\,\mathrm{MHz}$ are the same. Because $\left|x_{\mathrm{Tc}}(t;T)\right| \le 1$, overloading did not occur in the sigma-delta modulator. To make the transmitted peak acoustic power associated with the binary Tukey-windowed chirp the same as that associated with the pseudochirp, the transmitted signal was scaled according to

$$y''_{\mathrm{bTc}}(t;T) = \frac{4}{\pi} y'_{\mathrm{bTc}}(t;T). \tag{A.39}$$

The factor $4/\pi$ is the magnitude of the fundamental frequency of a periodic square wave with an amplitude of 1. Other parameters were $f_{\mathrm{s,ADC}} = 20\,\mathrm{MHz}$, $M = 18$, $\beta = 3.7$, $f_{\mathrm{c}} = 0.1125$, $D = 5$, and $\sigma_{\mathrm{w}}^2 = 1$.

Fig. A.6(a)–(h) are plots of the optimal SNR versus T' for binary Tukey-windowed chirps corresponding to s_{dB} = –40 dB to –61 dB with a step of –3 dB, respectively. In each figure panel, the curves corresponding to three binary Tukey-windowed chirps are shown as thick solid lines from top to bottom: $y'_{\mathrm{bTc}}(n; 24\,\mu\mathrm{s})$, $y'_{\mathrm{bTc}}(n; 20\,\mu\mathrm{s})$, and $y'_{\mathrm{bTc}}(n; 16\,\mu\mathrm{s})$. Each panel of the figure includes

the characteristic curves of pseudochirps for comparison. The characteristic curve corresponding to the same PSL is shown as a thick dashed line, and the others are shown as thin solid lines. Fig. A.6 shows that using a binary Tukey-windowed chirp improves the SNR by up to 2 dB relative to using a pseudochirp given an s_{dB} and a T' since, given an s_{dB}, the turning-point positions (which represent more efficient code/filter combinations) in the curves for binary Tukey-windowed chirps are generally 1–2 dB higher than the characteristic curves of pseudochirps. Taking a 1-dB SNR improvement as an example, this means that using a binary Tukey-windowed chirp instead of a pseudochirp results in a $\left(1-10^{-1/10}\right)\cdot 100\% = 20.6\%$ reduction in code duration and dead zone because the SNR improvement is approximately proportional to the code duration. Moreover, comparing the turning-point positions in the curves for binary Tukey-windowed chirps with respect to the characteristic curves of pseudochirps shows that using a binary Tukey-windowed chirp in general results in a PSL that is 6 dB lower than that when using a pseudochirp. Fig. A.6(h) shows that $y'_{\mathrm{bTc}}(n; 24\,\mu\mathrm{s})$ performs worse than $y'_{\mathrm{bTc}}(n; 20\,\mu\mathrm{s})$ and $y'_{\mathrm{bTc}}(n; 16\,\mu\mathrm{s})$ at a lower s_{dB} level. This may reflect that the code-tuning algorithm finds a better code than the original code $y_{\mathrm{bTc}}(n; 24\,\mu\mathrm{s})$, rather than the best code.

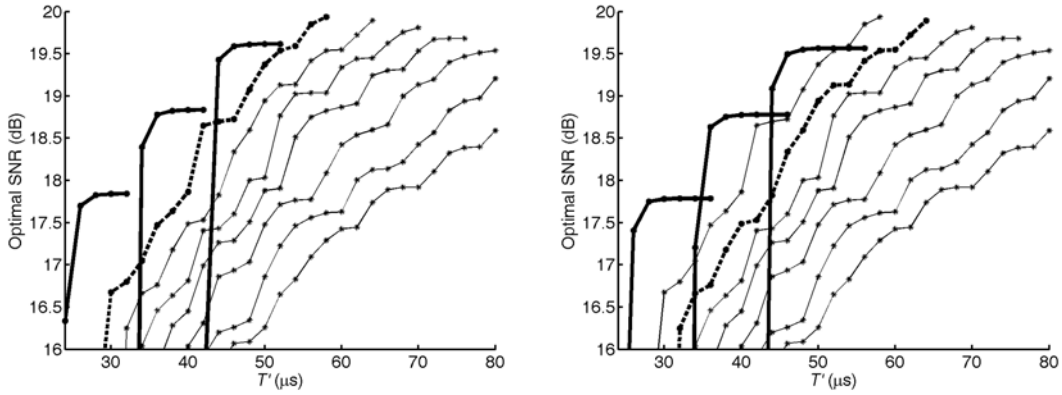

Fig. A.6. The curves of optimal SNR versus T' for binary Tukey-windowed chirps generated by simulations. (a) s_{dB} = –40 dB. (b) s_{dB} = –43 dB. (c) s_{dB} = –46 dB. (d) s_{dB} = –49 dB. (e) s_{dB} = –52 dB. (f) s_{dB} = –55 dB. (g) s_{dB} = –58 dB. (h) s_{dB} = –61 dB. In each panel, the curves corresponding to three binary Tukey-windowed chirps are shown from top to bottom as thick solid lines: $y'_{\mathrm{bTc}}(n; 24\,\mu\mathrm{s})$, $y'_{\mathrm{bTc}}(n; 20\,\mu\mathrm{s})$, and $y'_{\mathrm{bTc}}(n; 16\,\mu\mathrm{s})$. Also shown in each panel are the characteristic curves of pseudochirps for comparison. The characteristic curve corresponding to the same PSL is shown as a thick dashed line; the others are shown as thin solid lines.

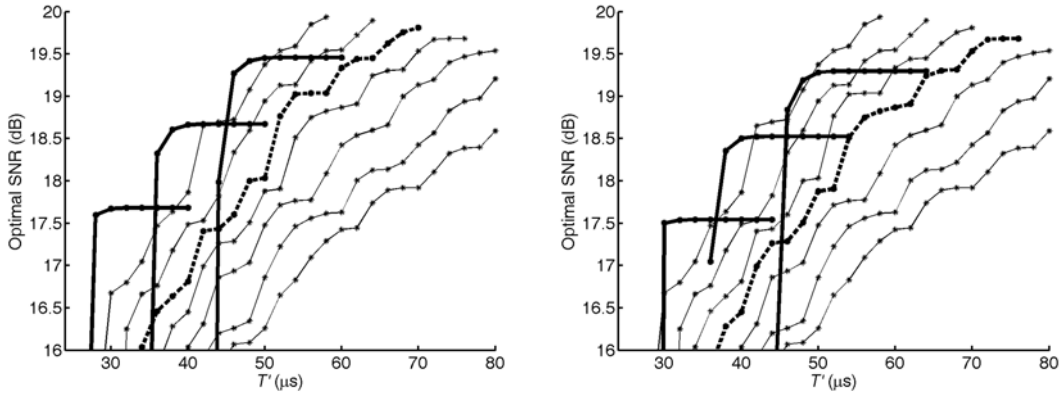

(c) (d)

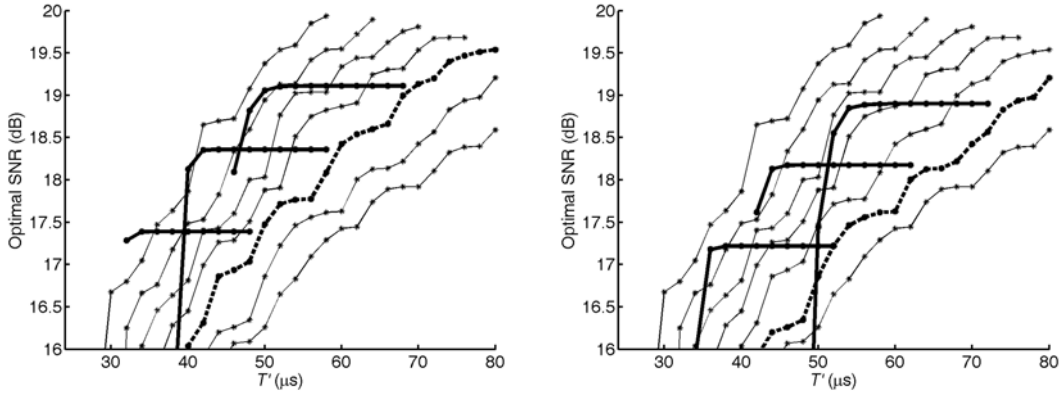

(e) (f)

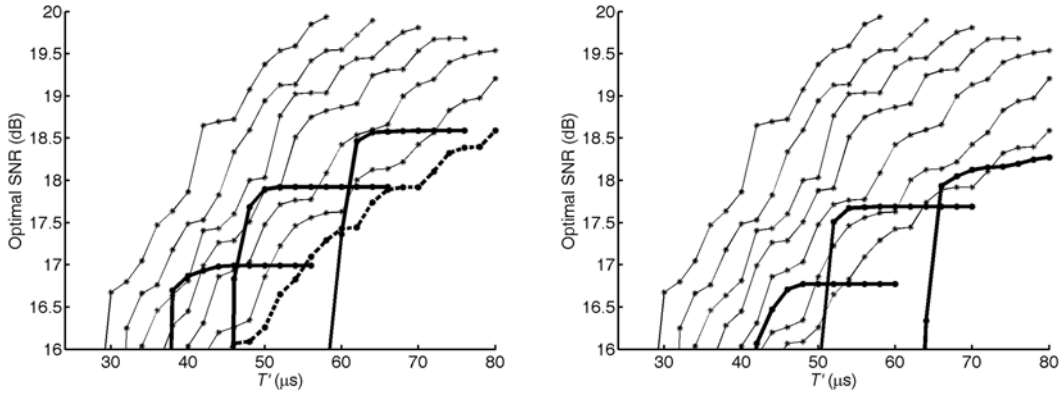

(g) (h)

Fig. A.6. (Continued.)

A.4.2 Experimental results

Fig. A.7 shows the experimental setup. A transducer with a diameter of 25.4 mm and a focal length of 71.1 mm (V304, Panametrics, Waltham, MA) was used to transmit and receive the ultrasonic signal. The image target was a nylon wire with a diameter of 0.2 mm placed 68.7 mm from the transducer. The pulse-echo signal from

the wire and its spectrum obtained by using a pulser/receiver (PR5800, Panametrics) to transmit and receive are shown in Fig. A.8(a) and (b), respectively. A waveform generator (DAC200, Signatec, Corona, CA) was used to generate the coded signal at a sampling rate of 200 MHz (i.e., there are five samples per bit) with an amplitude resolution of 12 bits. The pulser/receiver was used to provide a 60 dB gain to the echo signal. The amplified echo was then digitized by an ADC (PCI-9820, ADLINK, Taipei, Taiwan) at a sampling rate of 60 MHz (i.e., $f_{s,ADC} = 60\,\text{MHz}$) with an amplitude resolution of 14 bits. The transmit and receive timing was controlled by a function/arbitrary waveform generator (33120A, Agilent, Palo Alto, CA), which generated a 1-kHz trigger signal for the waveform generator and the ADC.

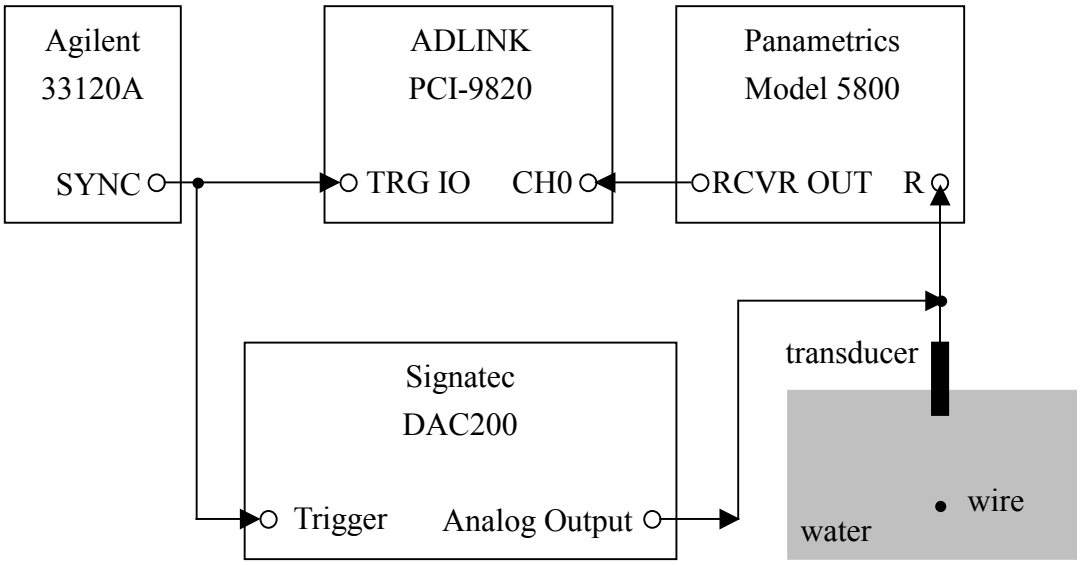

Fig. A.7. Block diagram of the experimental setup.

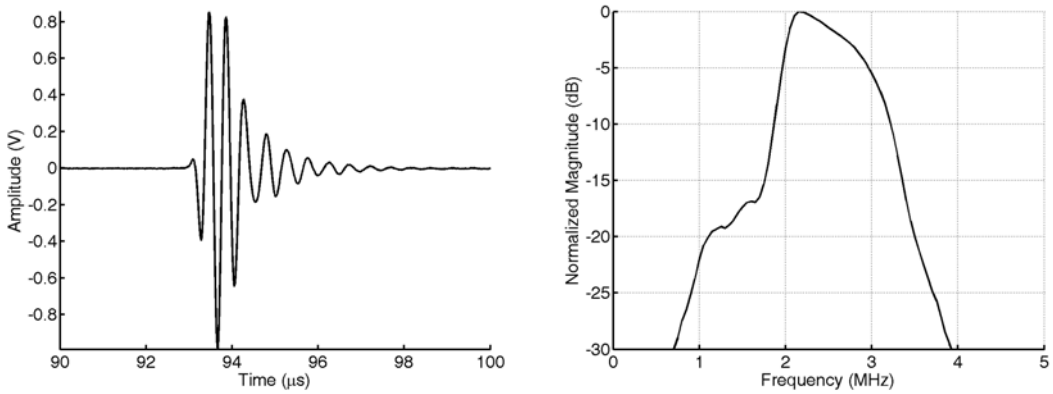

(a) (d)

Fig. A.8. (a) The pulse-echo signal and (b) the corresponding spectrum of the signal obtained from the wire using a pulser/receiver to transmit and receive.

Because the noise was not white in this setup, a dummy experiment was conducted in order to estimate $R_{n_\mathrm{d}}(k)$. A total of 4000 records were acquired at 16000 samples per record in the absence of a transmit signal. The parameters were $M = 54$, $\beta = 3.7$, $f_\mathrm{c} = 0.0375$, and $D = 15$ (i.e., $f_{\mathrm{s,d}} =$ 4 MHz). The $R_{n_\mathrm{d}}(k)$ was estimated from $n_\mathrm{d}(n)$ using the following equation [66]:

$$R_{n_\mathrm{d}}(k) = \frac{\sum_{n \in I_n} n_\mathrm{d}(n) n_\mathrm{d}^*(n-k)}{\sum_{n \in I_n} 1}, \tag{A.40}$$

where I_n is an index set. The power spectral density of $n_\mathrm{d}(n)$, obtained by taking the Fourier transform of $R_{n_\mathrm{d}}(k)$, is shown in Fig. A.9. Electromagnetic interference manifested as several spikes in the power spectral density in this setup. An experiment was also conducted using a one-cycle square wave with a duration of 0.4 μs and an amplitude of $\pi/4$ V as the transmitted signal. The SNR at baseband was 14.8 dB, and this value was used as a reference in the subsequent experiments.

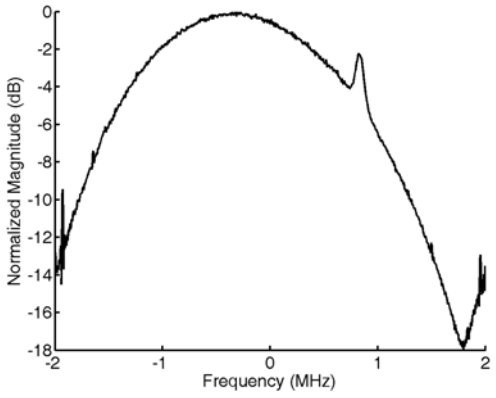

Fig. A.9. The measured power spectral density of $n_\mathrm{d}(n)$.

The codes (seven pseudochirps and three binary Tukey-windowed chirps) evaluated in Section A.4.1 were here evaluated experimentally. The transmitted signal levels were $\pm\pi/4$ V and ± 1 V for the pseudochirp and the binary Tukey-windowed chirp, respectively, in order to maintain a constant peak acoustic power for all cases. The echo signal ($y'_{\mathrm{bTc,d}}$ or $z_{\mathrm{pc,d}}$) from the wire was estimated using 16000 records to reduce noise and to design the compression filter. The output

SNR corresponding to each compression filter was estimated using $n_{\mathrm{d}}(n)$. The SNR improvement using coded excitation is defined as the output SNR using coded excitation minus 14.8 dB (i.e., the SNR reference). The thick solid lines in Fig. A.10(a)–(h) show the optimal improved SNR versus T' for binary Tukey-windowed chirps corresponding to $s_{\mathrm{dB}} =$ –40 dB to –61 dB with a step of –3 dB, respectively. In each panel of the figure, the curves corresponding to the three binary Tukey-windowed chirps, $y'_{\mathrm{bTc}}(n; 24\,\mu\mathrm{s})$, $y'_{\mathrm{bTc}}(n; 20\,\mu\mathrm{s})$, and $y'_{\mathrm{bTc}}(n; 16\,\mu\mathrm{s})$, are shown from top to bottom. Each figure panel also contains the characteristic curves of pseudochirps corresponding to $s_{\mathrm{dB}} =$ –40 dB to –58 dB with a step of –3 dB, for comparison. The characteristic curve corresponding to the same PSL is shown as a thick dashed line, and the others are shown as thin solid lines. The experimental results again show that using a binary Tukey-windowed chirp instead of a pseudochirp reduces the code duration by at least 20.6% or the PSL by 6 dB.

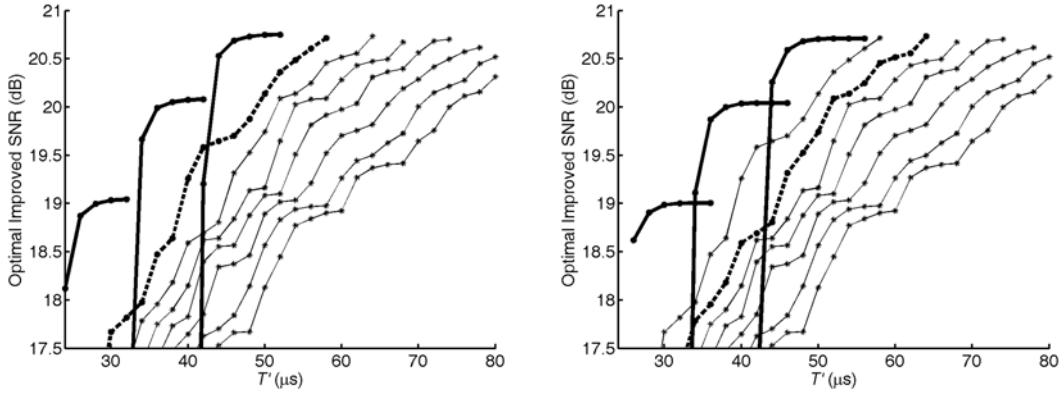

(a) (b)

Fig. A.10. The curves of optimal SNR versus T' for binary Tukey-windowed chirps obtained from experiments. (a) $s_{\mathrm{dB}} =$ –40 dB. (b) $s_{\mathrm{dB}} =$ –43 dB. (c) $s_{\mathrm{dB}} =$ –46 dB. (d) $s_{\mathrm{dB}} =$ –49 dB. (e) $s_{\mathrm{dB}} =$ –52 dB. (f) $s_{\mathrm{dB}} =$ –55 dB. (g) $s_{\mathrm{dB}} =$ –58 dB. (h) $s_{\mathrm{dB}} =$ –61 dB. In each panel, the curves corresponding to three binary Tukey-windowed chirps are shown from top to bottom as thick solid lines: $y'_{\mathrm{bTc}}(n; 24\,\mu\mathrm{s})$, $y'_{\mathrm{bTc}}(n; 20\,\mu\mathrm{s})$, and $y'_{\mathrm{bTc}}(n; 16\,\mu\mathrm{s})$. Also shown in each panel are the characteristic curves of pseudochirp corresponding to $s_{\mathrm{dB}} =$ –40 dB to –58 dB with a step of –3 dB for comparison. The characteristic curve corresponding to the same PSL is shown as a thick dashed line; the others are shown as thin solid lines.

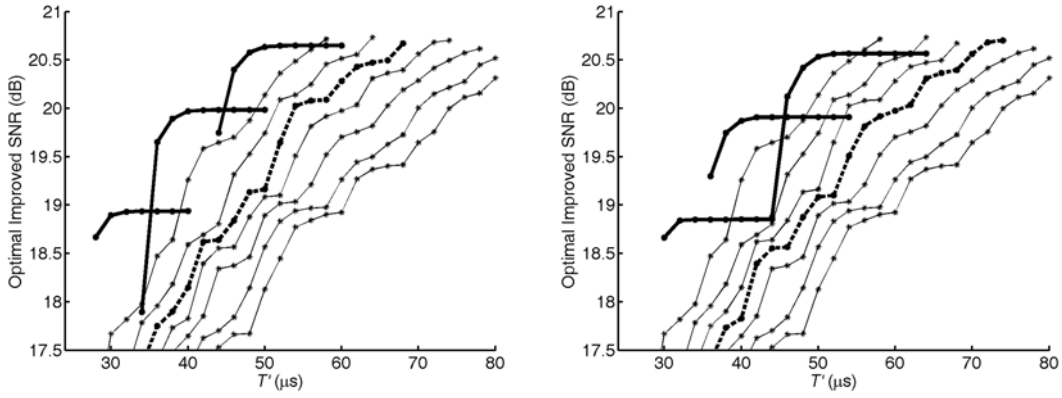

(c) (d)

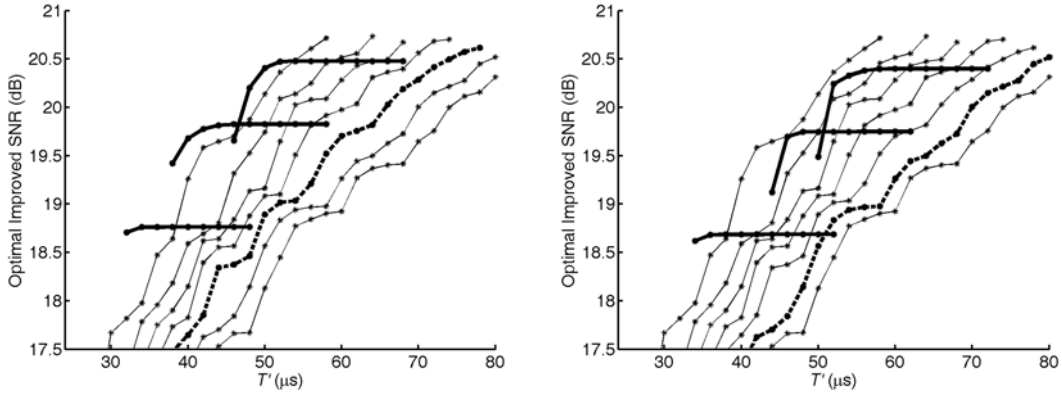

(e) (f)

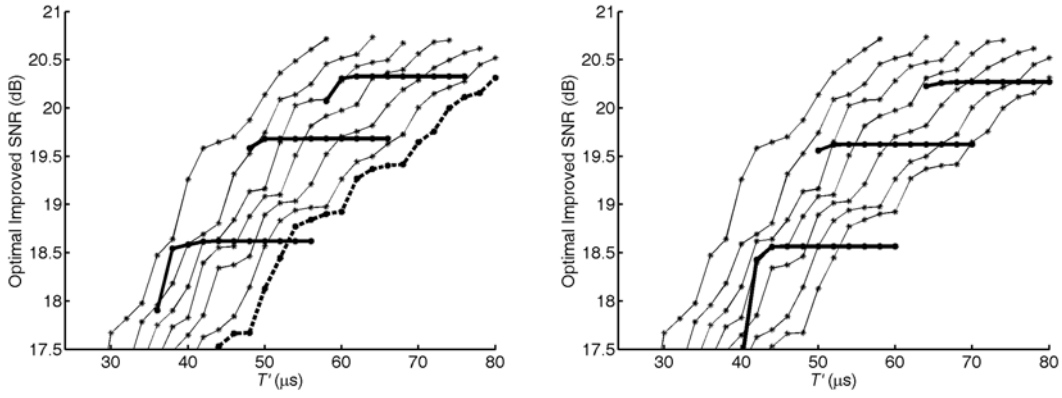

(g) (h)

Fig. A.10. (Continued.)

A.5 Discussion

The code-tuning algorithm introduced in Section A.2.4 does not guarantee the

smallest $\left\|\left[y'(t;f_s)-x(t)\right]\otimes h_t(t)\right\|$, since the compression performance could be improved by using other algorithms such as a genetic algorithm [68]. Furthermore, other metrics could be adopted for the error between the original nonbinary code and its corresponding binary code.

Let the bit duration be the inverse of the bit rate, the shortest time between any two consecutive transitions in the code is equal to the bit duration using the proposed method. One inherent restriction in this study is that a transition always occurs at an instant equal to an integral multiple of the bit duration. This restriction is not necessary and can be removed. For example, assume that the shortest switching time of the pulser is limited to 25 ns and that the clock rate of the system is 200 MHz, then the bit rate of the code can be set to 200 MHz instead of 40 MHz but the time between any two consecutive transitions is limited to be larger than or equal to five clock cycles in order not to violate the minimal switching time (25 ns). With this scheme, similarity between the original nonbinary code and its corresponding binary code will increase. This subject is currently under investigation.

The application of the proposed method for code conversion is not limited to SNR improvement. In [53], [54], the codes are used for special purposes (as mentioned in Section A.1), non-binary, and inflexible; the proposed method for code conversion can be applied to those cases to eliminate the need for arbitrary waveform generators. The selected error metric results in the fundamental component in the binary code dominating its similarity to the corresponding nonbinary code, and the signal integrity of higher harmonics is not controlled. Therefore, for cases in which the higher harmonics are desired [55]–[58], the applicability of the method must be further investigated.

A.6 Concluding remarks

This appendix proposes a method for exciting nonbinary codes using bipolar square wave pulsers. A nonbinary code is converted into a binary code by code translation and code tuning such that the desired waveform can be transmitted using a bipolar pulser. Tukey-windowed chirps were converted with different durations (16, 20, and 24 μs), all with a taper ratio of 0.15, a center frequency of 2.5 MHz, and an equivalent bandwidth of 1.5 MHz, into binary Tukey-windowed chirps that were compared with pseudochirps over the same spectral band. The bit rate was 40 MHz.

Simulation results showed that using a binary Tukey-windowed chirp instead of a pseudochirp reduces the code duration by 20.6% when the constraints on PSL and the SNR improvement are fixed. Moreover, using a binary Tukey-windowed chirp can in general lower the PSL by 6 dB relative to that when using a pseudochirp if the total duration and the SNR improvement are fixed. Experimental results under the same settings were in agreement with the simulations. Although the converted binary code is only an approximation of the original code after convolving with the impulse response of the transducer, the proposed method is successful at improving the SNR. With our method, the low-cost advantage of bipolar pulsers is preserved while the compression performance of the coded excitation system is enhanced in medical ultrasound. The proposed method for code conversion can also be used to eliminate the need for an arbitrary waveform generator in other applications, such as pulse inversion imaging [53] and dynamic transmit focusing [54].

References

[1] M. E. Lanfranchi, *Breast Ultrasound*. 2nd ed. New York: Marban Books, 2000.

[2] T. C. Telger, *Teaching Atlas of Breast Ultrasound*. New York: Thieme Medical Publishers, 1996.

[3] C.-M. Chen, Y.-H. Chou, K.-C. Han, G.-S. Hung, C.-M. Tiu, H.-J. Chiou, and S.-Y. Chiou, "Breast lesions on sonograms: Computer-aided diagnosis with nearly setting-independent features and artificial neural networks," *Radiology*, vol. 226, no. 2, pp. 504 – 514, 2003.

[4] A. T. Stavros, D. Thickman, C. L. Rapp, M. A. Dennis, S. H. Parker, and G. A. Sisney, "Solid breast nodules: Use of sonography to distinguish between benign and malignant lesions," *Radiology*, vol. 196, no.1, pp. 123–134, 1995.

[5] Q. Zhu and B. D. Steinberg, "Wavefront amplitude distortion and image sidelobe levels: Part I—Theory and computer simulations," *IEEE Trans. Ultrason., Ferroelect., Freq. Contr.*, vol. 40, no. 6, pp. 747–753, 1993.

[6] Q. Zhu, B. D. Steinberg, and R. L. Arenson, "Wavefront amplitude distortion and image sidelobe levels: Part II—*In vivo* experiments," *IEEE Trans. Ultrason., Ferroelect., Freq. Contr.*, vol. 40, no. 6, pp. 754–762, 1993.

[7] Q. Zhu and B. D. Steinberg, "Wavefront amplitude distribution in the female breast," *J. Acoust. Soc. Amer.*, vol. 96, no. 1, pp. 1–9, 1994.

[8] L. M. Hinkelman, D.-L. Liu, R. C. Waag, Q. Zhu, and B. D. Steinberg, "Measurements and correction of ultrasonic pulse distortion produced by the human breast," *J. Acoust. Soc. Amer.*, vol. 97, no. 3, pp. 1958–1969, 1995.

[9] R. C. Gauss, M. S. Soo, and G. E. Trahey, "Wavefront distortion measurements in the human breast," in *Proc. IEEE Ultrason. Symp.*, 1997, pp. 1547–1551.

[10] W.-C. Yeh, P.-C. Li, Y.-M. Jeng, H.-C. Hsu, P.-L. Kuo, M.-L. Li, P.-M. Yang, and P.-H. Lee, "Elastic modulus measurements of human liver and correlation with pathology," *Ultrasound Med. Biol.*, vol. 28, no. 4, pp. 467–474, 2002.

[11] B. S. Garra, E. I. Céspedes, J. Ophir, S. R. Spratt, R. A. Zuurbier, C. M. Magnant,

and M. F. Pennanen**,** “Elastography of breast lesions: Initial clinical results,” *Radiology*, vol. 202, no. 1, pp. 79–86, 1997.

[12] S. A. Goss, R. L. Johnston, and F. Dunn, “Comprehensive compilation of empirical ultrasonic properties of mammalian tissues,” *J. Acoust. Soc. Amer.*, vol. 64, no. 2, pp. 423–457, 1978.

[13] S. W. Flax and M. O’Donnell, “Phase-aberration correction using signals from point reflectors and diffuse scatterers: Basic principles,” *IEEE Trans. Ultrason., Ferroelect., Freq. Contr.*, vol. 35, no. 6, pp. 758–767, 1988.

[14] M. O’Donnell and S. W. Flax, “Phase-aberration correction using signals from point reflectors and diffuse scatterers: Measurements,” *IEEE Trans. Ultrason., Ferroelect., Freq. Contr.*, vol. 35, no. 6, pp. 768–774, 1988.

[15] D.-L. Liu and R. C. Waag, “Correction of ultrasonic wavefront distortion using backpropagation and a reference waveform method for time-shift compensation,” *J. Acoust. Soc. Amer.*, vol. 96, no. 2, pp. 649–660, 1994.

[16] G. C. Ng, S. S. Worrell, P. D. Freiburger, and G. E. Trahey, “A comparative evaluation of several algorithms for phase aberration correction,” *IEEE Trans. Ultrason., Ferroelect., Freq. Contr.*, vol. 41, no. 5, pp. 631–643, 1994.

[17] G. C. Ng, P. D. Freiburger, W. F. Walker, and G. E. Trahey, “A speckle target adaptive imaging technique in the presence of distributed aberrations,” *IEEE Trans. Ultrason., Ferroelect., Freq. Contr.*, vol. 44, no. 1, pp. 140–151, 1997.

[18] R. C. Gauss, G. E. Trahey, and M. S. Soo, “Adaptive imaging in the breast,” in *Proc. IEEE Ultrason. Symp.*, 1999, pp. 1563–1569.

[19] E. L. Madsen, J. A. Zagzebski, G. R. Frank, J. F. Greenleaf, and P. L. Carson, “Anthropomorphic breast phantoms for assessing ultrasonic imaging system performance and for training ultrasonographers: Part I,” *J. Clin. Ultrasound*, vol. 10, no. 2, pp. 67–75, 1982.

[20] S. A. Goss, R. L. Johnston, and F. Dunn, “Compilation of empirical ultrasonic properties of mammalian tissues. II,” *J. Acoust. Soc. Amer.*, vol. 68, no. 1, pp. 93–108, 1980.

[21] E. L. Madsen, E. Kelly-Fry, and G. R. Frank, “Anthropomorphic phantoms for assessing systems used in ultrasound imaging of the compressed breast,”

Ultrasound Med. Biol., vol. 14, sup. 1, pp. 183–201, 1988.

[22] A. C. Kak and M. Slaney, *Principles of Computerized Tomographic Imaging*. New York: Institute of Electrical and Electronics Engineers, 1988.

[23] S.-W. Huang and P.-C. Li, "Computed tomography sound velocity reconstruction using incomplete data," *IEEE Trans. Ultrason., Ferroelect., Freq. Contr.*, vol. 51, no. 3, pp. 329–342, 2004.

[24] S.-W. Huang and P.-C. Li, "Experimental investigation of computed tomography sound velocity reconstruction using incomplete data," *IEEE Trans. Ultrason., Ferroelect., Freq. Contr.*, accepted.

[25] M. Krueger, A. Pesavento, and H. Ermert, "A modified time-of-flight tomography concept for ultrasonic breast imaging," in *Proc. IEEE Ultrason. Symp.*, 1996, pp. 1381–1385.

[26] M. Krueger, V. Burow, K. M. Hiltawsky, and H. Ermert, "Limited angle ultrasonic transmission tomography of the compressed female breast," in *Proc. IEEE Ultrason. Symp.*, 1998, pp. 1345–1348.

[27] N. G. Chen, P. Y. Guo, S. K. Yan, D. Q. Piao, and Q. Zhu, "Simultaneous near-infrared diffusive light and ultrasound imaging," *Appl. Opt.*, vol. 40, no. 34, pp. 6367–6680, 2001.

[28] M. Huang, T. Xie, N. G. Chen, and Q. Zhu, "Simultaneous reconstruction of absorption and scattering maps with ultrasound localization: Feasibility study using transmission geometry," *Appl. Opt.*, vol. 42, no. 19, pp. 4102–4114, 2003.

[29] J. D. Bronzino, *The Biomedical Engineering Handbook*. 2nd ed. vol. 1, Boca Raton, FL: CRC Press, 2000.

[30] H. L. Royden, *Real Analysis*. 3rd ed. Englewood Cliffs, NJ: Prentice-Hall, 1988.

[31] H. Stark and Y. Yang, *Vector Space Projections: A Numerical Approach to Signal and Image Processing, Neural Nets, and Optics.* New York: Wiley, 1998.

[32] P. L. Combettes and P. Bondon, "Hard-constrained inconsistent signal feasibility problems," *IEEE Trans. Signal Processing*, vol. 47, no. 9, pp. 2460–2468, 1999.

[33] M. Tabei, T. D. Mast, and R. C. Waag, "A *k*-space method for coupled first-order acoustic propagation equations," *J. Acoust. Soc. Amer.*, vol. 111, no. 1, pp. 53–63,

2002.

[34] P. M. Morse and K. U. Ingard, *Theoretical Acoustics*. New York: McGraw-Hill, 1968.

[35] A. I. Nachman, J. F. Smith, and R. C. Waag, "An equation for acoustic propagation in inhomogeneous media with relaxation losses," *J. Acoust. Soc. Amer.*, vol. 88, no. 3, pp. 1584–1595, 1990.

[36] M. Frigo and S. G. Johnson, "FFTW: An adaptive software architecture for the FFT," in *Proc. ICASSP*, 1998, pp. 1381–1384.

[37] J. W. Goodman, *Introduction to Fourier Optics*. 2nd ed. New York: McGraw-Hill, 1996.

[38] P. Oskoui and H. Stark, "A comparative study of three reconstruction methods for a limited-view computer tomography problem," *IEEE Trans. Med. Imag.*, vol. 8, no. 1, pp. 43–49, 1989.

[39] K. C. Tam, J. W. Eberhard, and K. W. Mitchell, "Incomplete-data CT image reconstructions in industrial applications," *IEEE Trans. Nucl. Sci.,* vol. 37, no. 3, pp. 1490–1499, 1990.

[40] H. Stark, *Image Recovery: Theory and Application*. London: Academic, 1987.

[41] M. O'Donnell and S. D. Silverstein, "Optimal displacement for compound image generation in medical ultrasound," *IEEE Trans. Ultrason., Ferroelect., Freq. Contr.*, vol. 35, no. 4, pp. 470–476, 1988.

[42] R. C. Gonzalez and R. E. Woods, *Digital Image Processing*. 2nd ed. Reading, MA: Addison-Wesley, 2002.

[43] M. O'Donnell, "Coded excitation system for improving the penetration of real-time phased-array imaging systems," *IEEE Trans. Ultrason., Ferroelect., Freq. Contr.*, vol. 39, no. 3, pp. 341–351, 1992.

[44] R. M. Lemor, P. K. Weber, P. K. Fonfara, C. Guenther, H. J. Welsch, and M. L. Hoss, "A new combined open research platform for ultrasound radio frequency signal processing," in *Proc. IEEE Ultrason. Symp.*, 2003, pp. 33–37.

[45] M. E. Lyons and K. J. Parker, "Absorption and attenuation in soft tissues II—Experimental results," *IEEE Trans. Ultrason., Ferroelect., Freq. Contr.*, vol.

35, no. 4, pp. 511–521, 1988.

[46] F. J. Harris, “On the Use of Windows for Harmonic Analysis with the Discrete Fourier Transform,” *Proceedings of the IEEE*, vol. 66, no. 1, pp. 66–67, 1978.

[47] D.-L. Liu and R. C. Waag, “Propagation and backpropagation for ultrasonic wavefront design,” *IEEE Trans. Ultrason., Ferroelect., Freq. Contr.*, vol. 44, no. 1, pp. 1–13, 1997.

[48] P. T. Christopher and K. J. Parker, “New approaches to the linear propagation of acoustic fields,” *J. Acoust. Soc. Amer.*, vol. 90, no. 1, pp. 507–521, 1991.

[49] B. Haider, P. A. Lewin, and K. E. Thomenius, “Pulse elongation and deconvolution filtering for medical ultrasonic imaging,” *IEEE Trans. Ultrason., Ferroelect., Freq. Contr.*, vol. 45, no. 1, pp. 98–113, 1998.

[50] R. Y. Chiao and L. J. Thomas, “Synthetic transmit aperture imaging using orthogonal Golay coded excitation,” in *Proc. IEEE Ultrason. Symp.*, 2000, pp. 1677–1680.

[51] Y. Wang, K. Metzger, D. N. Stephens, G. Williams, S. Brownlie, and M. O’Donnell, “Coded excitation with spectrum inversion (CEXSI) for ultrasound array imaging,” *IEEE Trans. Ultrason., Ferroelect., Freq. Contr.*, vol. 50, no. 7, pp. 805–823, 2003.

[52] J. Shen and E. S. Ebbini, “A new coded-excitation ultrasound imaging system—Part I: Basic principles,” *IEEE Trans. Ultrason., Ferroelect., Freq. Contr.*, vol. 43, no. 1, pp. 131–140, 1996.

[53] C.-C. Shen and P.-C. Li, “Pulse-Inversion-Based Fundamental Imaging for Contrast Detection,” *IEEE Trans. Ultrason., Ferroelect., Freq. Contr.*, vol. 50, no. 9, pp. 1124–1133, 2003.

[54] S. Zhou and J. A. Hossack, “Dynamic-transmit focusing using time-dependent focal zone and center frequency,” *IEEE Trans. Ultrason., Ferroelect., Freq. Contr.*, vol. 50, no. 2, pp. 142–152, 2003.

[55] P.-C. Li, “Pulse compression for finite amplitude distortion based harmonic imaging using coded waveforms,” *Ultrason. Imaging*, vol. 21, no. 1, pp. 1–16, 1999.

[56] Y. Takeuchi, “Coded excitation for harmonics imaging,” in *Proc. IEEE Ultrason.*

Symp., 1996, pp. 1433–1436.

[57] J. Borsboom, C. T. Chin, and N. de Jong, "Experimental validation of a nonlinear coded excitation method for contrast imaging," in *Proc. IEEE Ultrason. Symp.*, 2002, pp. 1933–1936.

[58] W. Wilkening, M. Krueger, and H. Ermert, "Phase-coded pulse sequence for non-linear imaging," in *Proc. IEEE Ultrason. Symp.*, 2000, pp. 1559–1562.

[59] T. X. Misaridis and J. A. Jensen, "An effective coded excitation scheme based on a Tukey-windowed FM signal and an optimized digital filter," in *Proc. IEEE Ultrason. Symp.*, 1999, pp. 1589–1593.

[60] P.-C. Li, E. Ebbini, and M. O'Donnell, "A new filter design technique for coded excitation systems," *IEEE Trans. Ultrason., Ferroelect., Freq. Contr.*, vol. 39, no. 6, pp. 693–699, 1992.

[61] T. X. Misaridis, M. H. Pedersen, and J. A. Jensen, "Clinical use and evaluation of coded excitation in B-mode images," in *Proc. IEEE Ultrason. Symp.*, 2000, pp. 1689–1693.

[62] T. Azuma, Y. Miwa, and S. Umemura, "Subaperture decoding to enhance performance of coded excitation," in *Proc. IEEE Ultrason. Symp.*, 2002, pp. 1669–1672.

[63] P. M. Aziz, H. V. Sorensen, and J. van der Spiegel, "An overview of sigma-delta converters," *IEEE Signal Process. Mag.*, vol. 13, no. 1, pp. 61–84, 1996.

[64] S. L. Marple, *Digital Spectral Analysis: With Applications*. Englewood Cliffs, NJ: Prentice-Hall, 1987.

[65] A. V. Oppenheim and R. W. Schafer, *Discrete-Time Signal Processing*. Englewood Cliffs, NJ: Prentice-Hall, 1989.

[66] S. Haykin, *Adaptive Filter Theory*. 4th ed. Upper Saddle River, NJ: Prentice-Hall, 2002.

[67] S. G. Nash and A. Sofer, *Linear and Nonlinear Programming*. New York: McGraw-Hill, 1996.

[68] R. L. Haupt and S. E. Haupt, *Practical Genetic Algorithms*. New York: Wiley, 1998.